Institut für Entwicklungsgenetik

Helmholtz Zentrum München

Evaluation of the effects of core histone H3.2 through *Aey69*, a microphthalmic mouse mutant

Sharmilee Vetrivel

Vollständiger Abdruck der von der Fakultät Wissenschaftszentrum Weihenstephan für Ernährung, Landnutzung und Umwelt der Technischen Universität München zur Erlangung des akademischen Grades eines

Doktors der Naturwissenschaften

genehmigten Dissertation.

Vorsitzender:	**Prof. Dr. Martin Klingenspor**
Prüfer der Dissertation:	1. **Prof. Dr. Wolfgang Wurst**
	2. **Prof. Angelika Schnieke, Ph.D**
	3. **Assoc. Prof. Natascia Tiso, Ph.D**

Die Dissertation wurde am 16.07.2019 bei der Technischen Universität München eingereicht und durch die Fakultät Wissenschaftszentrum Weihenstephan für Ernährung, Landnutzung und Umwelt am 08.01.2020 angenommen.

Institute of Developmental Genetics

Helmholtz Centre Munich

Evaluation of the effects of core histone H3.2 through *Aey69*, a microphthalmic mouse mutant.

Sharmilee Vetrivel

Complete copy of the dissertation approved by the academic faculty of Life and Food Sciences Weihenstephen of the Technical University of Munich in partial fulfilment of the requirements for the degree of

Doctor of Natural Sciences

Chair:	**Prof. Dr. Martin Klingenspor**
Dissertation Examiners:	1. **Prof. Dr. Wolfgang Wurst**
	2. **Prof. Angelika Schnieke, Ph.D**
	3. **Assoc. Prof. Natascia Tiso, Ph.D**

The dissertation was submitted to the Technical University of Munich on 16.07.2019 and accepted by the academic faculty of Life and Food Sciences Weihenstephen on 08.01.2020.

Dedicated to the mouse that started it all.....

Aey69

Tables

Abbreviations

Abbreviations	Full Form
A	Alanine/Adenosine
Abcb6	ATP-Binding Cassette, Sub-Family B, Member 6
Aey	*Abnormal Eyes*
Ago3	Argonaute RISC Catalytic Subunit 3
ANOVA	Analysis Of Variance
AP2α	Activator Protein 2α
AQP0	Aquaporin 0
ARVO	Association For Research In Vision And Ophthalmology
ASD	Anterior Segment Dysgenesis
Atf1	Activating Transcription Factor 1
B2m	Beta-2-Microglobulin
BME	β-Mercaptoethanol
Bmp4	Bone Morphogenetic Protein 4
Bmp7	Bone Morphogenetic Protein 7
Bmpr1A	Bone Morphogenetic Protein Receptor, Type IA
bp	Base pairs
Brd2	Bromodomain Containing 2
Brg1/ Smarca4	SWI/SNF Related, Matrix Associated, Actin Dependent Regulator Of Chromatin, Subfamily A, Member 4
BRN3	Brain-Specific Homeobox 3
C	Cytosine
C-Maf	Avian Musculoaponeurotic Fibrosarcoma (MAF) Protooncogene

C-Terminal	Carboxyl Terminal
Ca^{2+}	Calcium
CAF-1	Chromatin Assembly Factor 1
CALBINDIN	Vitamin D-Dependent Calcium-Binding Protein, Avian-Type
Car1	Carbonic Anhydrase 1
CAS9	CRISPR-Associated Endonuclease Cas9
CBP	CREB-Binding Protein
Cd163l1	CD163 Molecule Like 1
cDNA	Complementary Deoxyribonucleic Acid
CEF3	Translation Elongation Factor EF-3
CENP-A	Centromere Protein A
Cgn	Cingulin
ChIP-QPCR	Chromatin Immunoprecipitation Quantitative Real-Time PCR
ChIP-Seq	Chromatin Immunoprecipitation Sequencing
Clpx	Caseinolytic Mitochondrial Matrix Peptidase Chaperone Subunit
Cntnap5c	Contactin Associated Protein-Like 5C
Creb	Camp-Responsive Element
Crebrf	CREB3 Regulatory Factor
Crem	Camp Responsive Element Modulator
Crim1	Cysteine Rich Transmembrane BMP Regulator 1 (Chordin Like)
CRISPR	Clustered Regularly Interspaced Short Palindromic Repeats
crRNA	CRISPR RNA
Cryaa	Crystallin, Alpha A
Crygd	Crystallin, Gamma D

Cwc27	Spliceosome Associated Cyclophilin 27
CX	Connexin
D	Aspartic Acid
DAPI	4',6-Diamidino-2-Phenylindole, Dihydrochloride
DMEM	Dulbecco's Modified Eagle Medium
Dnmt3i	DNA Methyltransferase I
Dpp10	Dipeptidylpeptidase 10
Dpp9	Dipeptidylpeptidase 9
Dyl	Dysgenetic Lens
Efna5	Ephrin-A5
Efnb2	Ephrin-B2
EGFP	Enhanced Green Fluorescent Protein
ENU	N-Ethyl-N-Nitrosourea
Epha3	Ephrin Type-A Receptor 3
Ephb2	EPH Receptor B2
Erdr1	Erythroid Differentiation Regulator 1
F	Phenylalanine
F13a1	Coagulation Factor XIII, A1 Subunit
FBS	Fetal bovine serum
FGF	Fibroblast Growth Factor
Foxc1	Forkhead Box C1
FOXE3	Forkhead Box E3
FPLC	Fast Performance Liquid Chromatography

G2	Gap 2 Phase
GCL	Ganglion Cell Layer
GFAP	Glial Fibrillary Acidic Protein
GFP	Green Fluorescent Protein
Gja8	Gap Junction Protein, Alpha 8
GNM	Gaussian Network Model
GRAMM	Global Range Molecular Matching
gRNA	Guide Ribonucleic Acid
H_2O_2	Hydrogen Peroxide
H3/Hist3	Histone H3
HAT	Histone Acetyltransferase
Hdac9	Histone Deacetylase 9
Hes5	Hes Family basic Helix Loop Helix Transcription Factor 5
HIRA	Histone Repression A Factor
Hmgb3	High Mobility Group Box 3
HP1	Heterochromatin Protein
Hsf2	Heat Shock Factor 2
I-TASSER	Iterative Threading Assembly Refinement
Ile	Isoleucine
INBL	Inner Neuroblastic Layer
IPTG	Isopropylthio-β-D- Galactoside
ISL1	Insulin Gene Enhancer Protein
K	Lysine
KAT3	Histone Lysine Acetyltransferases

kb	Kilobases
KD	Kilo Dalton
Leu	Leucine
Lhx2	LIM/Homeobox Protein 2
LP	Lens Placode
M	Methionine
Mab21l2	Mab-21-like 2
MAC	Microphthalmia, Anophthalmia, Coloboma
MACS	Model-based Analysis of ChIP-Seq
Me	Methylation
Mip	Major Intrinsic Protein Of Lens Fiber
Mitf	Melanogenesis Associated Transcription Factor
mRNA	Messenger Ribonucleic Acid
MYC	Myelocytomatosis Oncogene
Myo7a	Myosin 7A
N	Asparagine
N2A	Neuro2A
NR	Neural Retina
nt	Nucleotide
OC	OPTIC CUP
ON	Optic Nerve
O/N	Overnight
ONBL	Outer Neuroblastic Layer
OTX2	Orthodenticle Homeobox 2

OV	Optic Vesicle
P	Proline
P300	Adenovirus Early Region 1A-Associated Transcriptional Co-Activator
PAX2	Paired Box Gene 2
PAX6	Paired Box Gene 6
PBS	Phosphate Buffered Saline
Pck2	Phosphoenolpyruvate Carboxykinase 2
PCR	Polymerase Chain Reaction
Pdpk1	3-Phosphoinositide Dependent Protein Kinase 1
PEG	Polyethylene glycol
PFA	Paraformaldehyde
Phospho	Phosphorylation
Pitpnm1	Phosphatidylinositol Transfer Protein Membrane Associated 1
Pitx3	Pituitary Homeobox 3
PKCA	Protein Kinase C-Alpha
Pmp22	Peripheral Myelin Protein 22
Pogz	Pogo Transposable Element With ZNF Domain
Prox1	Prospero Homeobox 1
Psmd12	Proteasome 26S Subunit, Non-ATPase 12
PTM	Post Translational Modifications
Pxdn	Peroxidasin
Pymol	Python-Enhanced Molecular Graphics
Rax	Retinal Homeobox Protein
Rbbp7	Retinoblastoma Binding Protein 7, Chromatin Remodeling Factor

REST	Relative Expression Software Tool
RGC	Retinal Ganglion Cells
RMSD	Root Mean Square Deviation
RNA	Ribonucleic Acid
RPC	Retinal Progenitor Cells
RPE	Retinal Pigmented Epithelium
Rplp0	Ribosomal Protein Lateral Stalk Subunit P0
RT	Room Temperature
S	Serine
Sdccag8	Serologically Defined Colon Cancer Antigen 8
Sdk1	Sidekick Cell Adhesion Molecule 1
SDM	Site Directed Mutagenesis
SDS-PAGE	Sodium Dodecyl Sulfate-Polyacrylamide Gel Electrophoresis
SE	Surface Ectoderm
Selenbp	Selenium-Binding Protein
Ser	Serine
Sey	Small Eye Mutant
Shh	Sonic Hedgehog Signaling Molecule
Shisa6	Shisa Family Member 6
Six3	Sine Oculis Homeobox Homolog 3
Skp2	S-Phase Kinase-Associated Protein 2
Smad1	SMAD Family Member 1
Smad5	SMAD Family Member 5

Smarca5/ Snf2h	SWI/SNF Related, Matrix Associated, Actin Dependent Regulator Of Chromatin, Subfamily A, Member 5
Smarcad1	SWI/SNF-Related, Matrix-Associated Actin-Dependent Regulator Of Chromatin, Subfamily A, Containing DEAD/H Box 1
Smarcc2	SWI/SNF Related, Matrix Associated, Actin Dependent Regulator Of Chromatin Subfamily C Member 2
Smarcd1	SWI/SNF Related, Matrix Associated, Actin Dependent Regulator Of Chromatin, Subfamily D, Member 1
Snord116	Small Nucleolar RNA, C/D Box 116
SNP	Single Nucleotide Polymorphism
SOX2	SRY (Sex Determining Region Y)-Box 2
Sparc	Secreted Protein Acidic And Cysteine Rich
Sytl3	Synaptotagmin Like 3
Tenm3 /Odz3	Teneurin Transmembrane Protein 3
TGFβ1	Transforming Growth Factor Beta 1
TH	Tyrosine Hydroxylase
tracrRNA	Trans-activating crRNA
Tsc1	Tuberous Sclerosis 1
Tube1	Tubulin, Epsilon 1
Vax2	Ventral Anterior Homeobox 2
Yap1	Yes Associated Protein 1

Summary

Background:

During an ENU (N-ethyl-N-nitrosourea) mutagenesis screen, a dominant small-eye mutant, *Aey69* mouse with viable homozygotes was observed. In a genome-wide linkage analysis using SNP markers, the mutation was mapped to chromosome 3. The comprehensive phenotyping screen of the mutant mice in the German Mouse Clinic revealed only a few statistically significant alterations between wild types and homozygous mutants. Microphthalmia was the most severe developmental phenotype in the mutant mouse line. For a better understanding of the changes during early eye development, microarray analysis of transcriptomic changes in the mutant embryos were done. Surprisingly, none of the key transcription factors of eye development (*Pax6*, *Otx2*, *Sox2*) were found to be among the top-altered genes, raising various questions regarding the pathways and molecules affected for the microphthalmic phenotype. Sequencing revealed a 358A->C mutation (Ile120Leu) in the *Hist2h3c1* gene and a 71T->C mutation (Val24Ala) in the *Gja8* gene (coding for connexin50). Neither of these mutations were found to be associated with microphthalmia until then (Vetrivel et al. 2019).

Amongst the mutant proteins, *Hist2h3c1* encoded H3.2 has not been studied extensively in development. But in *Aey69* a missense mutation in the linker region of the protein results in microphthalmia phenotype. The highly homologous nature of the histone H3 proteins makes any kind of specific interaction or novel function of the protein difficult to analyze. Thus to identify any specific effects and function of the protein, a Crispr/Cas9 based approach is to be employed for generating knock-in mouse lines with mutant and wild-type proteins tagged to a green fluorescent protein (GFP).

Results:

Extensive analysis of ocular development documented revealed apoptotic events in the lens and hyperproliferation in the retina from early embryonic stages. Gene expression analysis revealed differential expression of genes related to ocular development targets including BMP and Ephrin family genes. Immunohistochemical and QPCR analyses revealed *Hist2h3c1* encoded H3.2 to be the primary factor behind the micropthalmic changes. Mitotic analysis by H3S10P marker showed mis-localization of the marker in the developing lens and retina. Therefore, *Aey69* represents a H3.2 mutant mouse with mitotic defects leading to arrested lens development and unchecked retinal proliferation. Transgene line containing the histone gene fused to GFP was established and characterized at genomic, transcriptional and protein level. The GFP tag was then used for ChIP-Seq analysis of the DNA sequences bound by

H3.2. The analysis revealed interesting ocular specific targets and also reiterated the identification of Ephrin family genes to be the top altered genes in *Aey69* through QPCR and ChIP-QPCR.

Conclusions:

This study identifies *Hist2h3c1* encoded H3.2 as a key player in ocular development. By incorporation at specific ocular developmental factors Histone H3.2 facilitates the function of these genes for successful lens & retina differentiation.

Zusammenfassung

Hintergrund:

Während eines ENU (N-Ethyl-N-Nitroseharnstoff) - Mutagenese-Screenings wurde eine dominante Mausmutante mit kleinen Augen, homozygot lebensfähig, beobachtet. In einer genomweiten Kopplungsanalyze mittels SNP-Markern wurde die Mutation auf Chromosom 3 abgebildet. Das umfassende Phänotypisierungsscreening der mutierten Mäuse in der Deutschen Mausklinik ergab nur wenige statistisch signifikante Veränderungen zwischen Wild-typen und homozygoten Mutanten. Die Mikrophthalmie war der schwerste Entwicklungsphänotyp in der mutierten Mauslinie. Zum besseren Verständnis der Veränderungen während der frühen Augenentwicklung wurde eine Mikroarray-Analyze der transkriptomischen Veränderungen in den mutierten Embryonen durchgeführt. Überraschenderweise wurde festgestellt, dass keiner der Schlüsseltranskriptionsfaktoren der Augenentwicklung (*Pax6*, *Otx2*, *Sox2*) zu den am häufigsten veränderten Genen gehört, was verschiedene Fragen zu den Signalwegen und Molekülen aufwirft, die in dem mikrophthalmischen Phänotyp betroffen sind. Die Sequenzierung ergab eine 358A-> C-Mutation (Ile120Leu) im *Hist2h3c1*-Gen und eine 71T-> C-Mutation (Val24Ala) im *Gja8*-Gen (kodiert für Connexin50). Keine dieser Mutationen wurde bis jetzt mit einer Mikrophthalmie assoziiert (Vetrivel et al. 2019).

Unter den mutierten Proteinen wurde Hist2h3c1, das für H3.2 kodiert, in der Entwicklung nicht ausführlich untersucht. Aber in Aey69 führt eine Missense-Mutation in der Linker-Region des Proteins zu einem Mikrophthalmie-Phänotyp. Die hochgradig homologe Natur der Histon-H3-Proteine erschwert die Analyze jeglicher spezifischer Wechselwirkungen oder neuer Funktionen des Proteins. Um spezifischen Effekte und Funktionen des Proteins zu identifizieren, werde ein Crispr / Cas9-basierter Ansatz zur Erzeugung von Knock-In-Mauslinien mit mutierten und Wildtyp-Proteinen verwendet werden, die mit grün-fluoreszierendem Protein (GFP) markiert sind.

Ergebnisse:

Umfangreiche Analyzen der Augenentwicklung zeigten apoptotische Ereignisse in der Linse und Hyperproliferation in der Retina in frühen embryonalen Stadien. Die Genexpressionsanalyze ergab eine unterschiedliche Expression von Genen, die in Zusammenhang mit der Augenentwicklung stehen, einschließlich Genen der BMP- und der Ephrinfamilie. Immunhistochemische und QPCR-Analyzen ergaben, dass *Hist2h3c1*-kodiertes H3.2 der Hauptfaktor für die mikropthalmologischen Veränderungen ist. Eine

mitotische Analyze mittels dem H3S10P-Marker zeigte eine Fehllokalisierung des Markers in der Linsenentwicklung und in der Retina. Daher stellt Aey69 eine H3.2-Mausmutante mit mitotischen Defekten dar, die zu einer verzögerten Linsenentwicklung und einer unkontrollierten Netzhautproliferation führen. Eine Transgenlinie, die das an GFP fusionierte Histon-Gen enthält, wurde etabliert und auf genomischer, transkriptionaler und Proteinebene charakterisiert. Die GFP-Markierung wurde zur ChIP-Seq-Analyze der durch H3.2 gebundenen DNA-Sequenzen verwendet. Die Analyze ergab interessante okularspezifische Zielmoleküle und bestätigte durch QPCR und ChIP-QPCR, dass die Gene der Ephrinfamilie die am häufigsten veränderten Gene in Aey69 sind.

Schlussfolgerungen:

Diese Studie identifiziert Hist2h3c1-kodiertes H3.2 als einen Schlüsselakteur in der Augenentwicklung. Durch den Einbau an spezifischen Augenentwicklungsfaktoren ermöglicht Histon H3.2 die Funktion dieser Gene für eine erfolgreiche Differenzierung zwischen Linse und Retina.

Acknowledgements

My Doctoral Dissertation at the Institute of Developmental Genetics (IDG), Helmholtz Zentrum Munich has helped in enhancing my scientific knowledge and has also made it a very thankful journey. I wish to express my humble gratitude to Prof. Dr. Wolfgang Wurst (Dir. IDG) and Dr. Daniela V Weisenhorn (Deputy Dir., IDG) for providing me support and facilities to perform this research work.

The foremost appreciation I would like to offer to my Project supervisor and Guide, Prof. Jochen Graw. He has helped me in crafting various aspects of my thesis. I also feel obliged to my co-supervisors Prof. Angelika Schnieke, Prof. Wolfgang Wurst and Dr. Natascia Tiso for their timely advice and kind encouragement.

Special thanks needs to be said to my mentor Dr. Florian Giesert for providing valuable scientific discussions and guiding me through transgenic experiments. In addition, I would like to thank Dr. Michael Rosemann for his constructive criticism during various meetings. I also wish to express my humble gratitude to Dr. Arie Geerlof and Dr. Robert Janowski, who helped me in executing the collaborative projects.

My research experience would not be complete without the friendly help of my colleagues, Claudia Dalke and Oanna Amarie. My thesis and exposure was made memorable and worth reminiscing due to the presence of my friends from the beginning to the end of my journey - Sarah kunze, Daniel Pawliczek, Marie Claire Ung, Maria Castiblanco, Natalia Dealgado, Tanja Orschmann and Theresa Bäcker.

I am forever grateful to the various experts and scientists at the Helmholtz Zentrum Munich who extended their gracious response and help for my various emails. I extend my appreciation to the DAAD for providing me financial support during my Ph.D.

The acknowledgments mentioned above could be meaningless without the mention of the persons who taught me the meaning of ‘Thanks’. I would like to thank and dedicate my thesis to my family.

1 Introduction

1.1 Ocular system

The eye is one of the most complex organs of the human body and provides 80% of external input processed by the brain (Iwata and Tomarev 2008; Jerath et al. 2015). The eye represents an interesting organ system for research due to its accessibility from *in utero* stage and the availability of various non-invasive high-throughput ocular screening methods for morphological (ophthalmoscopy) and functional (electroretinography) examination (Freund et al. 1996; Iwata and Tomarev 2008; Willoughby et al. 2010). The eye consists of three major layers: the outer region consisting of the cornea and the sclera, middle layer composed of the iris, the ciliary body and the choroid and finally the retina comprises the inner layer of the eye. The three regions are surrounded by transparent structures namely, the aqueous, the vitreous and the lens (Willoughby et al. 2010). The tissues comprising the ocular system have diverse functions. The optical function is provided by the lens, cornea and iris. The cornea refracts and transmits the light to the lens. The iris controls the amount of light reaching the retina from the lens. The light sensing and transmission function is provided by the retina through its complex array of neurons and photoreceptors. The structural component is provided by sclera and choroid. Sclera forms a connective tissue coat that protects the eye from internal and external forces and maintains its shape. Choroid is the vascular layer that provides oxygen and nutrients to the outer retinal layers (Freund et al. 1996; Willoughby et al. 2010).

Experimental models for understanding the genetics, development, and physiology of the human eye have been developed in different mammalian and non-mammalian species. Particularly, classical and targeted genetic approaches in the laboratory mouse, *Mus musculus*, have yielded a large number of mouse models that replicate key features of human eye diseases (Krebs et al. 2017; Sundin 2009). Still, major anatomical differences exist between the mouse eye and the human eye. Of note, the mouse lens is more spherical in shape compared to the human lens and occupies most of the vitreal cavity. The mouse retina has different photoreceptor adaptations not found in humans, as an adaptation for its nocturnal and crepuscular lifestyle (Sundin 2009).

1.2 Embryonic development of the ocular system

The ocular system presents an interesting challenge in understanding its development. The vertebrate eye comprises tissues from different embryonic origins: the lens and the cornea

are derived from the surface ectoderm and periocular mesenchyme, but the retina and the epithelial layers of the iris and ciliary body are from the anterior neural plate (Graw 2010).

Organogenesis of the eye is a multistep process comprising (Fuhrmann 2010):

- Formation of optic vesicles:

Earliest morphological sign of the ocular system is the appearance of symmetrical bilateral evaginations from the diencephalon, which slowly expand through the mesenchyme towards the surface ectoderm during the final stages of neural tube formation (Adler and Canto-Soler 2007). The evagination results in the formation of bilateral optic vesicles (Fuhrmann 2010).

- Invagination of the distal domain of the vesicles

Optic vesicle (OV) becomes further established by the appearance of symmetrical bilateral evaginations from the diencephalon. The evaginations slowly expand through the mesenchyme towards the surface ectoderm establishing the contact between the distal portion of the OV and the overlying surface ectoderm (Heavner and Pevny 2012).

- Morphogenesis of the optic cup.

The interaction between optic vesicle and surface ectoderm results in the formation of the bilayered optic cup and lens placode. The lens placode further invaginates into a vesicle that eventually closes and separates completely from the surface ectoderm (Graw 2010). The connection between the optic cup (OC) and the diencephalon is established by the optic stalk (Heavner and Pevny 2012).

- Differentiation into ocular tissues.

During morphogenesis of the optic cup, the ocular tissues become specified. The inner and outer layer of the optic cup becomes differentiated into neural retina and the retinal pigment epithelium, respectively. The margin between the two layers at the anterior side of the optic cup gives rise to iris and ciliary body. The optic stalk, narrows to become the optic fissure which eventually closes to form the optic nerve through which the visual processing of the retina is communicated to the brain (Adler and Canto-Soler 2007).

The timely action of transcription factors and inductive signals ensure the correct development of the different eye components. During embryonic development, reciprocal inducing events result in the formation of the functional ocular system which requires precise spatial organization and interaction between individual tissues to respect the laws of optics. In

multicellular organisms, precisely regulated genetic and epigenetic mechanisms help in achieving specification of individual cell lineages.

Multiple eye disorders, including anophthalmia or microphthalmia, aniridia, coloboma, and retinal dysplasia have been shown to result from disruptions in embryonic eye development (Fuhrmann 2010). Disrupted lens and retinal development can cause isolated or widespread ocular abnormalities that can obstruct vision at different levels and lead to blindness (Pirity et al. 2007). Thus, it is critical to understand the mechanisms that lead to altered eye development under a pathological condition.

Fig.1.1

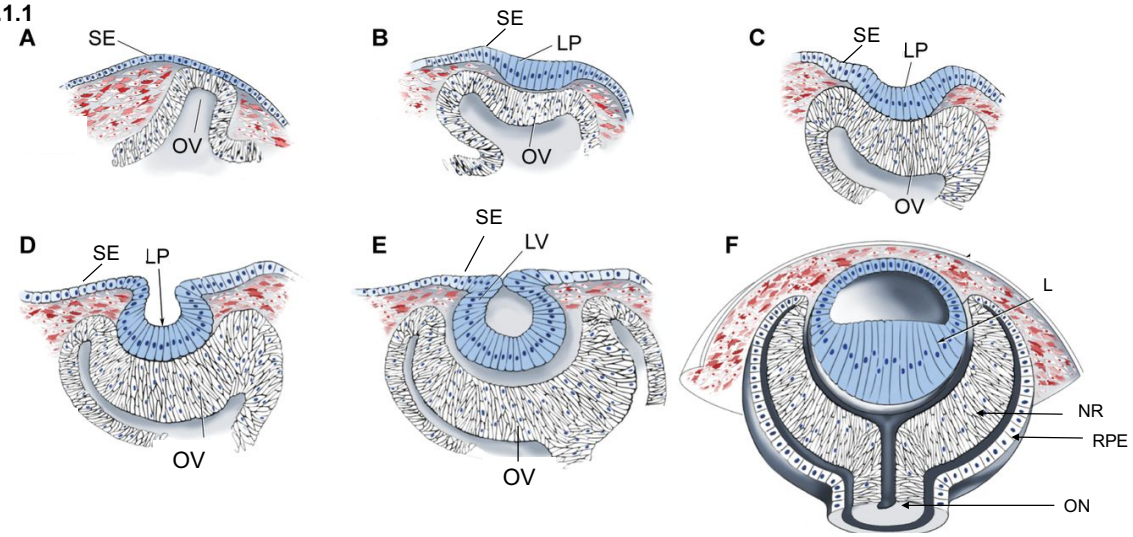

Fig. 1.1: Organogenesis of the eye.
Schematics showing the key processes of eye development during embryogenesis. (A) Earliest morphological sign of the ocular system with the optic vesicle (OV) and surface ectoderm (SE) (B) Invagination of the distal domain of the optic vesicle and formation of the lens placode (LP). (C) Interaction between optic vesicle and lens placode (D&E) Invagination of the lens placode to form the lens vesicle (LV) that eventually closes and separates completely from the underlying optic vesicle (F) Differentiation and morphogenetic processes in the optic vesicle give rise to the neural retina (NR) and retinal pigemented epithelium (RPE) and optic nerve (ON). The lens vesicle separates from the surface ectoderm to give rise to the lens. Adapted from Cvekl and Ashery-Padan 2014 under the terms of the Creative Commons Attribution License.

1.3 Microphthalmia

Microphthalmia (small eye), Anophthalmia (absent eye) and coloboma (optic fissure closure defects), collectively referred to as MAC, form a spectrum of developmental eye disorders, with an estimated incidence of 3.0 per 10,000 live births (Chambers et al. 2018). MAC can

occur alone or in combination with other ocular anomalies, such as early onset cataract and anterior segment dysgenesis (ASD). They are associated with extraocular features in just over half of the cases (Shah et al. 2011) and can be part of a syndrome (Slavotinek 2011). The clinical diagnosis is based upon an ophthalmologic examination, family history and molecular genetic testing and ocular/brain imaging (Bardakjian et al. 1993). The risk factors for MAC include maternal age over 40, multiple births, infants of low birth weight and low gestational age (Verma and Fitzpatrick 2007).

The diverse morphological alterations associated with MAC pathogenesis in clinical samples include (Bardakjian et al. 1993; Verma and Fitzpatrick 2007):

- Degeneration of optic vesicles
- Decreased optic cup size
- Altered proteoglycans in the vitreous
- Abnormal growth factor production
- Failure of the optic fissure closure

Molecular genetic testing has been able to identify a genetic cause in more than 50% of individuals (Graw 2019; Plaisancie et al. 2016). Thus, the analysis of novel genes in microphthalmic mouse models could help in the identification of the remaining unknown factors.

1.4 Mouse models of microphthalmia

Amongst the causative genes for microphthalmia, transcription factors represent the largest group followed by TGFβ/BMP signaling molecules, retinoic acid pathway genes and other miscellaneous genes with known or unknown functions (*Abcb6, Crim1, Hmgb3, Mab21l2, Odz3, Pxdn, Shh and Yap1)* (Reis and Semina 2015). In addition, amongst the microphthalmia associated-transcription factors mouse models for *Pax6, Sox2, Mitf, Rax* and *Pitx3* have been extensively characterized for their role in microphthalmia.

1.4.1 *Pax6*

PAX6 is a highly conserved 422 amino acid transcription factor consisting of two DNA-binding domains and a C-terminal region that functions in transcriptional activation (Osumi et al. 2008). PAX6 has been found to have diverse embryonic roles including patterning of the neural tube, formation of neural circuits, cortical cell proliferation and differentiation and development of

motor neurons (Hever et al.2006). The earliest microphthalmic *Pax6* mouse mutant was detected by Roberts 1967. Since then several *Pax6* allelic series of diverse ocular phenotypes have been identified for their molecular effect on ocular development (Graw 2019). Importantly the genetic studies in mice have helped in estimating the *Pax6*/PAX6 for the neural retinal cellular changes in microphthalmia (Manuel et al. 2008). The role of *Pax6* as a primary regulatory player for ocular embryonic proliferation was also identified through the models (Hever et al. 2006). Concurrently lens specific over expression pattern of specific *Pax6* isoform which lacks the paired domain of the DNA binding domain was found to cause apoptotic cell death in the lens during embryonic development (Osumi et al. 2008).

1.4.2 *Sox2*:

SOX2 represents a High Mobility Group domain containing transcription factor (Schneider et al. 2009). It is a single-exon gene coding for a 317 amino acid protein with a conserved DNA-binding high mobility group domain and a C-terminal transactivation domain. *Sox2* mutations have been found to account for almost 10–20% of severe cases of bilateral microphthalmia/anophthalmia (Schneider et al. 2009; Verma and Fitzpatrick 2007). Similar to *Pax6* allelic series, *Sox2* allelic series in mouse revealed Sox2 dosage dependent ocular phenotypic effect (Taranova et al. 2006). A key role for *Sox2* in the regulation of the NOTCH1 signaling pathway in retinal progenitor cells was also observed. Further, several targeted mouse mutants (*Sox2LP*, *Sox2IR*, *Sox2EGFP*$^{/IR}$ and *Sox2EGFP*$^{/LP}$) with a range of eye phenotypes from mild microphthalmia to severe anophthalmia have been developed and characterized (Graw 2019). Particularly, optic cup specific deletion of *Sox2* results in altered conversion of the neural retina through modulating the WNT/β-Catenin pathway (Heavner et al. 2014). In addition, targeted ablation of *Sox2* in the optic cup of *Pax6* haploinsufficient mice revealed that precise ratio of SOX2 to PAX6 is necessary for neural retina developmental competence in the retina (Matsushima et al. 2011).

1.4.3 *Mitf*:

MITF protein is a member of the MYC supergene family of basic-helix-loop-helix-leucine-zipper domain containing DNA-binding transcription factor (Arnheiter 2010). Mice harboring mutation in thr *Mitf* locus coding for the microphthalmia-associated transcription factor were one of the earliest microphthalmic mouse mutants described (Hertwig 1942). The homozygous mutants had unpigmented eyes of variably small size and might be the reason that the discovered gene was named as “Microphthalmus” according to the eye phenotype (Arnheiter 2010). *Mitf* allelic series exhibit the broad phenotypic variability found from near normal to white microphthalmic animals with osteopetrosis (Steingrímsson et al. 2003). *Mitf* has now

been established to be a highly interesting locus for its pleiotropic effects on unrelated tissues such as the retinal pigment epithelium, melanocytes, and long bones (Arnheiter 2010). Inter- and intra-allelic interactions in the locus has also been identified by *in-vivo* experiments (Konyukhov and Osipov 1968; Steingrímsson et al. 2003). Subsequently, extensive molecular work has established the role of MITF as a master regulator for melanocyte development (Hou and Pavan 2008). In addition, comparative analyses of eye development in *Mitf* and *Pax6* mouse mutants documented the role of *Pax6* gene dose regulates RPE transdifferentiation in *Mitf* mutants (Bharti et al. 2012).

1.4.4 *Rax*:

Rax is a paired-type homeobox gene encoding homeodomain protein with an octapeptide motif in the N-terminus and a transactivation OAR (otp, aristaless, and rax) domain in the C-terminus (Muranishi et al. 2012). The transcription factor RAX is localized in diverse tissues including anterior neural plate, ventral forebrain, optic cup, hypothalamus and posterior pituitary during embryonic development (Mathers et al. 1997). Mice with a hypomorphic *Rax* allele develop anophthalmia and hypothalamic abnormalities (Muranishi et al. 2012). Though *Rax* is not expressed in the lens, *Rax*-null embryos do not develop any lens structure. Rax was found to regulate lens formation through β-catenin signaling (Swindell et al. 2008). Homozygous *Rax* null mutant mice fail to form optic vesicles, ventral forebrain structure and die from perinatal lethality. This is in contrast to the homozygous *Pax6*-null mutants wherein optic vesicles are developed, but the vesicles do not grow and gradually degenerate. It was found that the *Pax6*-dependent formation of retinal progenitor cells is dependent on a functional copy of the *Rax* gene. Thus, *Rax* has been postulated to have an earlier role than *Pax6* in eye development (Muranishi et al. 2012; Zhang et al. 2000).

1.4.5 *Pitx3*:

PITX3 is a 302 amino acid bicoid-related homeodomain transcription factor. PITX3 is critical for the development of the ocular lens, mesencephalic dopaminergic neurons and skeletal muscle (Li et al. 2009). In humans, mutations in PITX3 are responsible for cataracts and Parkinson's disease (Ahmad N et al. 2013). *Pitx3* is expressed in mouse embryos in the developing lens, midbrain, and craniofacial and skeletal muscle (Semina et al. 1998). The *aphakia* (*ak*), *eyeless* (*eyl*) and *miak* are *Pitx3* mouse mutants characterized extensively for their microphthalmic pathology. The *aphakia* mouse is a recessive mutant with a double deletion in the upstream region of *Pitx3* leading to *Pitx3* protein deficiency (Ahmad N et al. 2013). The eyeless mutant is characterized by a guanine insertion (c.415_416insG) in *Pitx3*,

leading to a truncated protein (Rosemann et al. 2010). In *miak* mice, c.444C>A nonsense mutation in the *Pitx3* locus leads to a mutant PITX3 protein which lacks the C-terminus (Wada et al. 2014). Analysis of lens development in these mouse models has established a pivotal role for Pitx3 in lens fibre differentiation.

1.5 ENU mouse mutants in ocular research

With the advent of transgenic technology, specific gene based deletion mutants, conditional knockouts, reporter mouse lines are becoming an ideal source to study in depth the ocular specific molecular functions (Ohuchi et al. 2019; Yasue et al. 2017; Yu and Wu 2018). However, for the identification of novel genes of ocular importance, reverse genetics approaches including radiation or *N*-ethyl-*N*-nitrosourea (ENU) is an ideal choice (Takahashi et al. 1994). Reverse genetics approach represents a phenotype-driven approach and has the advantage of not being biased by pre-conceived concepts about gene function (Thaung et al. 2002). In addition, while transgene approaches result in a complete loss of the corresponding gene, reduced gene function induced by point mutations are more informative regarding the specific role of a gene in developmental pathology. For inducing point mutations, mutagen ENU has been found to be extremely efficient in the male mouse germ-line to induce mutations at a rate of 1.3×10^{-3} per locus (Stottmann and Beier 2014; Thaung et al. 2002).

Concurrently, in an ocular phenotype based mouse mutant screening ENU was found to induce a predominance of microphthalmia, anophthalmia and cataracts pathologies in C57BL/6 inbred mice (Baird et al. 2002). In addition, the mutants developed by ENU have been found to genetically mirror human ocular diseases (Dalke and Graw 2005; Thaung et al. 2002). Particularly, ENU induced *Pax6* missense mutations have been surveyed to identical counterparts in human patients (Thaung et al. 2002; Love et al. 1998; Xu et al. 1999). Also, an archive of ENU induced mouse mutations (https://www.helmholtz-muenchen.de/ieg/services/scientific-resources/index.html), is available for researching on possible candidate genes upon observance of the specific gene with a selected clinical phenotype. The archive also represents a source for diverse mouse mutants discovered and phenotypically characterized as microphthalmic mouse mutants, but not yet characterized at the molecular level (Graw 2019).

1.6 *Aey69* mouse

Aey69 mouse is one of the mouse lines developed at Helmholtz Zentrum, Munich by ENU approach (Vetrivel et al. 2019). *Aey69* mouse (abnormal eyes) was identified by morphological observation of its small eyes. The mutant mouse line is maintained on a C3HeB/FeJ genetic

background. Linkage was demonstrated to mouse chromosome 3 between the markers *D3Mit188* and *D3Mit11*. Exome sequencing analysis has revealed changes in *Gja8* and *Hist2h3c1*. Because of the unexpected finding of a mutation in a histone gene causing microphthalmia without a lens, attempts were to separate the two candidate genes *Gja8* and *Hist2H3c1* genetically. Unfortunately, they were so close together (*Gja8* at 96.9 Mb and *Hist2H3c1* at 96.2 Mb; ENSEMBL release 94) that no separation could be obtained after 5 generations outcrossing (Graw, unpublished data).

1.6.1 Novel characteristics of *Aey69*

Small-eye mutants are quite a frequent phenotype, and some of them are caused by mutations in the *Pax6* gene (Graw et al. 2005). In contrast to most of the *Pax6* mutants, the small-eye mutant *Aey69* described here is homozygous viable, which makes this mutant line very interesting. The pathology of microphthalmia onsets from the embryonic stage of E11.5 similar to the *aphakia* mutant mice. Histological analyses of eye development in the homozygous *Aey69* and wild-type (C3H) mouse are demonstrated in Fig. 1.2. The histological analyses clearly indicate a failed surface ectoderm separation at E11.5 leading to a diminishing lens area and dysregulated lens development in the mutant. The changes in the retina become more prevalent at around P1 wherein, the retinal pigmented epithelium (RPE) does not stop at the tips of the retina like in the wild types but covers the entire anterior part of the eye. Finally, after birth, RPE and other layers of the retina invade massively the central part of the eye, filling up the empty ‘lens space’.

The disruptions in lens development had been characterized previously through the work of Andrea Richter-Kügler (Master’s thesis 2013) by CRYGD stainings. The lens-specific expression of CRYGD indicate clearly that there is lens material expressing these proteins. However, there has been no specific immunohistochemical studies on the nature of alterations in retina in the embryonic stages or in the postnatal stages. In addition, homozygous *Aey69* mutants are viable and fully fertile. Comprehensive and standardized phenotyping of this mutant line revealed only a few altered phenotypes between the wild types and the homozygous mutants: increased locomotor activity (hyperactivity) and increased rearing, which is combined with decreased anxiety. An increased body temperature, less body mass and reduced blood lipid values are further characteristics of this particular mutant line. Thus *Aey69* represents a unique mutant mice line with the predominant ocular developmental defects and comparatively less severe systemic effects (Vetrivel et al. 2019).

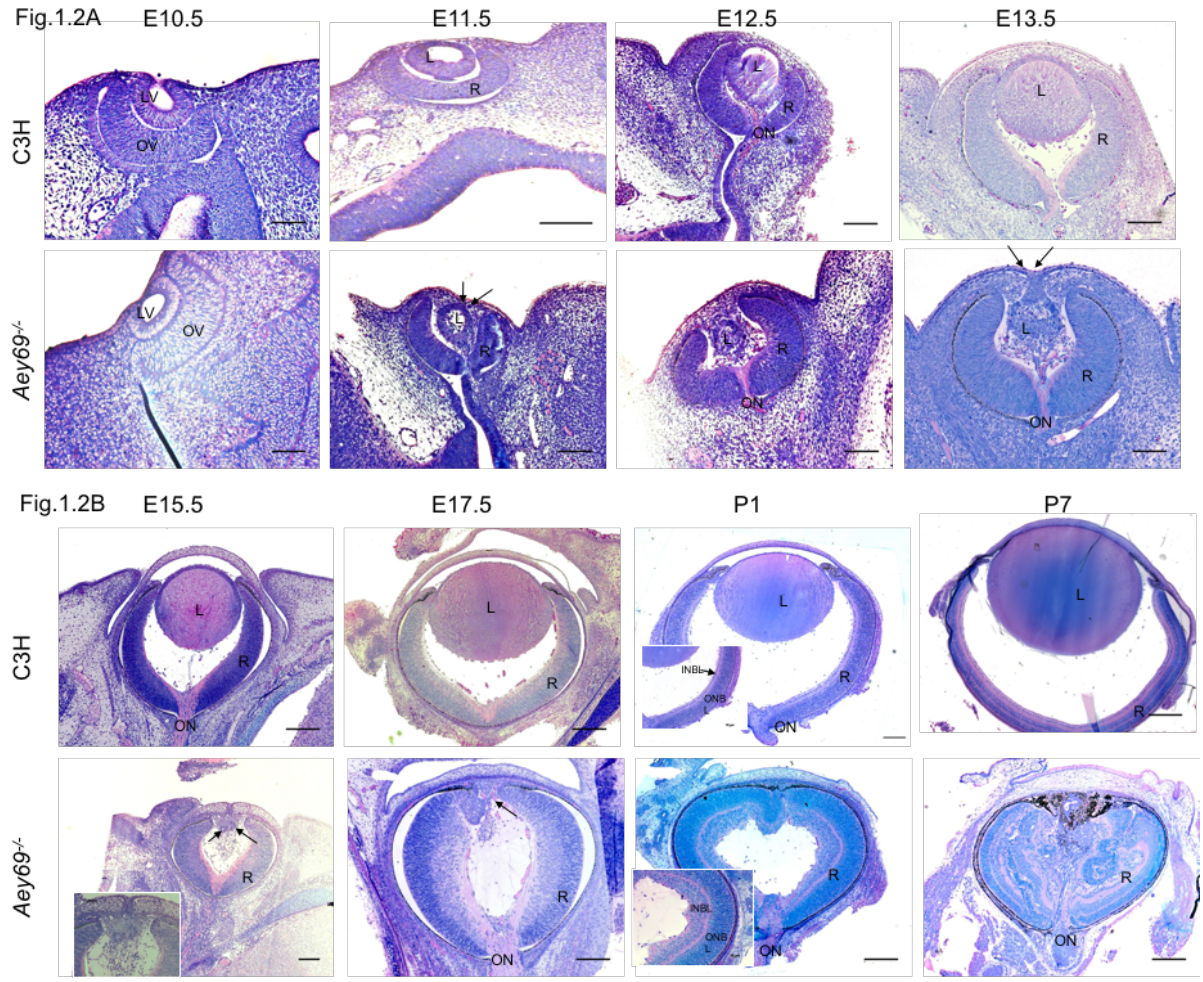

Fig. 1.2: Histological analysis of the Aey69 ocular phenotype.
The comparative histological staining between the wild-type and homozygous Aey69 eyes are shown. Eye development is demonstrated from embryonic day E10.5 until postnatal day P) 7. The figure summarizes the major disruptions in development starting from the lens vesicle stage of E11.5 (a) and the overgrowing of the retina into the empty lens space after birth (b). In particular, at E11.5 in the wild type there is no surface ectoderm connection between the future cornea and lens. However, in the mutant the surface ectoderm connection is maintained (as highlighted by black arrows) through the embryonic stages of E11.5-E13.5, when the lens gradually disappears. Further changes in later embryonic stages are also highlighted by their respective black arrows - at E15.5 increased infiltration of periocular mesenchymal cells into the mutant vitreal space, at E17.5 altered bending of retinal layers anterior to the cornea, and at P1 the mutant retinal layers are observed to be much thicker compared to the wild type. The bars indicate 100 µm at E10.5-E12.5, 50 µm at E13.5 - E15.5, and 0.1 mm at P7. L, lens; R, retina; ON, optic nerve; INBL, inner neuroblastic layer; ONBL, outer neuroblastic layer. Adapted from Vetrivel et al. 2019 under the terms of the Creative Commons Attribution License.

1.6.2 Transcriptomic analysis in *Aey69*

For a better understanding of the changes during early eye development, microarray analysis was done before the doctoral project commencement in collaboration with Prof. Dr. Johannes

Beckers (Gene Regulation and Epigenetics Group, Institute of Experimental Genetics, HMGU). Transcriptomic analyses was done in *Aey69* mutant embryos and their wild-type littermates using whole embryos (E9.5), embryo heads (E10.5, E11.5), tissues of the eye region (E12.5), and whole eyes (E13.5). The approach resulted in 376 regulated genes at E9.5, 157 genes at E10.5, 420 genes at E11.5, 847 genes at E12.5, and 739 genes at E13.5. The results clearly indicated that lens-specific genes like crystallin genes and *Mip,* are downregulated in the mutant eye at E12.5 and E13.5, indicating that at these stages the lens vesicle does not develop properly to a lens. In addition, no major ocular development factors namely *Pax6*, *Sox2*, *Pitx3*, *Six3* were amongst the top altered genes. This observation was also validated separately by immunohistochemistry (Richter-Kügler 2013 Master's thesis). Thus in-depth analysis of the altered genes from microarray by QPCR would be the next crucial step.

1.7 Digenic nature of the mutation in *Aey69*

Aey69 represents a unique mouse model with two point mutations in two diverse genes: a gap junction mediating intercellular communication (*Gja8*) and a histone gene providing structural and regulatory components for epigenetic regulation (*Hist2h3c1*).

1.7.1 Gap Junction proteins

Gap junction proteins / Connexins play an important role in the regulation of the intercellular communication and maintenance of cellular homeostasis (Kar et al. 2012). Connexins typically have a molecular weight ranging between 25 and 62 kDa and the respective size is currently used to designate the different protein isoforms (Evans et al. 2006). Gap junction proteins have four transmembrane domains connected by two extracellular loops and N- and C-terminal tails projecting into the cytoplasm (Yeager and Harris 2007). The proteins undergo oligomerization at appositional membranes and form gap junction channels. Gap junction channels are low resistance channels regulating intercellular transport of biological molecules with masses up to 1 kDa (Yu et al. 2016). Gap junction mediated transport regulate signaling and function of various organ systems including central nervous system (CNS), heart, lens, liver, lung, retina, ear, kidney, testis, ovary, breast, bone, skin, etc. (Kar et al. 2012). Tissue specific transport functions are mediated by the region and stage specific expression pattern of the different gap junction isoforms with unique gating and permeation properties (Mathias et al. 2010; Pfenniger et al. 2011). For example, CX32 is the predominant gap junction in liver. Pathological alterations in CX32 was found to be positively correlated

with cholelithiasis, hepatitis, hepatocellular carcinoma and liver cirrhosis in humans and mammalian knockout models (Maes et al. 2015).

In the ocular system, CX43, CX46 and CX50 play crucial and unique roles in the lens development and differentiation (Yu et al. 2016). During lens growth and development the differentiating fibres in the lens nucleus lose all their intracellular organelles, while accumulating high concentrations of soluble crystallin proteins that increase their refractive index to become the mature fibres in the deep cortical region of the lens nucleus (White and Bruzzone 2000; Wride 2011). Gap junctions contribute to lens function by helping maintain an environment that favors crystallin solubility and fibre transparency by coupling the metabolically active epithelium and the organelle lacking lens fibres (White and Bruzzone 2000). The change in the expression pattern of connexins during lens differentiation suggests that connexins may have different roles in lens development and physiology (Berthoud and Ngezahayo 2017).

1.7.2 *Gja8*

CX50 is a 440 aa protein, coded by the *Gja8* gene and is found to be expressed in the ocular system, the anterior pituitary and the testis (Dorgau et al. 2015; Kar et al. 2012; Vitale et al. 2017). CX50 was found to respond to cellular stimuli during anterior pituitary development and spermatogenesis (Pelletier et al. 2015; Vitale et al. 2017). However, *Gja8* null mice exhibit normal fertility (Kidder and Cyr 2016). Also, no pathological alteration in CX50 was found in the anterior pituitary of db/db mice, even though obesity has been reported to modify connexion protein levels in a wide range of tissues in the body (Pelletier et al. 2015). Interestingly, for the ocular system, the importance of *Gja8* is corroborated by the ocular abnormalities and cataractogenesis induced by mutations in the gene (Berthoud and Ngezahayo 2017; Yu et al. 2016).

Amongst the three connexin isoforms expressed in the lens (CX43, CX46 and CX50) CX50 is highly expressed in both epithelial cells and fibres (Mathias et al. 2010). GJA8 has been established to be critical for epithelial cell proliferation and differentiation during postnatal development (Berthoud and Ngezahayo 2017; White and Bruzzone 2000). The stimulatory effect of CX50 on lens cell differentiation has been identified to be mediated by modulating expression of cyclin-dependent kinase inhibitor p27/p57 and E3 ubiquitin ligase complex component Skp2 (S-phase kinase-associated protein 2) (Shi et al. 2015). Also there is an existence of a positive feedback circuit between FGF signaling and CX50 function to regulate lens size (Berthoud et al. 2014). CX50 also cooperates with AQP0 to mediate cell-cell adhesion function (Liu et al. 2011). Ca^{2+} dependent binding cleavage of the C-terminal of

CX50 has been proposed to occur during the maturation of lens fibre cells (Nielsen et al. 2012). In the retina, CX50-positive horizontal cells have been postulated to regulate light adaptation in the retina (Dorgau et al. 2015). In humans, the importance of CX50 for lens function is demonstrated by several dominant cataracts caused by mutations in the *GJA8* gene (Churchill and Graw 2011).

The functional role of CX50 in determining lens size is supported by mice expressing different *Gja8* mutants which have decreased lens sizes (Berthoud and Ngezahayo 2017). In particular, lenses from homozygous *Gja8* (D47A) mutants show pathological nuclei retention suggesting that CX50 may mediate intercellular diffusion of second messengers required for lens differentiation (Berthoud et al. 2013a). In case of humans, *GJA8* point mutants lead to increased hemichannel activity in exogenous expressions systems and differ in their ability to form functional gap junction channels (Berthoud and Ngezahayo 2017). Till now, more than 20 *GJA8*/*Gja8* point mutations of varying inheritance pattern has been identified in humans and mouse (Berthoud and Ngezahayo 2017). The molecular analyses from these diverse mouse models postulate the role of CX50 in lens pathology through (Berthoud et al. 2014; Berthoud and Ngezahayo 2017; Yu et al. 2016) :

- Inefficiency in forming gap junction channels
- Impaired trafficking,
- Alterations in voltage-dependent gating
- Difference permeability properties

Consequently, the effect of overexpression of *Gja8* in lens epithelial cells has not been tested. Also the signaling pathways, by which altered gap junction activity leads to lens defects, have not been identified (Berthoud and Ngezahayo 2017). These lacunae in literature represents the need for more extensive molecular characterization of *Gja8* and its mutants. Interestingly, *Gja8* mutation in *Aey69* (71T->C; Val24Ala) has not yet been identified/described till now in mammalian models (Vetrivel et al. 2019). Changes in *Gja8* have been mostly associated with cataract and smaller lenses (Kumar et al. 2013), but loss of lens in *Aey69* suggests the possibility for uncharacterized early ocular developmental roles (E11.5-E13.5) of CX50.

1.7.3 Histones:

Histones are evolutionary conserved, small basic proteins composed of 5 main subtypes: H1, H2A, H2B, H3 and H4 (Becker and Workman 2013). Histones represent the main structural components for the compaction of DNA to form chromatin complex (Marino-Ramírez et al. 2005). The first structural organization of chromatin is the nucleosome core. Nucleosome core

is composed of a cylindrical core octamer constituted by heterotetramer of H3 and H4 sandwiched between a pair of H2A-H2B heterodimers (Becker and Workman 2013). Each histone octamer has 147 base pairs of supercoiled DNA wrapped around its outer surface and stabilized by electrostatic interactions (Cvekl and Mitton 2010). Nucleosome cores are separated by linker DNA of variable length, associated with the linker histone H1 (Mariño-Ramírez et al. 2005). The overall structural state of chromatin controls DNA replication and the transcription of underlying genes (Becker and Workman 2013). Taking into consideration the structural role of histones in maintaining the chromatin. The concept of the histone code was introduced in 2000 by Strahl and Allis. The histone code acts through

- formation of histone modifications through histone acetyltranferases (HATs), protein methyltransferases, and serine/threonine protein kinases
- reading the modifications by reader proteins having chromo/bromodomains.

One example for the histone code is the recognition of the dimethylation of lysine 9 in histone H3 by heterochromatin protein 1 (HP1) via its chromodomain resulting in chromatin condensation. Histone code exists in a number of possible combinations such as silently repressed islands, active sites of transcription for housekeeping genes and specific temporal points for gene regulation (Bannister and Kouzarides 2011; Oliver and Denu 2011). The dynamic regulatory nature of the histone code has been shown to play a role in development, stem cell pluripotency, tumorigenesis, inflammation and also in ocular diseases manifestation (Li and Seto 2016; Liu et al. 2013; Yang et al. 2006).

1.7.4 H3 Histones

Histone H3 family contains 216 different members characterized from various species (http://www.actrec.gov.in/histome/). Several mammalian sequence variants of H3 have been found to be encoded by this cluster of genes (Biterge and Schneider 2014). Eight histone H3 variants have been reported in humans (Vardabasso et al. 2014).

Histone H3 is the most extensively post-translationally modified of the five histones (Sadakierska-Chudy et al. 2015). H3 histones consists of a N-terminal, globular domain and C-terminal (Ramaswamy and Ioshikhes 2013). The globular domain of H3 spans from a proline residue at position 38 to glycine 132. The globular domain comprises of “histone fold” motif, a structure of three α helices (α1: K64- F78, α2: S86-A114, α3: P121-R131) connected by the loops L1 and L2. Within the globular domain, the post-translational modifications are restricted to the borders of the helices, the loops between individual helices (Tropberger and Schneider 2010).

The H3 barcode model postulates a crucial role for H3 histones to index genomic information and ensure epigenetic memory. Short-term alterations in gene expression is achieved by histone H3 post translational modifications (PTMs) but long-term establishment (epigenetic memory) of gene expression involves stable incorporation of the appropriate histone H3 variants (Hake and Allis 2006). Histone genes encoding these variants can be classified into two main subtypes: canonical and replacement variants on the basis of their expression pattern and genomic organization (Hake and Allis 2006).

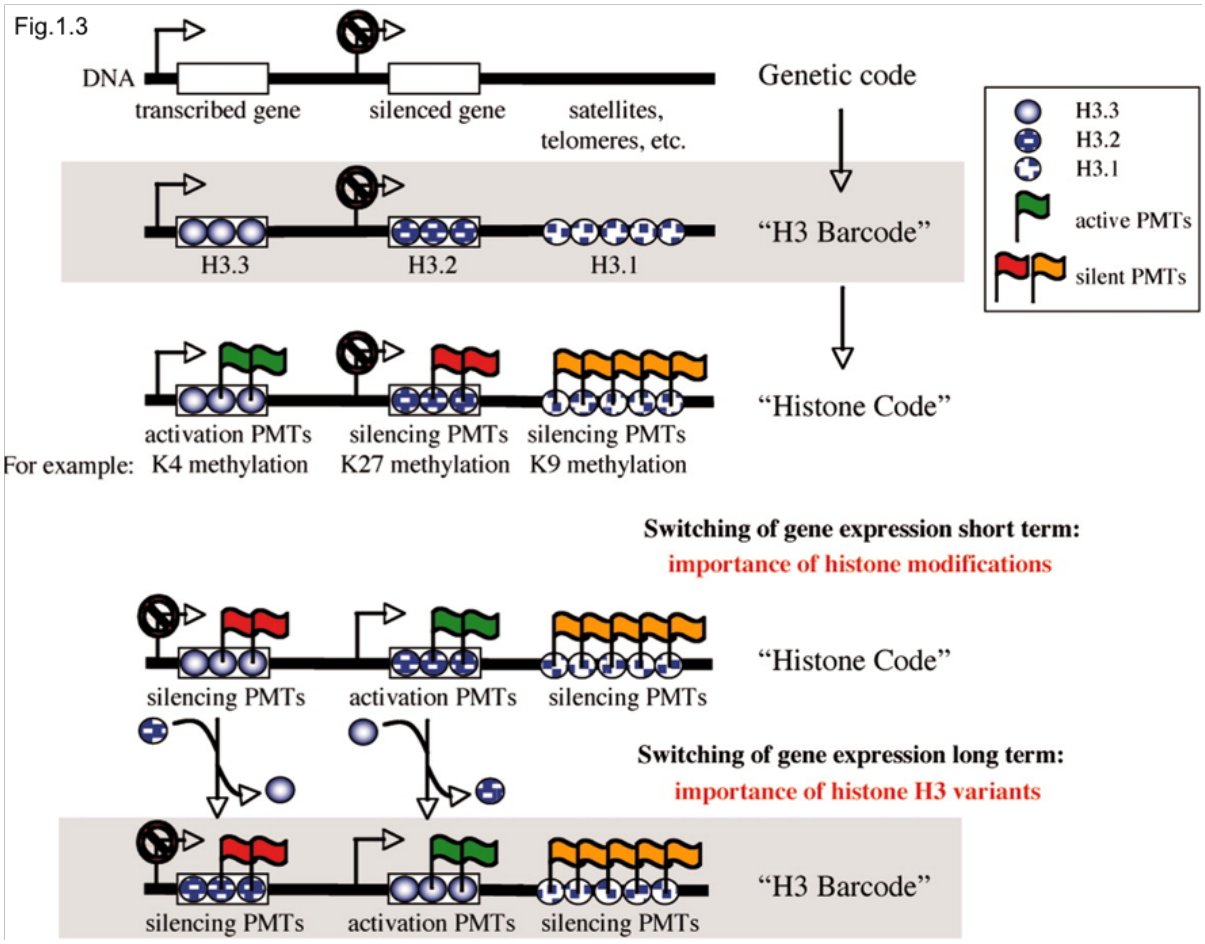

Fig.1.3: **H3 barcode model to index genomic information and ensure epigenetic memory.** DNA contains genetic information in the form of genes (white boxes) that have to be activated or silenced at appropriate times and noncoding regions, such as centromeres, telomeres, and satellites (dotted line). Actively transcribed genes contain H3.3 (blue gradient circle) in their chromatin, whereas silenced genes have H3.2 (blue circle with white dots) incorporated. A majority of DNA does not contain any meaningful genetic information and also genes, which are constitutively silent. These genomic regions are indexed by the presence of H3.1 (white circles with blue dots) in the chromatin. The next regulatory step to ensure proper gene expression is the regulation of genes with posttranslational histone modifications (green flag, activation PMTs; red and orange flags, different silencing PMTs). We propose that short-term alterations in gene expression is achieved by the employment of specialized PMTs (e.g., acetylation), but long-term establishment (epigenetic memory) of gene expression involves more stable histone modifications as well as the incorporation of the appropriate histone H3 variants. Adapted from Hake and Allis 2006 under © 2006 National Academy of Sciences.

1.7.5 Canonical H3 variants:

Expression of canonical H3 variants is directly linked to DNA replication during S-phase of the cell cycle and are hence termed as the replication-dependent or canonical group of H3 proteins (Szenker et al. 2011). Genes encoding canonical histones have no introns and are organized in tandem, multicopy clusters (Marzluff et al. 2002). Most of the histone genes in the mammalian genome are replication dependent. Replication-dependent histone mRNAs are not polyadenylated and end in a conserved stem-loop (Marzluff and Koreski 2017). The translation of the replication-dependent histones is tightly regulated to the cell cycle by the binding of the stem loop binding protein, and U7 small nuclear RNA to the 3′ end of the replication-dependent histone mRNA (Marzluff and Koreski 2017). Histones H3.1 and H3.2 are canonical histones and differ by only one amino acid from each other. Because of the high sequence conservation amongst H3.1 and H3.2, most studies tend to group these variants as one (Hake and Allis 2006). In addition, the existence of multiple encoding genes for the canonical histones has resulted in technical complexity in analyses of the canonical variants (Henikoff and Smith 2015).

H3.1:

H3.1 is incorporated mainly in constitutively silenced loci. H3.1 has been shown to be incorporated outside of the S phase in the event of DNA repair after UV lesion (Polo et al. 2006). K27M substitution in *HISTH3.1* gene encoding H3.1 was also found in some of the samples from pediatric glioblastomas patients (Huang et al. 2018).

H3.2:

H3.2 are dominantly incorporated in facultative heterochromatin. H3.2 is enriched in PTMs associated with gene silencing, K27 di- and trimethylation (Hake et al. 2006). The canonical variant H3.2 has been found to occupy heterochromatin sites in mice embryos throughout the preimplantation stage, *i.e.*, from the one-cell stage through the blastocyst stage. This expression is a requisite to achieve the epigenetic reprogramming required for development (Akiyama et al. 2011).

1.7.6 Replacement H3 variants:

Expression of replacement H3 variants is generally not upregulated during DNA replication and their incorporation involves local replacement of an existing nucleosome or subunit (Szenker et al. 2011). The variants are incorporated into the nucleosomes throughout the whole cell cycle. Replacement variant genes possess introns and their mRNAs are polyadenylated (Marzluff and Koreski 2017). H3.3, H3t (H3.4), H3.5, and CENP-A belong to this type. The genes encoding specific replacement variants are fewer (e.g H3.3 is encoded

by 2 genes, compared to 8 genes encoding H3.2) and the individual variants are structurally diverse (Sadakierska-Chudy et al. 2015). This structural divergence has led to specific studies on the individual histone variants.

H3.3

H3.3 is structurally close to the canonical H3 histones and differs by 4 amino acid differences from H3.2 and by 5 amino acids from H3.1 (Szenker et al. 2011). These non-identical residues have been found to be essential for H3.3 depositions. This is also corroborated by altered genome-wide distribution of H3.3 upon mutation of the H3.3 coding sequence to the canonical H3.2 in mouse embryonic stem (ES) cells (S. B. Hake and Allis 2006). H3.3 has been established to have an important role in reproduction and early development. This is seen by the phenotypic effects of display reduced growth rates, neuromuscular deficits, and male infertility in H3.3 mutant mice (Jang et al. 2015; Welby et al. 2019). Missense mutations in the *H3.3* coding gene were observed in 31 % of pediatric Glioblastoma samples representing the first evidence of a histone variant-encoding gene mutated in human cancer (Sadakierska-Chudy et al. 2015; Schwartzentruber et al. 2012). H3.3 replaces most of the canonical H3 in non-dividing cells in a time-dependent manner during development and the chromatin is saturated with H3.3 histones in adult tissues (Bano et al. 2017; Tvardovskiy et al. 2017). It has been proposed to participate in the epigenetic transmission of active chromatin states (Szenker et al. 2011).

CENP-A:

Amongst the histone H3 variants the centromere protein A (CENP-A) is the longest variant and share no sequence similarity with canonical H3 (Hake and Allis 2006; Mariño-Ramírez et al. 2005).The variant is specifically localized to centromeric chromatin (De Rop et al. 2012). The centromere-specific localization is also maintained during the transition from histones to protamines during spermatogenesis, when all other histones are lost (Palmer et al. 1991). CENP-A has been found to be essential for kinetochore assembly and centromere propagation. CENP-A nucleosome composition was found to be dynamic through the cell cycle (Henikoff and Smith 2015). *Cenpa* null mice fail to survive beyond 6.5 dpc (days post coitus) due to severe mitotic defects (Howman et al. 2000). CENP-A was found to be upregulated in breast cancer, colorectal cancer, hepatocellular carcinoma lung adenocarcinoma and testicular tumors (Sadakierska-Chudy et al. 2015).

H3T/H3.4

H3.4 is a testis-specific H3 variant robustly expressed in the testis and primary spermatocytes (Skene and Henikoff 2013). During spermatogenesis, H3t appears and replaces the canonical

H3 proteins in differentiating spermatogonia (Ueda et al. 2017). Structural analyses revealed that H3t-containing nucleosomes are more flexible than the canonical nucleosomes (Tachiwana et al. 2008). *H3t* gene deficiency leads to azoospermia because of the loss of haploid germ cells (Ueda et al. 2017).

H3.5

H3.5 protein is expressed in seminiferous tubules and around transcription start sites (TSSs) in testicular cells (Shiraishi et al. 2018). Biochemical analyses revealed that the H3.5-specific Leu103 residue is responsible for the instability of the H3.5 nucleosome, both in-vitro and in living cells (Urahama et al. 2016). Ectopic H3.5 expression complemented the growth defect in *H3.3* knockdown cells by incorporating into euchromatic region suggesting that H3.5 may have an overlapping function with H3.3 as a replacement histone (Schenk et al. 2011).

1.7.7 Post-translational modifications in histones

Histone post-translational modifications have been researched extensively since their pioneering discovery in the early 1960s (Allfrey et al. 1964; Stillman 2018). Allfrey et al. initially identified that acetyl and methyl groups could be post translationally added to histones and these modifications correlated with gene expression (Allfrey et al. 1964). Consequently, through a combination of techniques involving ChIP-Seq, modification specific antibody and Mass spectrometric based detection a plethora of histone PTMs have been identified and characterized (Stillman 2018; Su et al.2007). These include the common/well characterized PTMs, acetylation, methylation, and phosphorylation in Histone tails as well as lesser-studied modifications such as succinylation and modification in globular domain of the histones (Stillman 2018).

Histone acetylation has been the most studied PTM (Kelly et al. 2018). In H3 from most species, the main acetylation sites include lysines 9, 14, 18 and 23. H3 acetylation in the amino termini plays a fundamental role in transcriptional regulation (Strahl and Allis 2000). Acetylation in H3K56, H3K79, H3K64, H3K115 and H3K122 of the globular domain in H3 have also been identified *in-vivo* (Kebede et al. 2014; Tropberger and Schneider 2010). Histone acetylation neutralizes the positive charge mediating the interaction of the unmodified side chains of these residues with the negatively charged backbone of the DNA (Taverna et al. 2007).

Histone phosphorylation is associated with chromosome condensation during mitosis (Strahl and Allis 2000). H3 phosphorylation is directly correlated with the induction of

immediate-early genes such as c-jun, c-fos and c-myc (Clayton et al. 2000). Mutations in *Rsk-2* (Ribosomal S6 kinase 2), H3 kinase are associated with Coffen-Lowry syndrome in humans and result in a loss of epidermal growth factor-stimulated H3 phosphorylation *in-vivo* (Hanauer and Young 2002). H3T118 is the site of phosphorylation in the globular region and lies in the regions with the strongest DNA-histone interaction within the nucleosome. Nucleosomes reconstituted with phosphorylated H3T118 aggregate to anomalous nucleosomal structures (Kebede et al. 2014; Tropberger and Schneider 2010).

Histone Methylation is the least understood histone post-translational modifications. H3 and H4 are the predominant histones modified by methylation, and the multiple lysines in H3 (4, 9 and 27) are the preferred sites of methylation (Strahl and Allis 2000). Histone methylation is known to contributes to transcriptional activation. Methylation of H3K56, H3K64, H3K79 and H3K122 in globular region has also been observed *in-vivo*. But the functional significance of this has not been characterized extensively.

Most of the histone PTMs represent transient marks for gene regulation, however some modifications at silent chromatin regions have functions outside transcriptional regulation (Kubicek et al. 2006). For example, Histone PTMs specifically H3K9me1 play a role in maintaining the boundary between euchromatin and heterochromatin in eukaryotic genome (Bannister and Kouzarides 2011). In addition, there is a complex interface between Histone PTM and metabolism through the donor for the histone PTMs. Particularly, the principal donor for the acetyl marks is acetyl-CoA from cellular metabolism and genome-wide H3 acylation profiles were altered upon deletion of the metabolic enzyme propionyl-CoA. It has been postulated that histone PTMs are coupled to cellular metabolism and have complex regulatory patterns (Kebede et al. 2017; Stillman 2018). Finally, non-nucleosomal PTMs control specific deposition patterns of their constituent histone. Non-nucleosomal H3.1 and H3.3 carry a distinct set of modifications before their deposition, which in turn determine their final PTMs in nucleosomes (Loyola et al. 2006; Szenker et al. 2011).

PTMs regulate transcription via two main mechanisms (Bannister and Kouzarides 2011): Chromatin structure modification and regulation of the binding of effector molecules.

- **Chromatin structure modification**

Charge-dependent interactions at key residues that are subject to post-translational modifications can have profound effects in chromatin structure by affecting internucleosomal interactions. They do so through diverse effects on DNA-histone interaction, nucleosomal mobility and stability (Marino-Ramírez et al. 2005; Mersfelder and Parthun 2006). For

example, histone acetylation and phosphorylation effectively reduce the positive charge of histones, and this has the potential to disrupt electrostatic interactions between histones and DNA. This presumably leads to a less compact chromatin structure, thereby facilitating DNA access by protein machineries such as those involved in transcription (Mariño-Ramírez et al. 2005; Taverna et al. 2007). Histone PTMs also exhibit positive and negative crosstalk with their neighboring PTMs for coordinated transcriptional regulation (Stillman 2018; Strahl and Allis 2000). For instance, the histone PTMs H3S10P and acetyl H3K14 at the p21 (*CDKN1A*) gene locus activates transcription, and the activation does not occur when only one of the two PTMs are present (Schwämmle et al. 2016).

- **Regulation through effector molecules.**

Numerous chromatin-associated factors have been shown to specifically interact with modified histones via many distinct domains. These include ‘‘reader’’ proteins that recognize specific histone marks and ‘‘writer’’ proteins that create the modifications (Stillman 2018). Many of the effectors are now drug targets for a variety of diseases, including ocular disorders (Yan et al. 2014). The effector molecules are typically multivalent proteins and complexes for the simultaneous recognition of several modifications and other nucleosomal features. For example, Swi2/Snf2 contains a bromodomain that targets it to acetylated histones. In turn, this recruits the SWI/SNF remodeling complex, which functions to 'open' the chromatin (Bannister and Kouzarides 2011).

Thus histone PTMs strongly influences accessibility of specific DNA sequences for trans-acting factors and cis acting elements thereby affecting transcriptional regulation (Schwämmle et al. 2016). Histone PTMs based transcriptional regulation play a fundamental role in embryonic development from early stages of fertilization to tissue specific differentiation (Cantone and Fisher 2013). In addition, Histone PTMs can be inherited through the cell cycle thereby maintaining a memory of gene expression profiles (Kawabata et al. 2019; Vastenhouw and Schier 2012). Epigenetic asymmetry of the histone PTMs with respect to time and tissue type drive cell fate during embryonic development. For example, in 4-cell embryo stage, one of the four blastomeres shows lower levels of methylated H3K27; while high levels of this mark are observed this was found to be prerequisite for upregulation of Nanog and Sox2, and the resultant Inner Cell Mass (ICM) fate (Canovas and Ross 2016). Also during embryonic development there is a shift from histone H3 modifications associated with transcriptional activity to transcriptionally repressive H3 marks (Schneider et al. 2011).

1.7.8 H3 histones modifications in ocular development:

The ocular system represents an ideal system to both genetic and epigenetic modes of gene regulation at the molecular level as regulatory genes are among the best understood in mammalian systems (Cvekl and Mitton 2010). Interestingly, epigenetic regulatory mechanisms have been receiving more attention in the recent years and various epigenetic systems modified have been characterized in ocular diseases of cataract, glaucoma and age-related macular degeneration (Alkozi et al. 2017; Cvekl and Duncan 2007; Liu et al. 2013; Pennington and Deangelis 2015). The functional significance of post-translational modifications in histone H3 family observed till now are postulated below:

- SOX11 regulates the transcription of genes crucial to retinal subtype differentiation through histone H3 acetylation in early proneural genes (Usui et al. 2013).
- High levels of histone H3K9 acetylation are seen in αA-crystallin coding regions involved in CREB-dependent activation of *Pax6*. This signaling at Distal Control Regions (DCR) leads to chromatin remodeling of the αA-crystallin locus in the lens placode (Yang et al. 2006).
- Methylation in lysine 4 and 27 on histone H3 (H3K4me3 and H3K27me3) were detected primarily in differentiated retinal neurons in the embryonic and adult retina (Popova et al. 2012).
- The lenses of CX50D47A congenital cataract mice have elevated levels of H3 histone (Berthoud et al. 2013b).
- Dimethyl lysine 9 on histone H3 (H3K9me2) is seen in early differentiating retinal ganglion cells (Rao et al. 2010).
- The H3-histone modifications namely H3K9me3 and H3K20me3 form a point of nuclear reorganization as an adaptation to improve night vision during postnatal growth (Solovei et al. 2009).

Concurrently studies on the specific nature of the histone subtype carrying these modifications is still lacking to the best of my knowledge.

1.7.9 *Hist2h3c1*

Hist2h3c1 refers to the histone gene cluster 2 at mouse chromosome 3 coding for the first copy (c1) of histone variant H3.2 (Marzluff et al. 2002). *Aey69* mice carry a mutation in *Hist2h3c1* (Vetrivel et al.2019). This distinct mutation has not been found to be associated with any other disorders until now. The reported mutation is at amino acid position 120 in the loop region of H3.2 (Fig.1.2). In addition, the mutation site is surrounded by regions that are

marked with prominent H3 post-translational modifications (Tropberger and Schneider 2010). Therefore, possible structural changes in the nucleosome containing the mutation could also be hypothesized. Thus, the mutant mouse and the phenotypic changes postulate unexplored vital roles of the gene and the protein.

1.8 Objectives of the study

Aey69 represents an interesting mouse line for extensive analyses of the altered eye developmental phenotype. Histological ocular characterization detailing the loss of lens and retinal overgrowth at postnatal stage raises several interesting questions. The question primarily encompasses the factors responsible for lens loss and characterization of the onset for retinal changes. Experiments based on these questions would help in characterizing the timeline of pathological changes associated with lens and retina in *Aey69*. In addition, the dominant nature of the *Aey69* phenotype indicates a major role for any affected genes and its related pathways in ocular development. Concurrently, transcriptomic changes from the microarray data would further help in defining the candidate signaling molecules instrumenting pathology in *Aey69*.

The coexistence of *Gja8* and *Hist2h3c1* mutation in *Aey69* arises query on which of the genes are primarily responsible for *Aey69* ocular phenotype. A combined effect of action of both the genes also cannot be excluded. Hence, an ocular specific characterization of both *Gja8* and *Hist2h3c1* in *Aey69* is crucial. Compared to *Hist2h3c1*, *Gja8* has been fairly researched on it for its role in ocular system. Therefore, any analyses of *Hist2h3c1* could present the first description of its functions. In addition, the encoded protein H3.2 has been so far not been studied specifically in mammalian system. Therefore, transgenic approaches to evaluate *Hist2h3c1* encoded H3.2 would again signify the first documentation of the developmental role for H3.2.Finally, if *Hist2h3c1* is established to the indubitable primary link for microphthalmic phenotype, then the process by which the mutation affects the change needs to be analyzed. For the same the nature, effect and properties of the mutation should be analyzed with respect to the coded protein as well as the coded mRNA.Based on these salient points, objective of the study can be broadly categorized as:

1. Immunohistochemistry and expression based characterization of the *Aey69* microphthalmic phenotype.

2. Analysis of the mutant genes in *Aey69*.
3. Evaluation of the nature of mutation in *Hist2h3c1*.
4. Assessment of the role of *Hist2h3c1* encoded H3.2 in embryonic development.

2 Materials and Methods

2.1 Materials

2.1.1 Equipment

Apparatus	Product	Manufacturer
Agarose-Gel electrophoresis apparatus	Power supply	Biorad, Laboratoreis Inc., Herculus, U.S.A.
	Electrophoresis chamber	peQLab Biotechnologie GmbH, Erlangen, Germany
Balance	TE 1502S	Sartorius AG, Goettingen, Germany
	analytical	Sartorius AG, Göttingen, Germany
Camera for light microscope	Axiocam	Zeiss, Oberkochen, Germany
Capillary Electrophoresis	2100 Bioanalyzer	Agilent Technologies GmbH, Waldbronn, Germany
Centrifuge	Microfuge: Eppendorf 5415R	Eppendorf, Hamburg, Germany
	Microfuge: Biofuge pico	Heraeus, Osterode, Germany
	Minifuge: SD220	Carl Roth GmbH & Co. KG, Karlsruhe, Germany
	Benchtop: Sigma 3K18	Sigma Zentrifugen GmbH, Osterode am Harz, Germany
	Galaxy mini	VWR International Ltd Lutterworth, England
FPLC purification	Äkta	GE Healthcare Europe GmbH, Penzburg, Germany
Freeze Vac	Concentrator plus complete system	Eppendorf, Hamburg, Germany
Fume hood	Variolab Mobilien W 90	Waldner Laboreinrichtungen GmbH & Co. KG, Wangen, Germany
Gel documentation system	Argus X1	Biostep GmbH, Jahnsdorf, Germany
	Peqlab Fusion SL	ANALIS Nv Netherland, Amsterdam, Netherlands
Heating plate	Ikamag	Ludwig Empfenzeder, Munich, Germany
Incubators	(CO_2)-Teco 20	Selutec GmbH, Hechingen, Germany

	Celsius 2007	Memmert, Schwabach, Germany
Laminar Flow cabinet	Laminar flow cabinet	Gelaire Pty Ltd., Sydney, Australia
Luminometer	Centro LB 960	Berthold Technologies GmbH & Co. KG, Bad Wildbad, Germany
Microscope	Light: Axioplan2	Zeiss, Oberkochen, Germany
	Light: Axiovert 35	Zeiss, Oberkochen, Germany
	Fluorescence: DMI 6000B	Leica Microsystems GmbH, Wetzlar, Germany
	Olympus confocal microscope fv1000	Olympus, Hamburg, Germany
	EVOS™ FL Imaging System	ThermoFisher Scientific, Schwerte, Germany
Microtome	RM2050	Leica Microsystems, Wetzlar, Germany
Microwave	M1712N	Samsung Electronics GmbH, Schwalbach, Germany
pH Meter	pH Meter 761 calimetic	Knick, Berlin, Germany
	Hanna Instruments H12211	Hanna Instruments Germany GmbH, Vöhringen, Germany
Pipette	Pipetman (2µl, 10µl, 20µl, 200µl, 1ml)	Gilson S: A.S., Villiers-le-Bel, France
Pipette aid	Macro-612-1900	VWR International Ltd Lutterworth, England
Safe seal tips	Biozym SafeSeal Tips Precision filter tips (2µl, 10µl, 20µl, 200µl, 1ml)	Biozym Scientific GmbH, Oldendorf, Germany
Shaker	Platform: Polymax 1040	Heidolph Instruments GmbH & Co. KG, Schwabach, Germany
	Orbital: Rotamax 120	Heidolph Instruments GmbH & Co. KG, Schwabach, Germany
	Centromat S	Braun Melsungen AG, Germany
Spectrophotometer	Nanodrop: ND1000	peQLab Biotechnologie GmbH, Erlangen, Germany
	Biophotometer	Eppendorf AG, Hamburg, Germany

Sonicator	Q500	Thomas Scientific, Swedesboro, New Jersey, United States
	Q800R	Qsonica, New York, United States
Thermal cycler	Step one (Realtime)	Applied Biosystems, Darmstadt, Germany
	Flexcycler	Analytik Jena AG, Jena, Germany
	BIOER LifeECxO Systems	Biozym Scientific GmbH, Oldendorf, Germany
	Mastercycler pro, Vapoproject	Eppendorf, Wesseling-Berzdorf,Germany
Thermomixer	7410	Bachofer, Reutlingen, Germany
	5436	Eppendorf, Hamburg, Germany
Vortex	G-560E Vortex-2-GENIE	ThermoFisher Scientific, Schwerte, Germany
Water bath	Julabo F12 MP	JULABO GmbH, Seelbach, Germany
Water purification system	MilliQ biocel	Millipore, Schwalbach, Germany

2.1.2 Consumables

Item	Catalog no.	Manufacturer
Concentrator	Amicon Pro Purification systems	Merck Chemicals GmbH, Darmstadt, Germany
Coverslips	H878	Carl Roth GmbH & Co. KG, Karlsruhe, Germany
Dialysis tubing (6- to 8-kDa cutoff, 2.5- to 4-cm flat width)	Spectrum™ Spectra	ThermoFisher Scientific, Schwerte, Germany
Disposable cuvettes	UVetta	Eppendorf, Hamburg, Germany
Fast 48-well reaction plates	437523	ABI, Foster City, U.S.A.
FPLC columns	ResourceS,Superdex 200	GE Healthcare Europe GmbH, Penzburg, Germany
Glass Slides	Superfrost® Plus	Gerhard Menzel GmbH, Braunschweig, Germany

Nitrocellulose membranes	10600002	GE Healthcare Europe GmbH,Penzburg,Germany
Parafilm	4621.1	Carl Roth GmbH & Co. KG, Karlsruhe, Germany
Petri dishes	633180	Greiner Bio-One GmbH, Frickenhausen, Germany.
Pipette tips	Filter	Biozyme Inc. St. Joseph, U.S.A.
	sterile	Biozyme Inc. St. Joseph, U.S.A.
Sterile filter	Millex-GP	Millipore, Carrigtwonhill, Ireland
Tubes	0.2ml	Sarstedt, Nuembrecht, Germany
	2ml & 1.5 ml	Eppendorf, Hamburg, Germany
	15 ml&50 ml	Becton Dickinson GmbH, Heidelberg, Germany
Weighing boats	A230	Carl Roth GmbH & Co. KG, Karlsruhe, Germany

2.1.3 Commercial kits

Kit	Catalog no.	Company
1 kb ladder	SM0311	Fermentas GmbH, St. Leon-Rot, Germany
100 bp ladder	SM0241	Fermentas GmbH, St. Leon-Rot, Germany
Agilent DNA 1000 Kit	5067-1504	Agilent Technologies GmbH, Waldbronn, Germany
BioZym cDNA synthesis kit	331470X	Biozym Scientific GmbH, Oldendorf, Germany
DreamTaq Green PCR Master Mix	K1081	Fisher Scientific GmbH, Schwerte, Germany
Nucleospin® Extract II	740609.50	Nucleospin, Macherey-Nagel, Dueren, Germany
Nucleospin® plasmid	740588.50	Nucleospin, Macherey-Nagel, Dueren, Germany
Omniscript RT Kit	205111	Qiagen GmbH, Hilden, Germany
pCRII Topo cloning Kit	K462001	Invitrogen, Darmstadt, Germany
Qubit dsDNA HS Assay Kit	Q32854	ThermoFisher Scientific, Schwerte, Germany

RNA extraction	74104	Qiagen GmbH, Hilden, Germany
RNeasy Plus Mini Kit	74134	Qiagen GmbH, Hilden, Germany
Roti-Lumin kit	P078.2	Roth, Karlsruhe, Germany
SensiFAST SYBR Hi-ROX Kit	BIO-92005	Bioline GmbH, Luckenwalde, Germany
StrataClone Blunt PCR Cloning Kit	240207	Agilent Technologies GmbH, Waldbronn, Germany
X-tremeGENE HP DNA Transfection Reagent	XTGHP-RO	Sigma-Aldrich, Deisenhofen, Germany
ZymoSpin ChIP Kit	D5209	Zymo Research, Freiburg, Germany

2.1.4 Biological materials

Enzyme	Manufacturer
*Bam*HI-HF	New England BioLabs GmbH, Frankfurt am Main, Germany
*Bbs*I	New England BioLabs GmbH, Frankfurt am Main, Germany
C57BL6/N, CD1 mice	Charles River, Sulzbach, Germany
Cas9 Protein	Integrated DNA Technologies Inc., Munich, Germany.
crRNA	Integrated DNA Technologies Inc., Munich, Germany.
DH5α	Invitrogen, Darmstadt, Germany
DNase1	Qiagen GmbH, Hilden, Germany
*Dpn*I	New England BioLabs GmbH, Frankfurt am Main, Germany
Hind III	New England BioLabs GmbH, Frankfurt am Main, Germany
KOD Hot Start DNA Polymerase	Merck Millipore, Darmstadt, Germany
N2A cell line	ATCC, Wesel, Germany
*Nde*I	New England BioLabs GmbH, Frankfurt am Main, Germany
pET-21a(+) vector	Gift from Dr.Schneider, Institute of Functional Epigenetics, Helmholtz Zentrum Munich (HMGU)
pMB_Cas9v2 vector	Gift from Dr.Giesert, Transgenic Unit, Institute of Developmental Genetics, HMGU
Proteinase K	Applichem GmbH, Darmstadt, Germany

Rosetta(DE3)pLysS	Gift from Dr.Geerlof, Protein Expression & Purification Facility,
RNase A	Carl Roth GmbH & Co. KG, Karlsruhe, Germany
RNase free DNase1	Qiagen GmbH, Hilden, Germany
Taq DNA polymerase	Invitrogen, Darmstadt, Germany
tracrRNA	Integrated DNA Technologies Inc., Munich, Germany

2.1.5 Chemicals

Chemical	Catalog no.	Manufacturer
Agarose	840004	Biozyme Scientific GmbH, Oldendorf, Germany
Ampicillin	K029.1	Carl Roth GmbH & Co. KG, Karlsruhe, Germany
β-Mercaptoethanol (BME)	M7522	Sigma-Aldrich, Steinheim, Germany
Boric Acid	A2940	Applichem GmbH, Darmstadt, Germany
Bovine Serum Albumin	A1152	Sigma-Aldrich, Deisenhofen, Germany
Citric acid	X863.2	Carl Roth GmbH & Co. KG, Karlsruhe, Germany
Difco LB-agar Miller	244520	Becton Dickinson & Company, Sparks, USA
Difco LB-Base Miller	241420	Becton Dickinson & Company, Sparks, USA
Dulbecco's Modified Eagle Medium (DMEM)	E15-806	PAA Laboratories GmbH, Pasching, Austria
dNTPs	R0241	Fermentas GmbH, Leon-Rot, Germany
EDTA	8043.2	Carl Roth GmbH & Co. KG, Karlsruhe, Germany
Ethanol	2246.2500	Th. Geyer GmbH & Co. KG Renningen, Germany
Fetal bovine serum (FBS)	A15-104	PAA GmbH, Pasching, Austria
Glycerol	1.04093	Merk KGaA, Darmstadt, Germany
Glycine	G7126	Sigma-Aldrich Chemie, Steinheim, Germany
HCl	1.00319	Merk KGaA, Darmstadt, Germany
IPTG (Isopropylthio-β-D-Galactoside)	2316.3	Carl Roth GmbH & Co. KG, Karlsruhe, Germany
Methanol	1.06009	Merk KGaA, Darmstadt, Germany
Protease and phosphastase Inhibitors	MSSAFE	Sigma-Aldrich, Steinheim, Germany
NaAc	1.06268	Merk KGaA, Darmstadt, Germany
NaCl	1.06404	Merk KGaA, Darmstadt, Germany

NaOH	1.06482	Merk KGaA, Darmstadt, Germany
Opti-MEM I	31985062	ThermoFisher Scientific, Schwerte, Germany
PFA	0335.3	Carl Roth GmbH & Co. KG, Karlsruhe, Germany
Pierce 16% formaldehyde (w / v), methanol-free	28960	ThermoFisher Scientific, Schwerte, Germany
Protein A/G PLUS-Agarose	sc-2003	Santa Cruz Biotechnology Inc, Heidelberg Germany
Pierce™ Protein A/G Plus Agarose	20423	ThermoFisher Scientific, Schwerte, Germany
RNase Zap	R2020	Sigma-Aldrich, Steinheim, Germany
Roti-Histol	6640	Carl Roth GmbH & Co. KG, Karlsruhe, Germany.
Roti-Mount	HP19	Carl Roth GmbH & Co. KG, Karlsruhe, Germany.
Sodium Citrate	3580.1	Carl Roth GmbH & Co. KG, Karlsruhe, Germany.
Sodium dodecyl sulfate (SDS)	20760	Serva Feinbiochemica GmbH & c. KG, Heidelberg, Germany
Sodium phosphate dibasic	1.06580	Merk KGaA, Darmstadt, Germany
Sodium phosphate monobasic	1.06346	Merk KGaA, Darmstadt, Germany
Sucrose	4621.1	Carl Roth GmbH & Co. KG, Karlsruhe, Germany.
Trizma Base	1.08382	Merk KGaA, Darmstadt, Germany
Trypsin-EDTA (0.05 %)	25300	Invitrogen, Darmstadt, Germany
Tween 20	9127.1	Carl Roth GmbH & Co. KG, Karlsruhe, Germany.
Water	1.15333	Merk KGaA, Darmstadt, Germany
X-gal	R0404	Fermentas GmbH, Leon-Rot, Germany
Xylene	1.08685	Merk KGaA, Darmstadt, Germany

2.1.6 Buffers and Solutions

Buffer	Components
Microinjection buffer	5 mM Tris-HCl, 0.1 mM EDTA pH 7.2
Refolding buffer	10mM Tris pH 7.5, 1mM EDTA pH 8.2M, NaCl, 5mM B-ME
RIPA lysis and extraction buffer	Commercial preparation from ThermoFisher Scientific, Schwerte, Germany. Catalog no.89900
SAU-200 buffer	7M urea, 20mM Sodium Acetate pH 5.2, 200mM NaCl, 1mM EDTA pH 8, 5mM B-ME

SAU-600 buffer	7M urea, 20mM Sodium Acetate pH 5.2, 600mM NaCl,1mM EDTA pH 8, 5mM B-ME
Sodium Citrate buffer	0.04 M Sodium Citrate dehydrate, 0.06 M Citric Acid pH 6
SDS gel loading buffer	Commercial preparation from Roth, Karlsruhe, Germany. Catalog no. K930.1
TE buffer	10mM Tris, 0.5mM EDTA pH 7.5,1mM DTT
TNE DNA lysis buffer	100 mM Tris-HCl pH 7.5, 0.5 mM EDTA, 150 mM NaCl
Unfolding buffer	7 M guanidinium-HCl, 20 mM Tris-HCl pH 7.5,10 mM dithiothreitol (DTT)
Wash buffer	50 mM Tris-HCl (pH 7.5), 100 mM NaCl, 1 mM benzamidine, 5 mM 2-BME,1mM EDTA (pH-8)

2.1.7 Software and tools

Software / Tool	website
EaSeq	https://easeq.net/citation/
GrammX	http://vakser.compbio.ku.edu/resources/gramm/grammx/
gRNA design, Broad Institute	https://portals.broadinstitute.org/gpp/public/analysis-tools/sgrna-design Broad Institute of Harvard and Massachusetts Institute of Technology, Cambridge, Massachusetts, USA
iGNM	http://ignm.ccbb.pitt.edu/
ITASSER	https://zhanglab.ccmb.med.umich.edu/I-TASSER/
MACS	http://liulab.dfci.harvard.edu/MACS/
Microsoft office version 15.23	http://www.microsoft.com/
NCBI	http://www.ncbi.nlm.nih.gov/
OligoIDT online tool	https://eu.idtdna.com/site/account/login?returnurl=%2Fcalc%2Fanalyzer Integrated DNA Technologies, Leuven, Belgium
PATCHDOCK	https://bioinfo3d.cs.tau.ac.il/PatchDock/
Primer BLAST	https://www.ncbi.nlm.nih.gov/tools/primer-blast/
Pymol Molecular Graphics System version 0_99rc6, 2010	https://pymol.org/2/
QUARK	https://zhanglab.ccmb.med.umich.edu/QUARK/
Real time PCR analysis: REST	http://www.REST.de.com Qiagen, Hilden, Germany

Sequence and gene analysis: Benchling	https://benchling.com
StepOne™ Real time PCR sytem data collection and analysis	https://www.appliedbiosystems.com Applied Biosystem Deutschland GmbH, Darmstadt, Germany
UCSC Genome Browser	https://genome.ucsc.edu/cgi-bin/hgTracks?db=mm10&lastVirtModeType=default&lastVirtModeExtraState=&virtModeType=default&virtMode=0&nonVirtPosition=&position=chr17%3A62777079%2D62785745&hgsid=731907037_HAvgIQu5adRbEN7haERC3NrahqnE

2.1.8 Primers

All primers were synthesized by Sigma-Aldrich, Steinheim, Germany.

Table 1: gRNA sequences and oligos ordered for cloning.

gRNA	Sequence with PAM	Oligos with overhangs (bold)
5'gRNA	GAGCGACAACAAACTACCAG**GGG**	**CACC**GGAGCGACAACAAACTACCAG
		AAACCTGGTAGTTTGTTGTCGCTCC
3' gRNA	ATGTTAGAAGAGGAATGCAG**AGG**	**CACC**GATGTTAGAAGAGGAATGCAG
		AAACCTGCATTCCTCTTCTAACATC

Table 2: Primers for Overlap PCR: SNP analysis

Region in NC_000069.6	Sequence (5'- 3')	Annealing (°C)	Polymerase	Product size (bp)
96245270-96246339	AGGAGAAACAGCGAGCAG	57.8	DreamTaq	1088
	GCCTAGACGTCCTAGTTGA			
96246170-96247048	CCTGGTAGTTTGTTGTCGC	62.0	KOD	896
	CTCGGTCGACTTCTGGTA			
96246769-96247590	AGTTTCAAGTCGCTGTCTCC	62.9	DreamTaq	845
	GTCAAATTACATTAGAAGGGAACG			
96247422-96248201	GTGCTTACTGTCCACCGA	62.9	DreamTaq	794
	AGTGACAGTGAGAAACCTTGC			
96248056-96248840	GAAGTTCCTTGTCCTTTGCTCA	62.9	DreamTaq	805
	ACCCAACAGCACACTATGAAG			

96244843-96248915	CACAGACGCCTCCGATGCTG	75.0	KOD	4073
	ACAGAGCTGTTCGTGCGCTG			

Table 3: Primer sequences and respective overlaps for donor plasmid cloning

Region	Sequence(5'- 3')	Overlap (bold)
5' Homology Arm	GTAATACGACTCACTATAGGGCGAATTGGAG CTCACAGACGCCTCCGATGCTG	
	GAACCAAAGAGCGACAACAAACTACCAGGC GGAACCACGGGCAGG	With Gene
Hist2h3c1 Gene	CCTGGTAGTTTGTTGTCGCTCTTTGGTTCATG	
	GCGCGCTCCCCACGGATGCGGCGGGCCAAC TGGATGTCCTTGGGCATGAGGGTGACGCGTT TGGC	With GFP
GFP	GCATCCGTGGGGAGCGCGCT	
	GGAATGGATGGGAGACAGGGCGC	With 3' Homology Arm
3' Homology Arm	GCGCCCTGTCTCCCATCCATTCC	
	CCCTCACTAAAGGGAACAAAAGCTGGCACAG AGCTGTTCGTGCGCT	

Table 4: Primers used for mutant plasmid cloning

Primer	**Sequence**	**Annealing (°C)**	**Product size (bp)**
SDM	ATCCAGGTGCTCAACGTCTGCATTCCTCTTC	75.0	9179
	GAAGAGGAATGCAGACGTTGAGCACCTGGAT		

Table 5: Genotyping Primers

Primers	Sequence (5'- 3')	Annealing (°C)	Polymerase	Product size (bp)
Founder primers	CACAGACGCCTCCGATGCTG	73.0	KOD	2700
	GCCACAAACGGAAAGCTGACCC			
Breeding generation primers	TACCAGAAGTCGACCGAGCTGC	67.0	DreamTaq	439
	GCCACAAACGGAAAGCTGACCC			

Table 6: Primers used for QPCR and ChIP-QPCR

All primers were used at an annealing temperature of 60 °C

Gene	Forward (5'- 3')	Reverse (5'- 3')
Atf1	AGACCTACCAGATCCGTACCA	GTCATCACCACGGTCTGC
B2m	GCAGAGTTAAGCATGCCAG	ATGATGCTTGATCACATGTCTCG
Bmp4	GCCCTCGACCAGGTTCATTG	GGAATGGCTCCATTGGTTCCT
Bmp7	CAGCCAGAATCGCTCCAAGA	GCTGTTTTCTGCCACACTGG
Bmpr1a	AGGTCAAAGCTGTTCGGAGA	CTGTACACGGCCCTTTGAAT
Brd2	GCCTCCTGGGTTGACCAAAT	CTCAGAGGAACTCTCACTGCTAC
c-Maf	CCCAGAGCCTTCTTCCCTTG	CATGTACAACGGGAGGCTGA
Car1	AGCCCACGATGCTGCACATGA	TGAGCGCCCACTCCATCCAC
Creb1	ACGGAAGAGAGAGGTCCGTC	GTTTTCAAGCACTGCCACTCTG
Crebrf	CCAAGAGAAGAGAGAGAACCCA	CCTTCAGCAGTCTTCCCTAACA
Crem	CGAGGTCCGCTACGTAAAC	CTTCGATCCTGCTGTGATTC
Dpp10	CAAGGGGATGACAGCCATGAAG	GGCTGTTACTTCCTAGTTCCTGGT
Efna3	ATACAAGGCAGCTGGGCAAT	AACGCTGCTTCTCTCGTAGG
Efna3-ChIP	AATGCACTTGCAATGCTGGG	AGCACACTTAGCAGCACCAT
Efna5	CTGGTGCTCTGGATGTGTGT	CCCTCTGGAATCTGGGGTTG
Efnb2	TGTGTGGAAGTACTGTTGGGG	TGTCCGGGTAGAAATTTGGAGT
Erdr1	CAGGACGGAGCGATTCTCAC	GGGGGACATTTCTGTACGCA
F13a1	ACTACCAGAGCACCCTCTCA	ATTGGAGTTATTGGGCGGGA
Foxc1	CGGATCGGCTTGAACAACTC	CGGTACAGAGACTGACTGGC
Hes5	GTGCAGAGTTGTCATTTGGGG	AAACACAAAACAACCCCACGG
Hist1h3b	GCAGGACTTCAAGACCGACC	GCACTTTGTTTCGTTTAAGCCC
Hist1h3c	ACTTTTGTGTATCTCCTCCCAAG	GTAGCGGTGAGGCTTCTTCA
Hist1h3d	ACCGTTCTCATTCCCTGAGAC	GTAGCGGTGAGGCTTCTTCA
Hist1h3f	CCGCTGTGGTATCGCCAA	ACTATTGCTTCCTCAGCCAC
Hist2h3b	GTATGGCCACTTGGCGTCTG	GTAGCGGTGCGGCTTCTTC

Hist2h3c1	CTTGCCTTAGTTAACACCCTCA	TTCAAGATTCTCCTTCTAGATTGTTAC
Hsf2	TTCCTGTTAGCAGAAACGGCA	CACACCCGGTCTCCACATTC
mmu-mir-204-5p	GCAGCCTTCCCTTTGTCATC	GTCTCCTCTGGTGCAGGGTCCGAGG TATTCGCACCAGAGGAGACAGGCAT
mmu-mir-5627-5p	CATAACAGAGGGTGCGCCG	GTCTCCTCTGGTGCAGGGTCCGAGG TATTCGCACCAGAGGAGACCGCAG
Pdpk1	TGCTGTGCAGTGACGTGG	CTGGAAGCGTCCTGGGTG
Pitpnm1	GCCTGGTGCAAGAGGTAGAA	ATGTAGGTCTGGCTCGGAGA
Pmp22	AAACCACTCACTGGAAACTCAA	GCAGTTATGAACCGTTTGTATCG
Psmd12	GCGACTGACGTTTTCAGCTC	TCTGATGTTGTGCTCCACCA
Rbbp7	CCAGACCGAACTCAGGCTTT	CTCGCTAGTCAAGAGCAGCC
Sdccag8	ATCAGCTTCTCCTGGAGCGA	CATGCTGGGTAACTGCGCT
Shisa6	AAGCAGACTCCAGGTGATCG	TCATGTGTAGGGGTCTGGGT
Smad1	TGAGCTTCGTGAAGGGTTGG	GATCTCAATCCAGCAGGGGG
Smad5	GCTGCGCTAAACTTTGTGACT	GAGGCGGGGAGTGACATTTA
Smarca4	CCACCCCTACATGTTCCAGC	GCACGGAGTTTGGGTAGAA
Smarca5	GCACCTCGACCTCCAAAAC	CATTGAGGGGCTCTGCTTC
Smarcad1	GATCAGTCTGTAAAACAGCCGC	GTGTACATCCACTCATGCTCC
Smarcc2	CCTGGCGTATCGGAACTTCA	GTCGGCTCTCAGCATCTACC
Smarcd1	GCCTATCCGAGACCAGGTA	CAGGTCGGACTGAAGGGTTC
Sparc	CATGAGGGCCTGGATCTTCTT	ATCTCCTCAGCAACTTCAGTCT
Tsc1	GCTCTCGGCTGATGTTGTTC	CAGAGACTAGCTTGCAGCG
Vax2	GCAGAGCAGCTGTATCGTCT	GGAACCAGACCTTCACCTGAG
Rplp0	ACTGGTCTAGGACCCGAGAAG	TCAATGGTGCCTCTGGAGATT
H3-all	TAAATCCACTGTGATATCGACTT CAAGACCGACCTGCGCTT	ATTATGCTGAGTGATATCTCGTGTGT GGCTCTGAAAAGAGCCT

Table 7: Primers used for H3.2 gene cloning into pET vector.

Primers	**Sequence (5'- 3')**	**Annealing (ºC)**	**Polymerase**	**Product size (bp)**
pET-primers	GGAATTCCATATGGCGCGGC AGCGCGGGAGT	65.0	KOD	408
	CGCGGATCCTTAAGCGCGCTC CCCACGGAT			

Table 8: Plasmid clones generated in the study.

All clones were selected by ampicillin resistance (100µg/ml) and verified by sanger sequencing (GATC Biotech, Konstanz, Germany)

Plasmid Name	Genes inserted	Insert Source	Vector Backbone	Vector Size without (w/o) Insert (bp)	Insert Size (bp)
H3.2-pET-21a(+)	H3.2 *Mus musculus* protein sequence	pSC_Crispr Donor_NC00069.6	pET-21a(+)	5800	409
mtH3.2-pET-21a(+)	H3.2 *Mus musculus* protein sequence	pSC_Crispr Mutant Donor	pET-21a(+)	5800	409
pMB_Cas9v2	gRNA sequence + *Bbs*I overhangs	Synthetic Oligos	pBR322	8631	24
pSC_Crispr Donor _NC00069.6	*Hist2h3c1*, *Hist2h2aa1, sfGFP*	pSC_Hist2h3c1 _NC00069.6, pSC_sfGFP	pSC-B-amp/kan	4300	4827
pSC_Crispr Mutant Donor	*Hist2h3c1*, *Hist2h2aa1, sfGFP*	pSC_Crispr Donor _NC00069.6	pSC_Crispr Donor _NC00069.6	4827	4827
pSC_Hist2h3c1 _NC00069.6	*Hist2h3c1*, *Hist2h2aa1*	Mouse Genomic DNA	pSC-B-amp/kan	4300	4062

2.1.9 Antibodies

Table 9: List of primary antibodies

Antibody	Company	Host species	Catalog no.	Dilution
BRN3	Santa Cruz	Goat	sc-6026	1:100
CALBINDIN	Swant	Rabbit	CB38a	1:500
CLEAVED CASPASE 3	Cell signaling	Rabbit	9661S	1:100
CONNEXIN 50	ThermoFisher Scientific	Rabbit	PA5-11644	1:50
CRYSTALLIN αA	Personal gift from Dr. Cvekl, Albert Einstein College of Medicine	Rabbit		1:500
EFNA5	Invitrogen	Rabbit	38-0400	1:100

EPHB2	Novus Biologicals	Goat	AF467	1:100
FOXE3 (M-57)	Santa Cruz	Rabbit	sc-134536	1:100
GFP	Santa Cruz	Mouse	sc-9996	1:500
GLIAL FIBRILLARY ACIDIC PROTEIN	Sigma	Rabbit	G9269	1:100
H3-S10P	Millipore	Rabbit	06-570	1:100
H3K122ME1	Abcam	Rabbir		1:100
KI67	Abcam	Rabbit	ab15580	1:100
OTX2	Abcam	Rabbit	ab15580	1:200
PITX3(N-20)X	Santa Cruz	Goat	sc-19307X	1:1000
PROTEIN KINASE Cα	Abcam	ab11723		1:200
PROX1	Millipore	Rabbit	AB5475	1:1000
TCFAP2A (3B5)	Santa Cruz	Mouse	sc-12726	1:500
TUBE1	Sigma-Aldrich	Mouse	T1323	1:200

Table 10: List of secondary antibodies

Antibody Name	**Company**	**Reactivity**	**Catalog #**	**Dilution used**
Alexa Fluor® 488	Invitrogen	Rabbit	A-21206	1:250
Alexa Fluor® 488	Invitrogen	Rat	A-21208	1:250
CY3	Jackson immuno	Goat	705-165-147	1:250
Cy3	Jackson immuno	Rat	712-165-153	1:250
Cy3	Jackson immuno	Mouse	715-165-150	1:250
DAPI	Sigma-Aldrich	---------	D9564	1:10,000
HRP-conjugated	Dianova	Mouse	115-035-003	1:500

2.2 Methods

2.2.1 Animals and tissue preparation

All animals used in this study (C57BL6/N, C3HeB/FeJ (C3H) and *Aey69* on C3H background) were kept in the mouse facility of Helmholtz Zentrum Munich. They were treated and bred according to the German Law for Animal Protection. For immunohistochemistry, the tissues were fixed in 4% PFA overnight and stored subsequently in 70% ethanol until embedding. For the QPCR, the tissues were stored immediately at -80^{o}C (to be used for RNA extraction).

2.2.2 Total RNA extraction, cDNA synthesis and realtime-qPCR

RNA was extracted using RNeasy mini kit (Section 2.1) following the manufacturer's protocol. DNA was eliminated by using gDNA Eliminator columns provided with the kit.RNA yield and purity were measured using NanoDrop ND-1000 (section 2.1).

cDNA was synthesized using Omniscript RT Kit (for OligodT) and Biozym cDNA Synthesis Kit (for random hexamers) following essentially manufacturer's instructions. OligodT primers were used for gene expression analysis of selected genes from transcriptomic data and random hexamers were used for gene expression analysis of histone genes and non-coding RNA. 1 µg of the total RNA was used and one tenth dilution of the prepared cDNA was used in PCR reactions.

DNA and RNA reference sequences were retrieved from NCBI database (Section 2.1) and primers were designed using PRIMER BLAST (Ye et al. 2012). For RT-qPCR, cautions were taken to include the intron-exon boundaries to enhance the specificity. Best primers based on their characteristics like specificity, complementarities, and secondary structures were selected using OligoAnalyzer online Tool (Owczarzy et al. 2008) and synthesized by Sigma (section 2.1).

Realtime qPCR was performed using the SensiFAST SYBR Hi-ROX Kit (section 2.1). Following the initial denaturation and enzyme activation at 95^{o}C for 5 minutes, the reaction was cycled for 45 times with denaturation at 95^{o}C for 15 seconds and annealing-extension temperature was 59^{o}C for 5 seconds and 72^{o}C for 30 seconds, respectively. Data were collected at the extension phase and processed using the StepOne software (section 2.1). Relative gene expression was calculated following the $2^{-\Delta\Delta CT}$ method (Livak and Schmittgen 2001). *B2m* was used as a reference gene for OligodT synthesized cDNA (Veazey and Golding 2011) and *Rplp0* was used as a reference gene for random hexamer synthesized cDNA (Fritsch et al. 2010). The primers used are given in Table 6.

2.2.3 Immunohistochemistry

Tissue sections in paraffin were deparaffinized in Roti-Histol (Section 2.1) followed by rehydration in descending ethanol series (2x100%, 96%, 80%, 60%, and 30%) for 4 minutes each. Finally, the sections were washed three times in water for 5 minutes each. For antigen retrieval in paraffin sections, sections were boiled for 25 minutes in 0.01 M sodium citrate buffer (pH 6.4) in a microwave oven at 600 watts and then allowed to cool for 30 minutes. Slides were then washed with Phosphate Buffered Saline (PBS) (3X) for 5 minutes and treated for 1 hour with 1% bovine serum albumin in PBS containing 0.3% Triton X-100, 0.05% Tween-20 (for blocking). Subsequently, the slides were incubated with the primary antibody/ies at 4^{o}C for overnight. The consequent day the slides were washed in PBS (4X) for 10 minutes and incubated with the appropriate secondary antibody/ies for 90 minutes. The slides were washed with PBS (3X) for 5 minutes and counterstained with DAPI for 15 minutes. The slides were then washed with PBS (2X) for 10 minutes, followed by brief wash in water and then air dried. The slides were finally mounted using Aqua-Poly/Mount (Section 2.1) and photographed using Olympus confocal microscope (Section 2.1) microscope. Images (single plane images and Z-stacks) were obtained and analyzed by ImageJ software. The findings were validated in biological replicates (minimum 2) in a blinded manner. Analysis was not done on areas shown as non-specific stained regions by corresponding negative control images, particularly blood vessels posterior to the lens and disturbed mesodermal cells beneath the RPE and above the cornea. Commercially available and validated antibodies were used and their respective dilution and product information are given in tables 7 & 8.

Cell count

The cell-cycle specific phosphorylation of histone H3 at Serine 10 position has been characterized in an extensive manner since the earliest report from Hendzel et al. 1997. In particular, in the report from Rothbart et al. 2015 on assessing the specificity of different histone PTM antibodies, the spatial location of the H3S10P antibody (Section 2.1) in different phases of cell cycle has been given in a detailed manner. In brief, microscopic examination of H3S10P cells in combination with the use of the DNA marker DAPI helps to distinguish among stages of the cell cycle: in prophase H3S10P staining are spread throughout the cell body and in interphase H3S10P is found as dotted like stained structures (Hendzel et al. 1997). The images related to the distribution of H3S10P have also been documented in embryo (Hari et al. 2012; You et al. 2015) as well as in ocular tissues (Barton and Levine 2008; Crosio et al. 2000; Ribas et al. 2012). Aberrant profiles among H3S10P cells have also been documented in conjunction with apoptosis and mitotic arrest (Chrysanthou et al. 2018; Wang et al. 2017). The analysis of H3S10P images was thus based on the published images in the above

mentioned reports. Confocal images of H3S10P stained cells were obtained with Olympus confocal microscope. The z-stacks were acquired using a frame size of 800 × 800 at 1 µm z-steps covering 5µm section area with sequential multitrack scanning using the 408 and 488 nm wavelengths of the lasers. Composite images were produced from the z stack images using ImageJ. The acquisition parameters were kept the same for all scans. Owing to the asynchronous cell cycle amongst the embryos and the different morphology between wild-type and mutant ocular sections, analysis was restricted to single sections from 3 different embryos wherein lens and retinal structures were present in both wild-type and homozygous mutant. Through this, I hoped to look at the nature of the cells occupying the mutant lens and retina in an asynchronous embryonic cell population. Counts were made in sections from 3 biological samples from each embryonic stages (Acharya et al. 2018). Cell count of each cell type (Prophase, Interphase and dysregulated) in one section was calculated as a percentage among phospho-histone-H3 positive cells in that particular section. Regions were drawn around nuclei, as delineated by DAPI and H3S10P staining, and marked as regions of interest. Mean gray value (representing the fluorescence intensity levels) and area of these regions of H3S10P was calculated using ImageJ. Statistical analyses were done using unpaired two-tailed t-test (Microsoft Excel version 15.23) to compare mean values between wild type and mutant for each embryonic stage.

2.2.4 Preparation of CRISPR tool kit- guideRNA (gRNA) and donor plasmid

Designing of guideRNAs

The gRNAs were designed using the online sgRNA Designer (http://www.broadinstitute.org/rnai/public/analysis-tools/sgrna-design). This tool ranks and picks candidate sgRNA sequences for the targets provided while attempting to maximize on-target reactivity and minimizing off-target activity. Any homology to other histone genes was also verified by BLAST.

SNP analysis

Genomic DNA from C57BL6/N mouse strain was used for the SNP analysis. The primer sets with their respective PCR conditions and the corresponding regions amplified are given in Table 1. The required PCR bands were cut out from the gel and purified according to the instruction of Nucleospin Gel and PCR clean up kit (Section 2.1). The purified DNA was then

sent for Sanger sequencing (GATC Biotech, Konstanz, Germany). The experiment was repeated independently in 2 biological replicates.

In addition, the entire region that was analyzed was cloned into StrataClone Blunt PCR Cloning Vector pSC-B-amp/ kan according to manufacturer instruction (Section 2.1). The primers used and the PCR conditions for the insert are given in Table 2. The positive single colonies were selected based on ampicillin resistance. Plasmid DNA was prepared using the Nucleospin Plasmid kit by following the manufacturer instruction (Section 2.1). The clones were verified by sequencing using the sequencing primers as well as the overlapping primer sets. The clone containing the mouse genomic sequence (pSC_Hist2h3c1_NC00069.6) was used for the construction of the donor plasmid.

Cloning of guideRNA

Oligos corresponding to the gRNA sequence as well as its reverse complement were ordered from Sigma. The sequences are given in Table 2. For cloning purposes, *Bbs*I digest overhangs were added to the ordered oligos (Highlighted in bold). The dried oligos were initially reconstituted separately at 1 µg/µl TE. Then 1 µl of each of the oligos were added into 100 µl TE buffer (10ng/µl). The mixed oligos were dimerized by heating at 100°C for 5 min and then cooled slowly to RT (Room Temperature).

The vector was cut using the restriction enzyme *Bbs*I (Section 2.1) in a 100 µl reaction digest at 37ºC, 1.5h. The restricted plasmid was then run on a 0.9% agarose gel and the 3300 bp vector band was purified using the Nucleospin Gel and PCR clean up kit. 50 ng of the plasmid DNA was then used for ligation with the 4 µl annealed oligos. The ligation reaction was done at 16ºC Overnight (O/N), or 3-4 hrs at RT

2 µl of the ligated reaction was used for transformation in DH5-α chemically competent cells. The positive single colonies were selected based on ampicillin resistance. Plasmid DNA was prepared using the Nucleospin Plasmid kit (Section 2.1). The clones were verified by sequencing using the internal T7 primer for successful gRNA sequence incorporation (pMB_Cas9v2).

Donor plasmid construction

The efficient homologous recombination-mediated knock in of *Hist2h3c1* gene fused in frame to GFP was mediated by donor plasmid. The sequence corresponding to the superfolder form of GFP was ordered from OilgoIDT (Section 2.1) as a Gblock (Cobb et al. 2015). The relevant

genomic fragments were amplified using primers (Table 3) from the plasmid pSC_Hist2h3c1_NC00069.6. KOD hot start polymerase (Section 2.1) was used for the construction of the donor plasmid using the fusion PCR method (Szewczyk et al. 2006). PCR cleanup was done on the purified gel bands of appropriate size. 0.5 µl of the cleaned up PCR products were used as the template for fusion PCR using respective forward and reverse primers that fuses the fragments into a single molecule. For example, the forward primer of Gene was used in combination with the reverse primer of GFP to create the fused product of Gene & GFP (Refer Fig 2.1). Fusion PCR conditions were:

Initial denaturation at 94°C for 5 min
94°C for 45 s, 65°C for 30 s, 72°C for 3 min (5 cycles)
94°C for 45 s, 64.5°C for 30 s with 0.5°C decrement per cycle (20 cycles)
Extension at 72°C for 3 min
Hold at 4°C

The fused product was purified from agarose gel using and transformed into the pSC-A-amp/kan *plasmid* provided with the StrataClone Blunt PCR Cloning Kit (Section 2.1) according to the manufacturer instructions. The following day colonies were chosen for plasmid DNA preparation. Plasmids containing the desired PCR product insert (pSC_Crispr Donor _NC00069.6) were verified by sequencing.

Mutant Donor plasmid construction

A plasmid with the desired point mutation (A>C) site-directed mutagenesis (SDM) was done on the plasmid pSC_Crispr Donor _NC00069.6. SDM was done with the required complementary primer pairs containing the mutated base (Table 4) using KOD hot start polymerase (Section 2.1). The parent template was removed using a methylation-dependent endonuclease (i.e. *Dpn*I) for 30-60 min at 37 ºC

2-5 µl of the PCR reaction after *Dpn*I was directlyused for transformation in DH5-α chemically competent cells. The positive single colonies were selected based on ampicillin resistance. Plasmid DNA was prepared using the Nucleospin Plasmid kit. The clone were verified by sequencing (pSC_Crispr Mutant Donor) using the internal sequencing primers as well as the primers around the mutation site (Table 4).

Fig.2.1

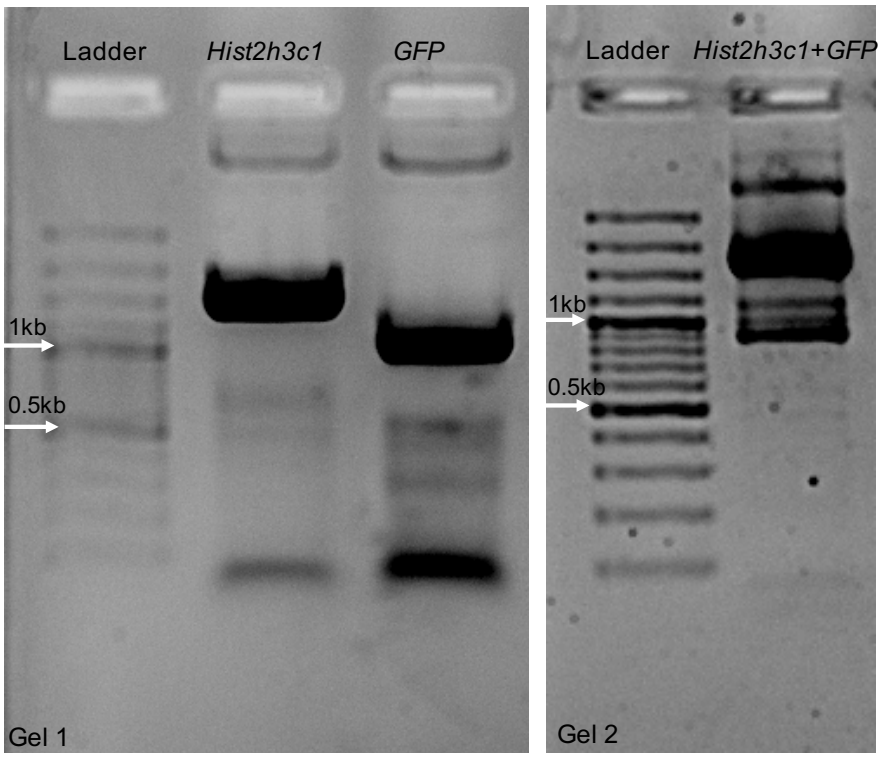

Fig.2.1: Representative results of Fusion PCR.
Lanes *Hist2h3c1* and *GFP* in Gel 1 refer to the amplification of the respective genes from their plasmids. Lane *Hist2h3c1+GFP* in Gel 2 refers to the fused product of the genes obtained from the fusion PCR of the purified sample from Gel-1. 100bp DNA ladder was used as a marker.

2.2.5 *In-vitro* analysis:

N2A cell line has routinely been employed in Crispr guide testing was used for *invitro* analysis (Liang et al. 2015). The gRNA sequence containing plasmids and donor plasmids were transfected in N2A cell line and assayed for their ability to mediate targeted cleavage.

24 hours prior to transfection, the cells were seeded in a 48-well plate at a cell density of 5×10^4 cells per well. For plasmid DNA transfection, 0.1 µg DNA was added to 27 µl of Opti-MEM I, followed by addition of 0.90 µl of X-tremeGENE HP transfection reagent. The mixture was incubated at room temperature for 20 min and then added to the cells.
The transfected complexes include:

Negative control 1: Empty vector devoid of any guide RNA sequences.
Test Sample 1: Vector with guide RNA sequences & plasmid pSC_Crispr Donor _NC00069.6.
Test Sample 2: Vector with guide RNA sequences & plasmid pSC_Crispr Donor _NC00069.6.

The plate was incubated at 37 °C for 48 h in a 5% CO_2 incubator. After 48 hours the cells were imaged for any GFP positive cells.

2.2.6 Establishment & characterization of transgenic mouse line:

Generation of mice via microinjection of the one-cell embryo (in co-operation with Transgenic Unit, Institute of Developmental Genetics, Helmholtz Centre Munich)

100 µM of the respective synthetic 5' and 3' gRNAs was mixed with 100 µM of Alt-R™ CRISPR-Cas9 tracrRNA (Section 2.1). The complex was incubated for 5 minutes at 95°C and cooled down to room temperature to form a crRNA/tracrRNA duplex. Prior to pronuclear injection, the complex was diluted in microinjection buffer together with recombinant Cas9 protein (Section 2.1) to a working concentration of each of 11 ng/µl (crRNA), 22 ng/µl (tracrRNA) and 50 ng/µl (Cas9). The injection mix is incubated for 10 min at room temperature and 10 minutes at 37°C to form the active ribonucleoprotein (RNP) complex. The targeting donor plasmid was dissolved in water and diluted with injection buffer to a working concentration of 10-20 ng/µl. One-cell embryos were obtained by the mating of C57BL6/N males with C57BL6/N females. For microinjections, one-cell embryos were injected into the larger pronucleus. Following injection, zygotes were transferred into pseudo-pregnant CD1 female mice to obtain live pups. Handling of the animals was performed in accordance with institutional guidelines and approved by the government of Upper Bavaria. Genomic DNA was isolated from tail tips of mice and PCR amplification was done for the genotyping.

Genotyping

Adult tail clips (from F0 generation), adult ear clips (from F1 and later generations), embryonic body tissues were used to extract the genomic DNA. Tissue samples with 500 µl of lysis buffer (Section 2.1) containing 20 µg of proteinase K and 0.5% SDS were incubated overnight at 55^{o}C with shaking. Following lysis, proteins were precipitated using 2.5M NaCl with vigorous shaking and incubating on ice for minimum 30 minutes. Samples were centrifuged at 6000 rpm (Eppendorf 5415R) for 10 minutes and supernatants were transferred into new tubes. DNA was precipitated with 1 ml ethanol and pelleted by centrifugation at 13000 rpm for 25 minutes. Pellets were washed with 250 µl 70% ethanol, dried and resuspended in 25 µl to 75 µl MilliQ water, depending on the tissue sample. DNA samples were stored at 4^{o}C till use. Mice generated from the injection of guides with wild-type donor plasmid are referred to as Hist2h3c1_wt-GFP_CRKI (CRKI being the acronym for constitutive expression). Similarly,

mice generated from the injection of guides with mutant donor plasmid are referred to as Hist2h3c1_Ile120Leu-GFP_CRKI.

For genotyping of Hist2h3c1_wt-GFP_CRKI and Hist2h3c1_Ile120Leu-GFP_CRKI founder and F1 mice, primers spanning the entire homology arms at the 5' side to the GFP region were used (Table 5 and Fig 2.2). The PCR product was then resolved on 2.5 % agarose gel along with 100 bp ladder as size marker (section 2.1). The band of interest was excised and purified using the Nucleospin Gel and PCR clean up kit (section 2.1). The DNA was sent for Sanger sequencing (GATC Biotech, Konstanz, Germany). Genotypes were assigned on the basis of appropriate band size and sequence. For the mice of the subsequent generations primers spanning the *Hist2h3c1* gene region to the GFP were used (Table 5 and Fig 2.3). For genomic site integration analyses the respective primers at the 5' and 3' end, PAM mutation site primers are given in Table 5.

Fig.2.2

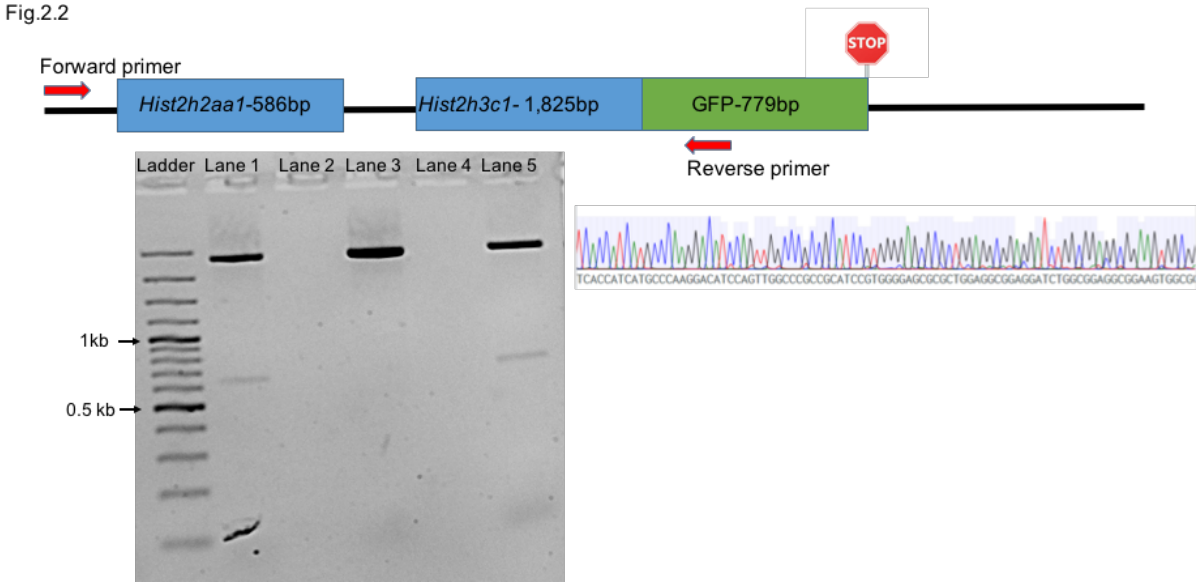

Fig2.2: Representative methodology and results of genotyping PCR used in genomic DNA from founder mice.
The positions of the primers in the transgene used are illustrated. The regions containing the genes *Hist2h2aa1*, *Hist2h3c1* and 5' part of GFP are covered in the PCR. PCR product using the primers are given in the gel below. 100bp DNA ladder was used as marker. Positive samples can be identified by the presence of the positive PCR band (2.7kb). Lane 2 and 4 refers to the negative samples. Lane 1,3 and 5 refers to test samples. Sanger sequencing from these products using the reverse primer gives rise to the chromatogram containing the GFP sequence (shown at the side).

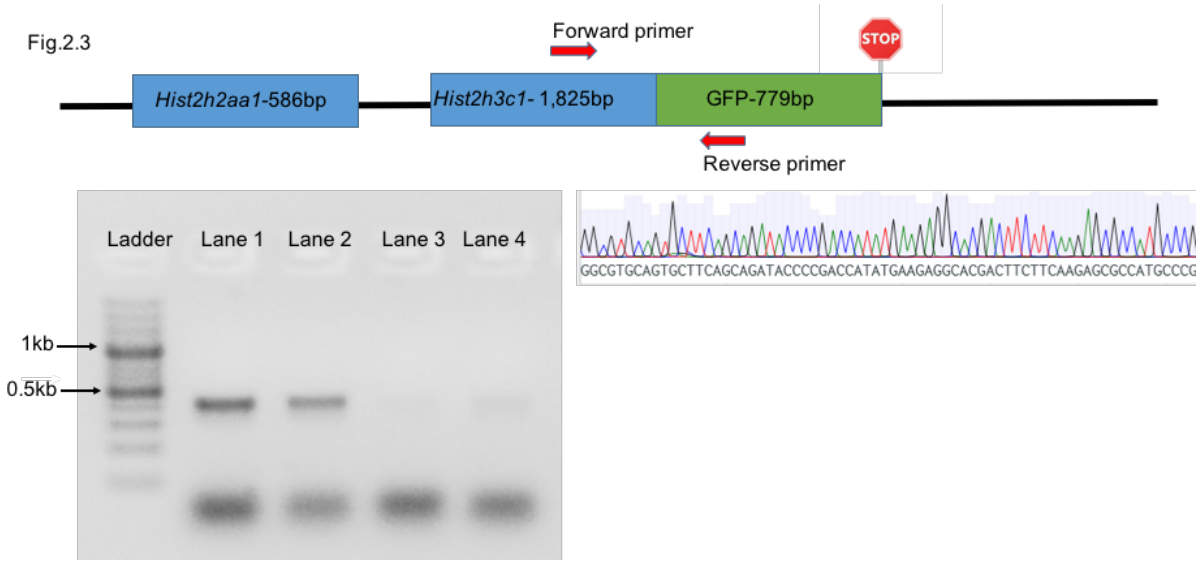

Fig.2.3: Representative methodology and results of genotyping PCR used in genomic DNA from breeding of founder mice.
The positions of the primers in the transgene used are illustrated. The regions containing the 3' part of *Hist2h3c1* and 5' part of GFP are covered in the PCR. PCR product using the primers are given in the gel below. 100bp DNA ladder was used as marker. Positive samples can be identified by the presence of the positive PCR band (0.44 kb). Lane 3 and 4 refers to the negative samples. Lane 1 and 2 refers to test samples. Sanger sequencing from these products using the reverse primer gives rise to the chromatogram containing the GFP sequence (shown at the side).

Protein Extraction and Western Blot

For protein isolation, whole embryos of the respective wild type and mutant were prepared at respective stages. Protein extracts were subsequently prepared from the embryos by homogenization in RIPA buffer supplemented with 1X protease and phosphatase inhibitors. The homogenized mixture was allowed to incubate for 20-30 min on ice. The cell debris was removed by centrifugation at 12,000 rpm for 10 mins at 4 °C. The supernatant containing the proteins was transferred to a fresh tube and stored at -20 °C until further analysis. For Western Blot, 30 µg of isolated protein was added to an equal volume of SDS gel loading buffer and heated for 10 min at 100 °C. The respective protein extracts were separated using 15% SDS–polyacrylamide gel electrophoresis gels and transferred electrophoretically onto a nitrocellulose membrane. At the following day, the membranes were washed in PBS with 0.1% Tween-20. Membranes were then blocked for 2 h with PBS containing 5% dried milk powder and incubated overnight with mouse anti-GFP (1:500). The following day, after washing in PBS containing 0.1% Tween-20, the membrane was incubated in appropriate mouse anti-rabbit (1:500) Horse Radish Peroxidase (HRP) - conjugated secondary antibody (diluted in

PBS containing 0.5% dried milk. The signals were detected with Roti-Lumin kit using a chemoluminescence-based, peroxidase-mediated detection systems.

Co-Immunoprecipitation

The protein samples were centrifuged at 4°C for 10 minutes (Eppendorf 5415R). The supernatant was transferred to 1.5 ml conical centrifuge tube on ice. The volume was made up to with RIPA buffer and 50µl was set aside as control. The lysate was precleared (optional step) by adding 1.0 µg (50µl) of the appropriate mouse control IgG together with 20 µl of resuspended volume of Protein A/G PLUS-Agarose. The samples were then incubated at 4° C for 4hr. The beads were allowed to settle by gravity and the supernatant was transferred to a fresh 1.5 ml tube on ice. 1-2 µg of the GFP primary antibody was added and incubated for 2 hours at 4° C. Then 20 µl of Protein A/G PLUS-Agarose was added and incubated at 4° C on a rocker platform overnight. The following day the immunoprecipitates were collected and washed gently. The proteins were eluted by SDS gel loading buffer to the beads flowed by heating for 10 min at 100°C. Samples were then size-separated by electrophoresis in SDS-containing (15%) polyacrylamide gels and transferred to nitrocellulose membranes. Western blot was then done using GFP antibody.

Embryonic fibroblasts culture:

At respective day (E10.5), uteri were removed and embryos were recovered in DMEM + 50% FBS. The head was removed and homogenized by vigorous pipetting. The homogenized tissue was then washed briefly in PBS, followed by plating in DMEM + 50% FBS. The cells were imaged after 48 hours (EVOS™ FL Imaging System).

2.2.7 ChIP-Seq and ChIP-QPCR for *Hist2h3c1* encoded H3.2

Chromatin Immuno Precipitation assays (ChIP) would help in identifying the incorporation sites of *Hist2h3c1* through the GFP tag in transgene positive mouse embryonic tissues (Zhang et al. 2017). Identification of H3.2 - specific incorporation sites at this stage would help in shortlisting the potential molecules triggering the microphthalmia in *Aey69* (persistent connection of the surface ectoderm with the developing lens from E11.5). The embryonic stage of E10.5 was chosen as the stage for ChIP library preparation and sequencing (Zymo Research, Irvine, US).

ChIP-Seq on frozen embryonic head tissues

To get the embryos, respective animals were bred and the embryos were collected. Head of the embryos was transferred to a 1.5 ml tube and immediately frozen at -80°C. The body was taken for genotyping: Upon confirmation of the sequence for *Hist2h3c1-GFP* in the genotyped PCR samples, the positive samples were chosen and sent to the Zymo Research, Irvine, US in dry ice. Sample preparation, ChIP DNA extraction, library generation and sequencing was done by the company. Analysis and peak calling by MACS software (Model-based Analysis of ChIP-Seq) was also done by the company. The ChIP Seq data was visualized and analyzed using UCSC Genome browser by uploading the sequencing files (bigWig – type of sequencing file) as a custom track (option for sequence files uploading in the browser). The generated track files were analyzed in comparison to their respective input control for possible fold enrichment UCSC Genome browser (Feng et al. 2012; Raney et al. 2014). Heat maps comparing the average ChIP-Seq was generated using EaSeq (Lerdrup et al.2016).

ChIP-QPCR

Homogenization and crosslinking of tissues:
Four frozen embryonic heads were pooled and 250µl of ice cold PBS was added. By gentle pipetting using 1ml pipette the tissues were homogenized to small bits. Further homogenization was done using squisher (4-5X) in ice. 750µl of PBS was added to the tissues and the tissues were crosslinked by adding formaldehyde (16 % PFA) to a final concentration of 1% (v/v). The fixation was allowed to proceed for for 10 min at room temperature with gentle shaking or rotating. The cross-linking reaction was stopped by adding 2.5M glycine to a final concentration of 0.125M and continued shaking or rotating for 5 min.

Nuclei preparation from tissues and chromatin shearing:

The cross-linked tissue was centrifuged at 8000 rpm (Eppendorf 5415R) for 90 seconds at 4°C. The supernatant was discarded and the sample was resuspended in PBS containing 1X protease inhibitors. The resuspended sample was centrifuged again at 8000 rpm for 90 seconds at 4°C. The step was repeated twice and the pellet was resuspended in the kit provided nuclei prep buffer (ZymoSpin ChIP kit) and the samples were then processed to chromatin shearing buffer according to manufacturer's instructions. The samples were sonicated at 80% amplitude for 40 cycles (30 s ON, 30 s OFF).

Assessment of chromatin shearing and reverse crosslinked DNA purification*:*

After shearing 25 µl of each sample was taken, reverse crosslinked by adding 2 µl of Proteinase K (10 mg/ml), 1 µl of RNaseA (10mg/ml) and 1 µl of 5M NaCl. The reverse crosslinked DNA was allowed to incubate for 30 minutes at 37°C and later at 65°C for 4 hours to overnight. The DNA was then purified by using the Nucleospin PCR clean up kit according to the manufacturer instructions. The DNA was quantified using Qubit dsDNA HS Assay Kit kit and 1-2 ng of the DNA was then checked for fragment size distribution using capillary electrophoresis instrument (2100 Bioanalyzer) according to manufacturer instructions. If the chromatin shearing was observed to be not satisfactory, reshearing was done for 10-5 cycles (depending on the observed fragment size).

Immunoprecipitation of chromatin:

After the confirmation of optimal fragment size (200-600 bp) 2-3 µg of GFP antibody was added to 5-10 µg of sheared chromatin. The volume was made up to 1ml using ZymoSpin ChIP kit provided Chromatin Dilution Buffer supplemented with protease and phosphatase inhibitors. 10% of the pooled sample was kept aside as input control and stored at 4°C. Enrichment and elution were done using the ZymoSpin ChIP kit and according to the manufacturer instructions. Reverse crosslinking of the enriched DNA was done according to the protocol mentioned before. The purified DNA was stored at -80 °C until QPCR analysis.

2.2.8 *In-silico* analysis for miRNA

The mutation of interest lies in the coding region of the *Hist2h3c1* gene. The mutation might effect its pathology through altered mRNA-miRNA binding or through protein structural changes. For the same, *in-silico* analyses followed by technical experiments was carried out to test the hypotheses.

miRDB and RegScan were used for input of mutant *Hist2h3c1* mRNA sequence. miRDB target prediction program is based on systematical analysis of public high-throughput experimental data while miRNA prediction in RegRNA relies heavily on the free energy of each miRNA:mRNA target pair (Kuhn et al. 2008; Peterson et al. 2014).

2.2.9 Co-expression analysis

The shortlisted candidate miRNAs were then taken up for further analysis by stem loop QPCR to quantify their co-expression with the mutated gene (Chen et al. 2005; Kramer 2011).

Embryonic stages of E10.5, E11.5 and E12.5 were chosen for analysis. The wild-type and mutant samples were analyzed in 3 biological duplicates. The expression of all the target miRNAs quantified in relation to the housekeeping gene of *Sno-202*. *Hist2h3c1* was quantified in relation to the housekeeping gene of *Rplp0*. The primers used are given in Table 6.

2.2.10 *In-silico* analysis for protein structure

The full-length amino acid sequence for Histone H3.2 was used. Three-dimensional models of the histone protein containing wild type and mutant sequence were generated and analyzed with I-TASSER and Quark (Yang et al. 2015). All structures were analyzed using the PyMOL Molecular Graphics System (version 0_99rc6, 2010). Changes in the structure of the histone protein were estimated by the alignment of the wild type and mutant structure and RMSD (Root Mean Square Deviation) calculation. Low RMSD values represent similar structures.

To investigate the binding of the proteins to histone H4 protein the principal docking servers: PatchDock and GRAMMX, were used to obtain a set of possible complexes (Autiero, Costantini, and Colonna 2009). The flexibility of the residues with respect to the nucleosomal complex was also computed using a Gaussian network model (Li et al. 2016).

The *in-silico* results were tried to be validated by X-ray crystallography analysis of the nucleosome containing mutant histone protein (Ile120Leu). This was done in collaboration with Dr. Geerlof (Protein Expression and Purification Facility, Helmholtz Centre Munich) and Dr. Janowski (Structural Biology Unit, Helmholtz Centre Munich).

2.2.11 Recombinant histone protein production and nucleosome assembly

Histone Expression Plasmids

Expression plasmids for the individual histone proteins – H2A, H2B, and H4 based on the T7 expression system in pET-21a(+) vector were a kind gift from Dr.Schneider, Institute of Functional Epigenetics, Helmholtz Centre Munich. The H2A-pET-21a(+) vector was used for cloning in the required wild-type and mutant H3.2 sequences. *Nde*I and *Bam*HI sites were used for the restriction-based cloning.

Restriction based cloning for H3.2 expression plasmids:

The H2A-pET-21a(+) vector was cut using the restriction enzyme *Nde*I and *Bam*HI in a 50 µl reaction digest at 37ºC, 1.5h. The restricted plasmid was then run on a 1% gel and the 5800bp

vector band was purified using the Nucleospin Gel and PCR clean up kit. 50 ng of the plasmid DNA was then used for ligation with the restricted PCR product.

Forward and reverse primers with the *Nde*I and *Bam*HI overhangs respectively were ordered (Table 7). The primers were used for the amplification of the wild-type and mutant H3.2 sequences, previously cloned in pSC_Crispr Donor _NC00069.6 and pSC_Crispr Mutant Donor respectively. The individual PCR product was run on a 1% gel and the 5800 bp vector band was purified using the Nucleospin Gel and PCR clean up kit. The purified PCR products were then cut using the restriction enzyme *Nde*I and *Bam*HI in a 50 µl reaction digest at 37ºC, 1.5h. The restricted PCR products were purified using the Nucleospin PCR clean up kit and ligated into the restricted H2A-pET-21a(+) vector by incubating for 3-4 hrs at RT.

2 µl of the ligated reaction was used for transformation in DH5α chemically competent cells. The positive single colonies were selected based on ampicillin resistance. Plasmid DNA was prepared using the Nucleospin Plasmid kit. The clones were verified by sequencing using the internal T7 primer for successful H3.2 sequence (wild-type and mutant) incorporation.

Bacterial transformation:

Rosetta(DE3)pLysS cells (from Dr. Geerlof), supplying the required tRNAs for recombinant mammalian protein expression (Rosano and Ceccarelli 2014), were transformed with 200 ng of the pET histone expression plasmids and plated on LB agar plates with ampicillin (100 µg/ml) and chloramphenicol (25 µg/ml). The plates were incubated at 37°C overnight. The next day one colony from the culture plate was used for inoculating pre-culture tube containing 4 ml of 2 LB media (with ampicillin and chloramphenicol). The tubes were incubated in a shaker at 37°C overnight.

Induction:

The next day, the pre-culture tubes were inoculated in 1l of LB media. The cultures were grown into log phase at 37°C with rotation until OD_{600} = 0.6. Histone expression was then induced by adding 0.4 mM IPTG (final concentration). Induction was done for 3 hours. Pre-and post-induction culture aliquots were taken for analyzing induction efficiency through SDS gel run.

Inclusion Body Preparation:

After 3 hours of IPTG induction the cultures were pelleted down by centrifugation at 4000 rpm for 25’ at RT. The pellet was resuspended in 16.7ml of wash buffer and frozen immediately at

-80°C overnight. The cell suspension was lysed by thawing at 37°C in a water bath. The volume was adjusted to 25ml per liter pellet with fresh wash buffer. The cell suspension was sonicated on ice for 4 times with 30 pulses at 100% intensity (or until the viscosity is reduced). The suspension was then centrifuged at 4000 rpm (Sigma 3K18) for 10 min at 4°C to pellet inclusion bodies. The inclusion bodies were then washed twice in wash buffer with 1% TritonX-100 and twice in 20 ml of wash buffer without Triton X-100. After the last wash the pellet was resuspended in 10-20 ml unfolding buffer (depending on induction efficiency) and the histones were unfolded by rotating at RT for 1h. The solution was centrifuged for 15 min at 10000 rpm (Sigma 3K18), transferred to a new tube and centrifuged again.

Histone protein purification:

The supernatant was dialyzed at 4°C for ~2h against 2l of freshly prepared SAU 200 buffer. The second dialysis with 2l of freshly prepared SAU 200 buffer was allowed to proceed O/N. The last dialysis step was done for ~2h with the same freshly prepared buffer, the following day and the precipitated material was removed by centrifugation at 13000 rpm for 20 min (Sigma 3K18). The cleared supernatant was loaded on a 6ml ResourceS column equilibrated with SAU200 and separated using a linear gradient of 0-100% from SAU200[A] to SAU600[B]. For H4, the gradient was changed to 30-100%.

500µl fractions were collected and the peak fractions were analyzed by SDS PAGE. Fractions containing pure histones were pooled and dialyzed against 2l of autoclaved MilliQ H_2O with 2mM BME. The second dialysis was done with 2l of autoclaved MilliQ H_2O with 2mM BME and was allowed to proceed O/N. The last dialysis step was done for ~2h with 2l of autoclaved MilliQ H_2O with 2mM BME, the following day and the precipitated material was removed by centrifugation at 13000 rpm for 20 min (Sigma 3K18). The unfolded histone proteins were quantified using the OD276nm and their respective molar extinction coefficients.

Formula: OD276/molar extinction coefficients* molecular weight = µg/µl
The histone proteins were freeze dried and stored at -80°C.

Octamer Reconstitution:

The lyophilized histones were dissolved to a concentration of 1mg/ml in unfolding buffer. Unfolding was done for 1h at RT. The 4 histones were mixed in equimolar ratios and dialyzed (at 4°C) against 1l of refolding buffer for 3h (2 times) and O/N dialysis against 2l of refolding

buffer The octamer was purified by gel filtration on Superdex 200 (30ml) in Äkta purifier using filtrated autoclaved millipore H_2O and filtrated refolding buffer. During the purification, high molecular weight aggregates first, come out followed by the octamers and lastly, the H2A-H2B dimers elute. The SDS-PAGE checked octamer fractions were pooled and concentrated to a final volume of no more than 500ul using concentrators (30KDa cut off).

Nucleosome reconstitution:

The conventional DNA sequence for nucleosome assembly was produced by PCR amplification from the pGEM-3z/601 (Plasmid #26656, Addgene). However, the required concentration and amount – 2mg/ml were never reached using the lab kits and protocols. Therefore, commercial DNA synthesis production was availed (Applied DNA Sciences, Inc., USA) and the high concentrated DNA was used for assembly.

Step by step salt gradient dialysis for nucleosome assembly:

The following equimolar mixture of octamer and DNA mixture was prepared

Octamer - 500 µg
DNA - 217.34 µg
5M NaCl - 100 µl
1M DTT - 2.5 µl

Octamer was added last to the reconstitution mixture and autoclaved water was used to make up the reconstitution mixture to the required volume (500µl). The reconstitution mixture was incubated at room temperature for 30 min. The reconstitution mixture was then transferred into a 30KDa cut off dialysis bag. The reconstitution mixture was first dialyzed against TE buffer pH 8.0 containing 1 M NaCl for 2 hr at 4°C. After 2 hrs the mixture was then transferred sequentially through TE buffers containing the reduced concentration of NaCl (0.85M, 0.65M, 0.5M). Each dialysis allowed to proceed for 2 hrs. Overnight dialysis was done against TE buffer containing 0.25 M NaCl. The following day the reconstituted nucleosome was allowed to equilibrate by dialysis against two changes of freshly prepared TE buffers for 2 hours each.

The assembled nucleosome was purified by gel filtration on Superdex 200 (30ml) using filtrated autoclaved MilliQ H_2O and filtrated TE buffer. The purified nucleosome was concentrated to a final concentration of 3-4 mg/ml using concentrators (30KDa cut off). The concentration was also verified in a semi-quantitative way by running the purified nucleosome against serial dilutions of octamers of known concentration.

3. Results

Objective 1: Immunohistochemistry and transcriptomic based characterization of the *Aey69* microphthalmic phenotype.

Aey69 mouse line was introduced in 2012 to AG Graw for ocular specific characterization. Extensive histological characterization done upon its introduction revealed the lens phenotype to be evident from E11.5 and the retinal changes to occur at postnatal stages (Fig1.2). However, immunohistochemical characterization of the changes had been limited to CRYGD characterization in the lens (Richter-Kügler Master's thesis 2013). Therefore, extensive immunohistochemical analyses based on lens and retinal proteins was done from the stage of E11.5 to understand more about the *Aey69* microphthalmic phenotype.

3.1 Disappearing lens in *Aey69*.

To understand and validate, whether there is any kind of lens material in the mutant eyes, I checked by immunohistochemistry for the presence (or absence) of lens specific CRYAA (Graw 2009). The results are given in Fig. 3.1A. The lens-specific expression of CRYAA indicate clearly that there is lens material expressing these proteins in the mutant, but their expression pattern is not comparable to the wild type. In the wild-type, the localization of the CRYAA signal demonstrates the transition from a lens vesicle (E11.5) to the circular lens structure with anterior proliferating lens epithelial cells and posterior differentiating lens fibers (E12.5-E14.5). However, in the mutant the lens vesicle is not able to form its characteristic structure due to the persistent connection with the surface ectoderm (E11.5-E12.5). There seems to be an increasing loss of lens-specific proteins in the developing mutant eyes from E12.5. It can be concluded that the failed separation of the surface ectoderm does not prevent the expression of lens-specific proteins, but rather stops these lens cells from successfully differentiating into lens fiber cells.

Due to the similarity of the lens pathology with the *Pitx3* mutant mouse model aphakia (Ahmad et al. 2013; Semina et al. 2000), I also tested for the immunohistochemical distribution of PITX3 and its lens specific downstream transcriptional target FOXE3 (Blixt et al. 2000). Interestingly, PITX3 lens expression was maintained in the wild-type and mutant lens vesicle at E11.5. In the subsequent stages, PITX3 expression became limited to the future lens epithelium in the wild type, however no such restriction was found in the mutant, and PITX3 seemed to be distributed all over the lens area. Later, a decrease in PITX3 stained area was observed from E12.5-E14.5 (Fig. 3.1B). Interestingly, there was no absence of PITX3 lens

expression in the embryonic stages of the mutant. Decrease in PITX3 stained area is observed from E12.5-E14.5 (Fig. 3.1B). The decreasing pattern of PITX3 follows the trend of the crystallin expression pattern indicating a dying lens structure wherein the lens markers are gradually lost. Consistent with CRYAA and PITX3 staining observations FOXE3 was also found to be rapidly disappearing in the *Aey69* embryonic eye (Fig. 3.2A). The distribution was not uniform over the mutant lens vesicle in comparison to the wild type. Interestingly, the decrease of the FOXE3 expression was observed to be stronger and earlier (E11.5) than the decrease of the PITX3 expression in the mutant lens. Cumulatively, it can be said that the development and differentiation of the lens in the *Aey69* mutants is strongly disrupted. Comparison of lens expression of PITX3 and FOXE3 hints at disruption in FOXE3 expression to happen independent of the regulatory activities of PITX3.

The rapid degeneration of the lens between E11.5 and E13.5 with numerous pycnotic nuclei and apparent failure of fiber cell differentiation (Fig. 3.2B), led me to examine if lens vesicle cells were undergoing apoptosis. The CLEAVED CASPASE 3 staining in lens indicated the presence of apoptotic events in the mutant lens from E11.5 - E13.5, when the lens structure is shrinking (Fig. 3.2B). Throughout this process, the expression of the transcription factor AP2α is gradually decreasing in the dying lens structure. At E14.5, a lens structure is no longer present in *Aey69*, henceforth no AP2α staining is seen in the anterior part of the mutant eye. However, the expression of AP2α is now observed in both the mutant and wild-type retina.

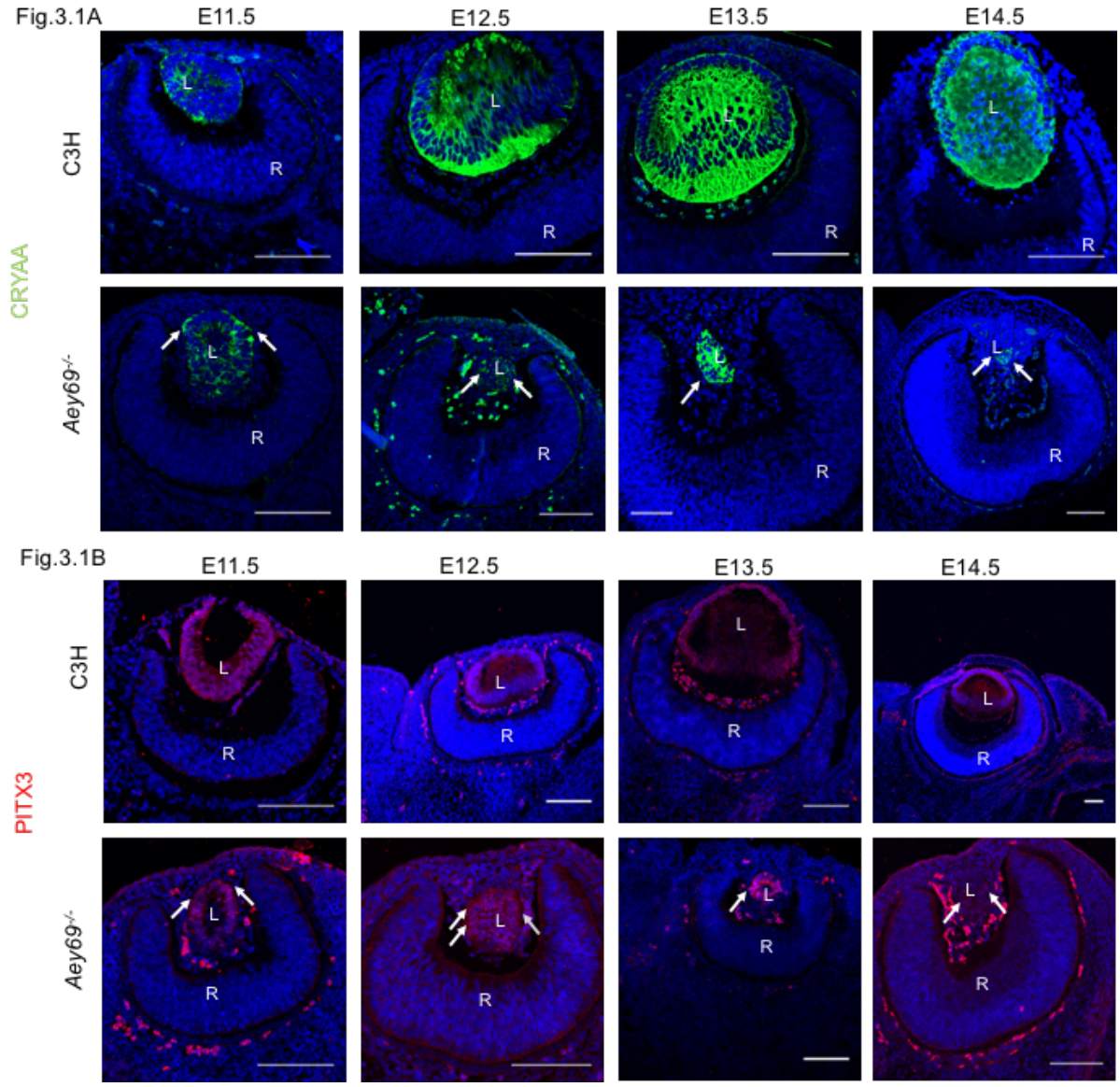

Fig.3.1: **Lens development in *Aey69* mutants.**

The lens-specific markers **CRYAA** (A) and **PITX3** (B) were used to characterize the early lens from the stages of E11.5-E14.5. At E11.5, no major change was observed in the distribution of the proteins between the wild type and mutant lens (marked by their respective arrows). However, through the stages of E12.5 – E14.5 the arrows highlight clearly the decreased CRYAA and PITX3 expression and a diminishing lens region in the mutant. The bars indicate 100 µm; n=3 for each embryonic stage; L, lens; R, retina; ON, optic nerve. Adapted from Vetrivel et al., 2019 under the terms of the Creative Commons Attribution License.

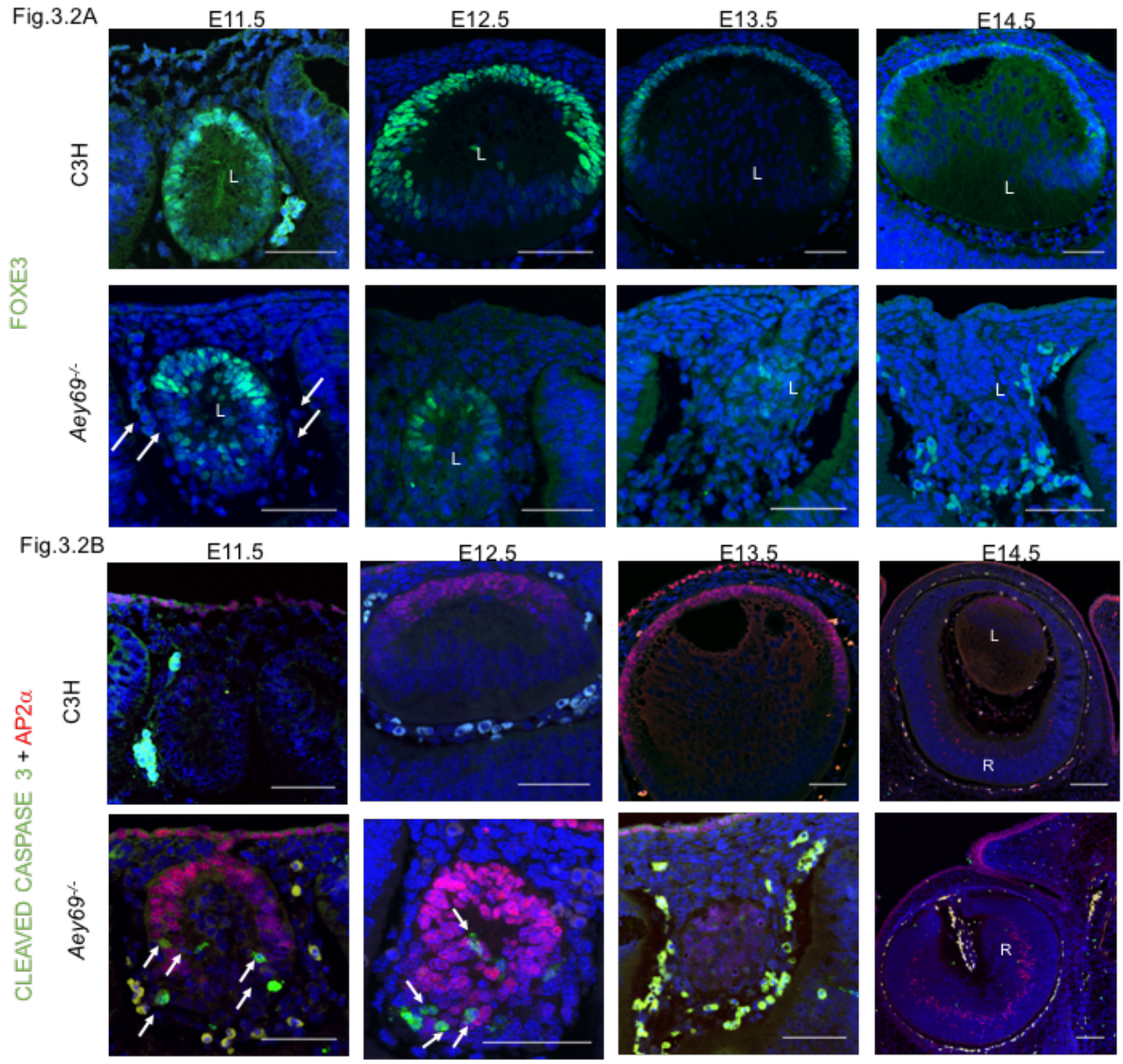

Fig. 3.2: **Disappearing lens vesicle and FOXE3 in lens and retina.**

A) The lens-specific transcription factor **FOXE3** was used to identify any disruptions in lens development starting from E11.5. The arrows marking the mutant lens at E11.5 clearly indicate reduced expression of FOXE3 at E11.5.
B) The apoptotic marker **CLEAVED CASPASE 3** was used to characterize apoptotic events during ocular development from E11.5 -E13.5, when the lens structure diminishes. The arrows marking the mutant lens at E11.5-E12.5 clearly indicate that the apoptotic death of the lens structure. There is also a consistent loss of ocular transcription factor **AP2α** in the mutant lens through E11.5-E13.5.
The bars indicate 50 µm from E11.5-E13.5 and indicate 100 µm at E14.5; n=3 for each embryonic stage; L, lens; R, retina; ON, optic nerve. Adapted from Vetrivel et al., 2019 under the terms of the Creative Commons Attribution License.

3.2 Disruptions in retinal development.

The retina comprises seven primary cell types: rod and cone photoreceptors, amacrine cells, retinal ganglion cells (RGCs), horizontal cells, bipolar cells and Müller glia. These cells are formed from a common pool of retinal progenitor cells (RPCs) during development in a characteristic, but overlapping, order (Livesey and Cepko 2001). Amongst the different cell types, BRN3-positive and OTX2-positive cells represent the earliest retinal progenitor population starting around E11.5 and E12.5 respectively (Brzezinski et al. 2010; Pan et al. 2005). Therefore, these two markers were used to characterize the early retinal development in the wild type and mutant through the stages of E11.5-E15.5. Immunostaining shows the foremost BRN3 expression in the central retina at E12.5 of the wild-type retina (Fig. 3.3A). As retinal development progresses, the expansion of BRN3-positive p
opulation is seen around the peripheral retinal regions (E13.5) and extends to the migrating retinal ganglion cells (RGC) to form the prospective ganglion cell layer (GCL) of the developing retina. However, in the mutant retina the foremost expression starts from E11.5, and comparatively more BRN3-positive cells are observed through the stages of E12.5-E13.5. This early appearance of BRN3-positive retinal progenitor cells in the mutant retina was also seen with OTX2-positive RPCs at E11.5 and E12.5 (Fig. 3.3B).

At P7 most retinal cells occupy their final positions within the retina and their distribution can be assessed without the impact of *rd1* mutation in the mice of C3H genetic background (Kalloniatis et al. 2016; Kranz et al. 2013; Young 1985). To see, whether all major retinal cell types contribute to this overgrowth in the *Aey69* mutants, the localization of the major retinal cell types was assessed using Calbindin (horizontal, amacrine and ganglion cells), Protein kinase Cα (bipolar cells), OTX2 (photoreceptors and bipolar cells), GFAP (Müller cells) and BRN3 (RGC). localization of the retinal cell types was assessed using Calbindin (horizontal, amacrine and ganglion cells), Protein kinase Cα (bipolar cells), OTX2 (photoreceptors and bipolar cells), GFAP (Müller cells) and BRN3 (RGC). The main conclusion from this analysis is that all major retina layers are present in both mutant and wild-type mice, but the retinal architecture is lost in the mutants and the whole retina appears as a collapsed structure filling up the ‘empty’ area of the lens (Fig. 3.3C).

Thus, the immunohistochemical characterization of the ocular pathology in *Aey69* clearly indicated that the lens structure is essential for the placement of the stratified retina (P7;

Fig.3.3C). It also illustrated a time course of disruptions in lens and retinal development: apoptotic events in lens (E11.5-E13.5; Fig.3.2B) and earlier expression of RPCs (E11.5; Fig.3.3A). These vital points were also analyzed in the related microphthalmia mouse model of *aphakia* (*Pitx3* homozygous knockouts; Ahmad N et al. 2013). The microphthalmic pathology in *Aey69* show a dominant mode of inheritance. Therefore, to examine whether the immunohistochemical alterations found in homozygous *Aey69* mutants are also found in heterozygous *Aey69* mutants, the alteration was analyzed in heterozygous *Aey69* mutants. Images in Fig.3.4 indicate that the pathological features of earlier expression of BRN3 positive RPCs and apoptosis of the lens is observed at E11.5 in the *aphakia* and heterozygous *Aey69* mutants. And also all the retinal layers are present in *aphakia* and heterozygous *Aey69* mutants (Fig.3.5).

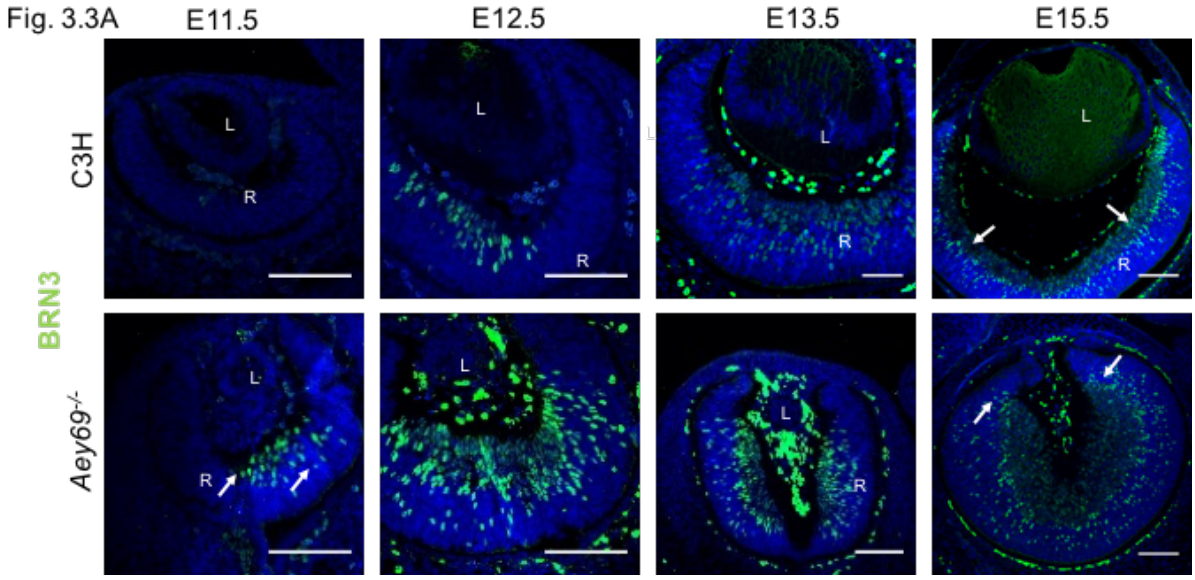

Fig. 3.3: **Retinal development in *Aey69* mutants.**
A) The ganglion cell specific marker BRN3 was used to characterize the early retina developmental changes and associated hyperproliferative events. The arrows in the mutant retina at E11.5 clearly indicate an early overexpression of BRN3-positive retinal cells. This overexpression does not affect the expansion of the BRN3 positive cells to the prospective ganglion cell layer in mutant retina at E15.5 similar to the wild type (marked by arrows in the respective sections). The bars indicate 100 µm; n=3, for each embryonic stage; L, lens; R, retina; ON, optic nerve. Adapted from Vetrivel et al.,2019 under the terms of the Creative Commons Attribution License.

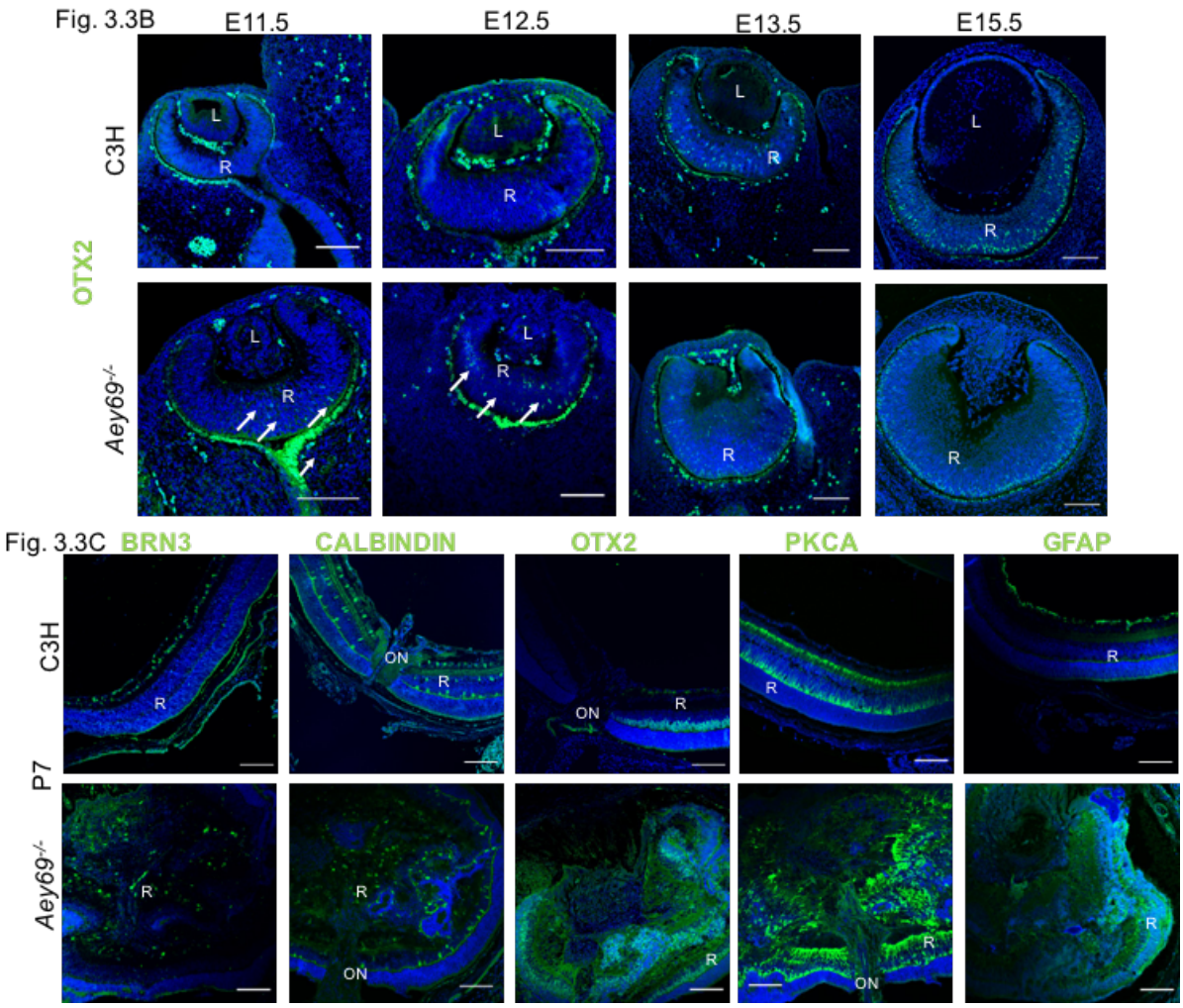

Fig. 3.3: **Retinal development in *Aey69* mutants**

B) OTX2 was used to characterize the early changes in *Aey69* mutant retina at the stages of E11-5-E13.5. The results indicate an early appearance of OTX2-positive retinal cells in the mutant at E11.5 and E12.5 (indicated by arrows at the respective stages).

C) Antibodies labeling diverse retinal cell types were used to characterize the retina at P7. The wild-type images clearly indicate that at P7 there is a stratified retina with distinct cell types: Calbindin-positive horizontal and amacrine cells, PKCa-positive bipolar cells, OTX2-positive photoreceptors and bipolar cells, GFAP-positive Müller cells, and BRN3-positive retinal ganglion cells. In the *Aey69*, these cell types were present covering the entire 'empty lens area' of the mutant eye.

The bars indicate 100 µm; n=3, for each embryonic stage; L, lens; R, retina; ON, optic nerve. Adapted from Vetrivel et al.,2019 under the terms of the Creative Commons Attribution License.

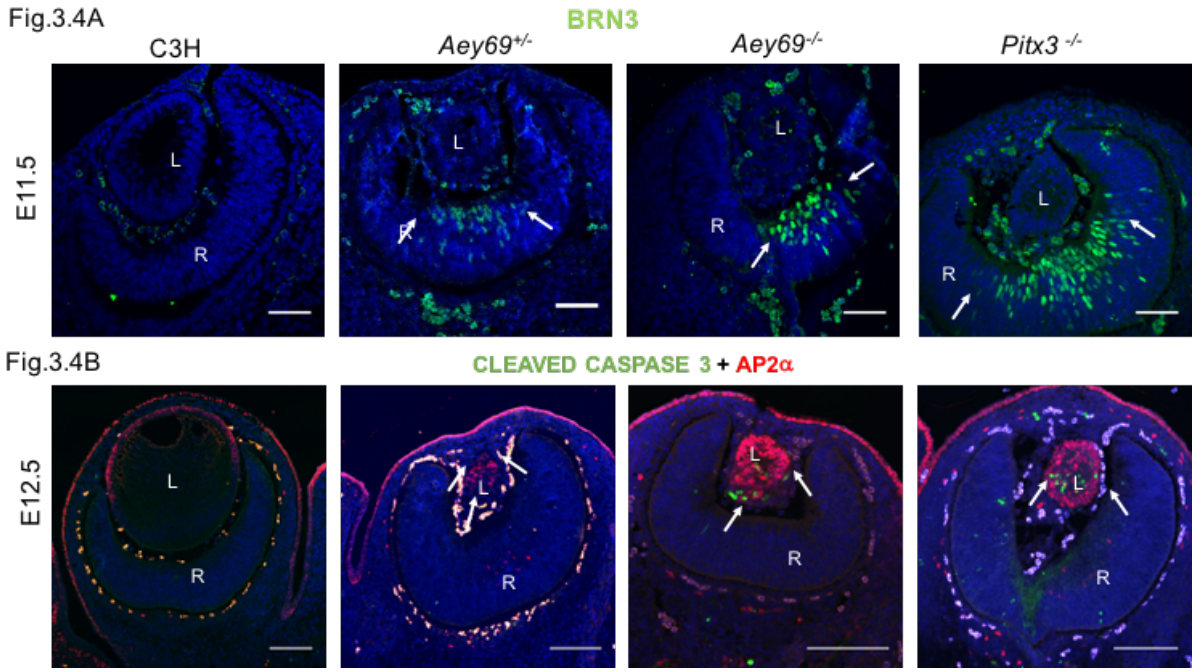

Fig.3.4 (A&B): **Apoptotic events and BRN3 earlier expression in microphthalmic mutants. A)**The ganglion cell specific marker **BRN3** was used to characterize the early retina developmental changes. The arrows in the mutant retinae at E11.5 clearly indicate an early overexpression of BRN3-positive retinal cells. **B)**The apoptotic marker **CLEAVED CASPASE 3** was used to characterize apoptotic events during ocular development at E12.5 along with the ocular transcription factor **AP2α**. The arrows marking the mutant lens indicate apoptotic cells and decreased expression of AP2α in the mutant lenses compared to the wildtype.
The bars indicate 100 µm from E11.5-E13.5; L, lens; R, retina; ON, optic nerve.

Fig.3.5

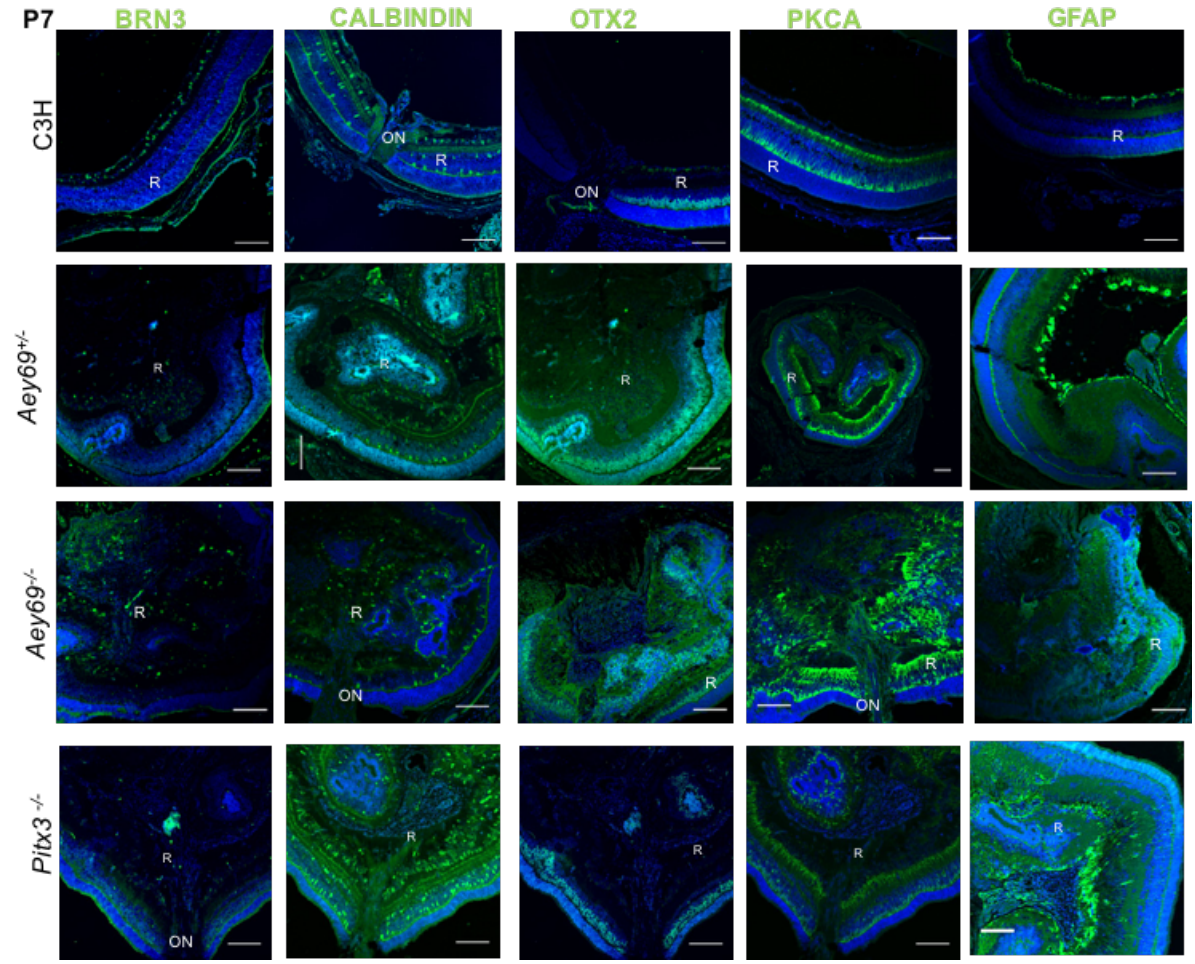

Fig. 3.5: **Presence of major retinal cell types in micropthalmic mutants.**
Antibodies labeling diverse retinal cell types were used to characterize the retina at P7. The wild-type images clearly indicate that at P7 there is a stratified retina with distinct cell types: Calbindin-positive horizontal and amacrine cells, PKCa-positive bipolar cells, OTX2-positive photoreceptors and bipolar cells, GFAP-positive Müller cells, and BRN3-positive retinal ganglion cells. In Aey69 and Pitx3 mutant mice, these cell types were present covering the entire 'empty lens area' of the mutant eye incldluing in *Aey69*$^{+/-}$. The bars indicate 100 µm; L, lens; R, retina; ON, optic nerve.

Thus, immunohistochemical analysis of lens and retinal development indicate that persistent surface ectoderm connection at E10.5 in mutant mice (*Aey69* and *aphakia*) leads to alterations in both lens and retina from E11.5. Further, the similarity between *Aey69* and *aphakia* is restricted only to these lens and retinal changes. The expression of PITX3, the microphthalmic causative factor in *aphakia*, is maintained in *Aey69*, and FOXE3 expression in *Aey69* was found to decrease without any corresponding PITX3 alteration. Finally, the pathological lens and retinal changes are observed in homozygous as well as heterozygous *Aey69* mutants.

Since *Aey69* was maintained as a homozygous mouse line, subsequent analyses were limited only to homozygous mutants.

3.3 Proliferation in *Aey69*

The disruption events happening in lens and retina of *Aey69* mutants in the early embryonic stages of E11.5-E13.5 lead to my next line of question: Are increased proliferation events causing the over expression of retinal population? If so are they restricted only to the retina, or are there any proliferation defects contributing to the apoptosing lens structure? Therefore to assess the proliferation defects, immunohistochemical distribution of pan cell cycle marker KI67 (Handa et al. 1999), cell cycle exit regulator PROX1 (Cavalheiro et al. 2014; Chen et al. 2008), and centriole organizer TUBE1 (Chang et al. 2003) were done.

KI67 was found to label completely the entire ocular section from E11.5-E12.5 in a similar manner in both the wild type and mutant (Fig.3.6A). At E13.5, restriction of KI67-stained cells in the retina was observed. There seems to be a gradual reduction of KI67-stained cells at the future inner neuroblastic layer in both the wild-type and mutant. At E15.5, in the wild type retina KI67 stained cells are restricted to a single layer posterior to the RPE. However, in the mutant the region occupied by the KI67 stained cells is comparatively larger. Taken together, it can be said that increased expression of retinal progenitor cells at embryonic stages (E11.5-E12.5) are followed by increased proliferative activities in the retina at E15.5. This overdrive of retinal proliferation events could be hypothesized to be the spear head of the retinal overgrowth covering the entire eye at the postnatal stages (Fig.1.2).

Prox1 is important for lens and retinal differentiation (Dyer et al. 2003; Tomarev et al. 1996) and is expressed in both the lens and retina. However, at E11.5-E13.5 the localization of the protein is restricted to the lens in both the wild-type and mutant (Fig.3.6B). In comparison to the cellular expression of PROX1 in the wild-type lens at E11.5-E13.5, expression of PROX1 in the mutant lens is mislocalized and follows a decreasing trend through the embryonic stages. Finally, at E15.5, there is no apparent lens structure in the mutant and PROX1 labeling is found only in the autofluorescent mesodermal cells and blood vessels. However, in the retina, expression of PROX1 is starting in an almost similar way in both the wild-type and mutant.

TUBE1 is a cell-cycle specific protein, essential for centrosome duplication in the S phase and for the formation of organized centrosome-independent microtubule asters during M phase (Chang et al. 2003). Decreased TUBE1 immunohistochemical distribution in mutant ocular sections has been speculated to be responsible for mitotic defects leading to disrupted lens

differentiation in *aphakia* (Ahmad et al. 2013). Therefore, the protein was **screened** for similar disrupted localization in *Aey69* (Fig.3.6C). Consequently, at E11.5 increased TUBE1 was seen in the mutant in comparison to the wild-type. In the succeeding stages of E12.5-E13.5 the TUBE1 signal seems to be comparable in both the wild type and mutant. No dramatic increase similar to E11.5 was observed. Interestingly, in the wild-type lens at E15.5-E17.5 track like localization of TUBE1 stained structures were observed. No such staining was observed in the mutant.

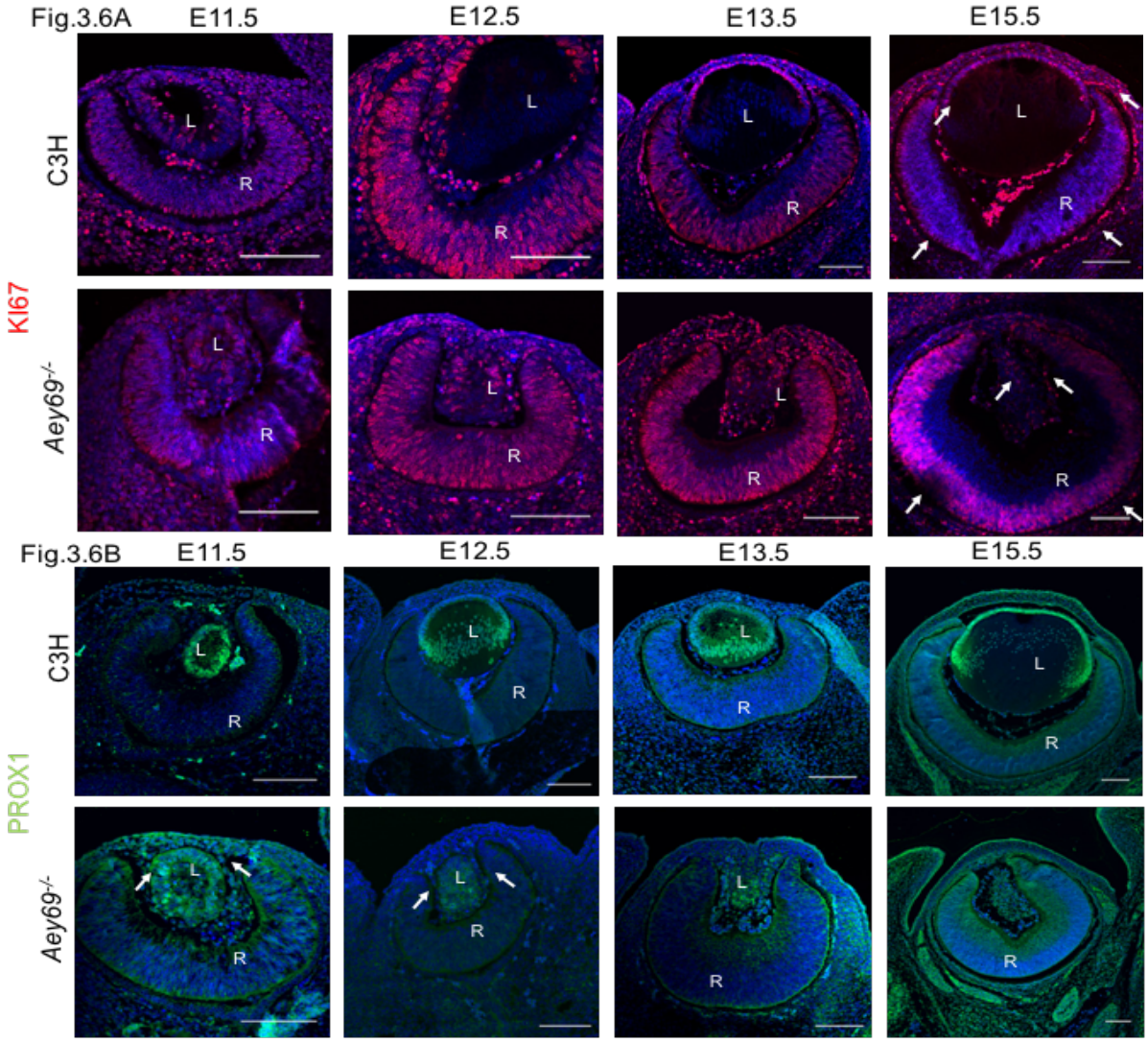

Fig. 3.6: **Proliferative dysfunctions in the *Aey69* mutant eye. A) KI67** was found to label the proliferative cells in both lens and retina through the stages of E11.5-E15.5. The main difference was found at E15.5, wherein the wild-type retina KI67 positive cell population seems to be restricted to the future outer neuroblastic layer (marked by arrows). Adapted from Vetrivel et al.,2019 under the terms of the Creative Commons Attribution License. **B) PROX1** immunostaining was used to characterize differentiation events in the developing eye of wild types and mutants. Prox1 expression was found to be restricted to the lens through the stages of E11.5-E13.5 . Arrows in mutant lens indicate the reduced and altered distribution of PROX1 at E11.5 & E12.5.

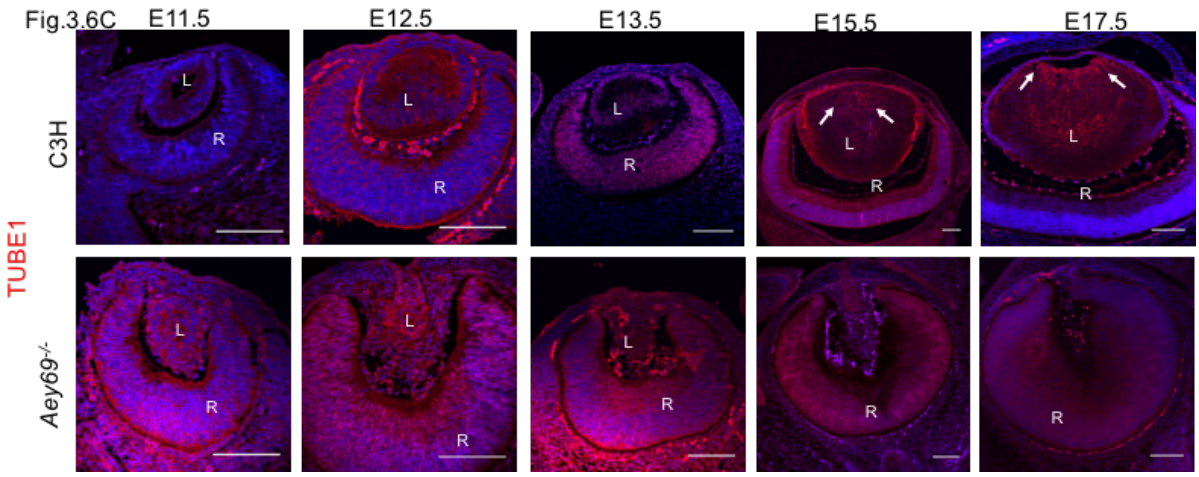

Fig. 3.6: **Proliferative dysfunctions in the *Aey69* mutant eye**. **C)** The temporal distribution of centriole organizer **TUBE1** is given through the stages of E11.5-E17.5. Increased epsilon-tubulin was observed in the mutant lens at E11.5.Additionally arrows in the wildtype lens at E15.5-E17.5 indicate a track like staining pattern of epsilon tubulin.
The bars indicate 100 µm; n=3 for each embryonic stage. L, lens; R, retina; ON, optic nerve.

3.4 Analysis of microarray data

The microarray results (Vetrivel et al.2019) were analyzed by characterizing the expression of the top altered genes at different stages. The top altered validated genes were:

- E9.5: *Pmp22, Pdk1, Brd2,*
- E10.5: *Efnb2, Psdm12, Ptipmn12*
- E11.5: *Foxc1, Sparc, Rbbp7*

In addition, among the dysregulated genes across the embryonic stages (E10-E13), *Erdr1* and *Hes5* were found to be significantly altered at more than one stage. Therefore, their expression was checked in more than one stage (E10.5 to E13.5). As can be seen in Fig.3.7A-D, the selected genes at E9.5 and E10.5 were found to show the similar trend of altered expression at the chosen stages. The selected genes at E11.5 were not found to fold expression changes similar to their expression in microarray (Fig.3.7C). As for *Erdr1* and *Hes5* microarray data indicates fluctuating pattern of gene expression with downregulation at E10.5, E11.5, E13.5 and upregulation at E12.5. However, in QPCR a similar expression trend is found only at E10.5. The discordant results could be explained by the selection of the sample area used in microarray: E11.5 (region around eye), E12.5 (region around eye) and E13.5 (eye). Contrarily, in QPCR the whole embryo was used at all stages.

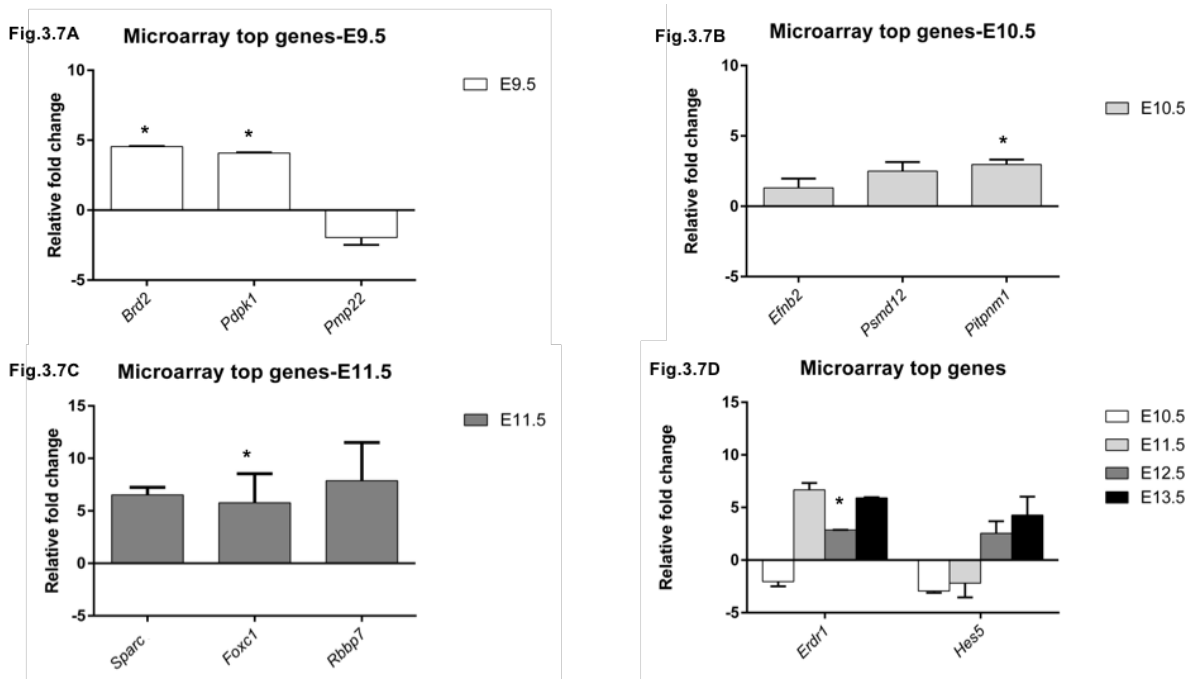

Fig.3.7A-D: **Validation of the top altered genes from microarray by QPCR**
Top altered genes from microarray were analyzed in their respective stages. Relative fold change was calculated by -2**ΔΔ**ct method by taking the respective wild-type tissue as the control. *B2m* was taken as the housekeeping gene. Statistically significant expression levels ($p < 0.005$) are marked by an asterisk. Expression pattern was found to be consistent to the microarray at E9.5 & E10.5. n=3 for each embryonic stage.

Further comprehensive expression analyses was restricted to the validated stages of E9.5 and E10.5. As seen from the histology results in Fig. 1.2, the pathophysiological changes in *Aey69* become more pronounced from E11.5-E12.5. Therefore, differentially expressed genes at E9.5-E10.5 could indicate potential targets/regulators triggering this change. Analyses was done based on the upstream regulator analysis in Ingenuity pathway analysis (IPA) using "lens" and "retina" as tissue filter. The pathway analysis examines, how many known targets of possible upstream regulators are present in the microarray dataset based on the literature. An overlap p-value is computed based on significant overlap between genes in the dataset and known targets regulated by the transcriptional regulator (Saili et al. 2013). Based on this approach a shortlist of potential upstream regulators across the various embryonic stages was generated.

Potential upstream regulators from IPA analysis was found to be: Creb1-E9.5 (p-value of overlap: 1.87E-02), VAX2- E10.5 (p-value of overlap: 1.75E-02). Apart from the IPA analysis prediction Bmpr1a, encoding a receptor for BMPs, of which BMP4 and BMP7 (Williamson and FitzPatrick 2014) are known to be important for early eye development was found to be amongst the top altered genes at E9.5 in microarray. Therefore, the predicted regulators (along with *Bmpr1a*) were analyzed at E10.5-E12.5. And also taking advantage of the

published research the upstream regulators were analyzed along with their known associated factors to get a comprehensive overview of the dysregulated factors in *Aey69*. Table 3.1 gives an outline of the genes, their associated factors and their association with ocular development (Total genes=14).

Interestingly, *Creb1* and *Bmpr1a* along with their associated factors were found to follow a biphasic pattern with strong downregulation at E10.5 followed by upregulation at E11.5 (Fig.3.8A-C). In addition, the ligand/downstream effector of the Bmpr1a geneset (*Bmp4*, *Bmp7* in Fig.3.8A) were found to be significantly downregulated at E12.5. Such a significant downregulation of ligands at E10.5 and E12.5 was also found in *Vax2* geneset with *Epha3* and *Efna5* (Fig.3.8C). This pattern could indicate that the co-ordianted expression of downregulation and upregulation found amongst the factors at E10.5-E11.5 is lost at E12.5.

Table 11: List of genes analyzed by QPCR based on Ingenuity Pathway Analysis.

Gene	Associated factors	Function	Mice studies	Reference
Bmpr1a	*Bmp4, Bmp7, Smad1, Smad5*	Lens specification and differentiation.	Disurpted optic fissure closure.	Huang et al.,2015
Vax2	*Efnb2, Efna5, Epha3*	Eye dorsal ventral axis specification.	Misrouting of the optic fibres and coloboma.	Barbieri et al., 1996
Creb1	*Crem, Atf1, c-maf, Snf2h*	CRYAA regulation.	Defective lens fiber differentiation.	Yang et al., 2006, Kawauchi et al.,1999

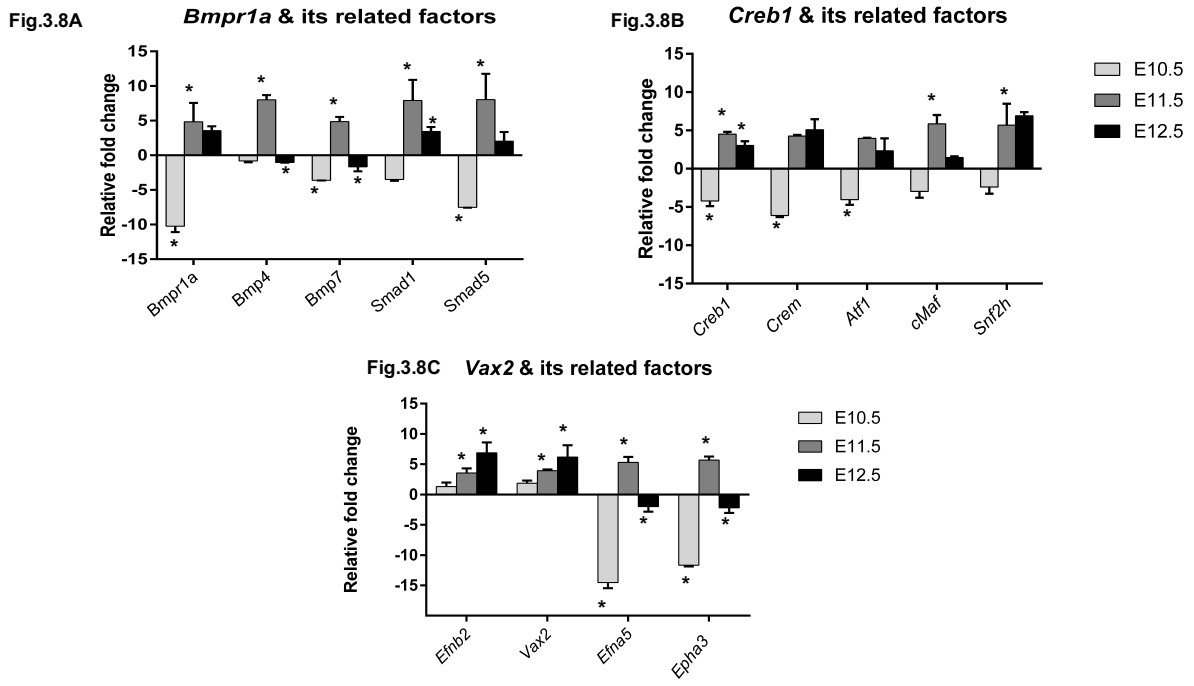

Fig.3.8A-C: **QPCR analysis based on predicted upstream regulators from IPA and the top altered genes at E9.5-E10.5.**

The predicted upstream regulators were *Creb1* (E9.5) and *Vax2* (E10.5). And the top altered genes were *Bmpr1a* and *Efnb2*. The components of the respective geneset were analyzed at the histopathologically relevant stages of E10.5-E12.5. The components were found to show a biphasic expression pattern with downregulation at E10.5 and upregulation at E11.5. Relative fold change was calculated by -2**ΔΔ**ct method by taking the respective wild-type tissue as the control. *B2m* was taken as the housekeeping gene. Statistically significant expression levels ($p < 0.005$) are marked by an asterisk. n=3 for each embryonic stage.

Thus, the top altered genes at E9.5 and E10.5 were validated by QPCR. The predicted upstream regulators and its associated factors were found to distinct phases of expression: Downregulation at E10.5, followed by upregulation at E11.5 and diverse expression alterations at E12.5.

Objective 2: Analysis of the mutant genes in *Aey69*.

The next point of analysis was to look at which of the mutated genes in *Aey69* (*Gja8* and *Hist2h3c1*) is responsible for the ocular alterations.

3.5 Mutant genes in *Aey69*

3.5.1 *Gja8*.

The distribution of GJA8 in the lens has been extensively characterized from the stage of E14.5 (Yu et al. 2019). However, there has been no immunohistochemical characterization of it in earlier stages (E11.5 and E12.5). A comparative immunohistochemical analysis of GJA8 expression was done in wild type, *Aey69* and *aphakia* mutants at E11.5 and E12.5 (Fig.3.9). At E11.5, in the wild-type GJA8 expression covers the entire lens vesicle, while in *aphakia* mutant the expression seems to be highly irregular and restricted to one part of the mutant lens vesicle. Interestingly, at this stage, no GJA8 expression is seen in the *Aey69* mutant. Furthermore, at E12.5, GJA8 expression becomes more restricted to the region beneath the future lens epithelial layer. In the *aphakia* mutant, the one-sided expression of GJA8 continues in the disorganized lens structure. In the *Aey69* mutant, however, no comparable expression to either the wild type or aphakia mutant was found at both stages. In fact, it could be said that there is no characteristic expression of GJA8 in the *Aey69* mutant.

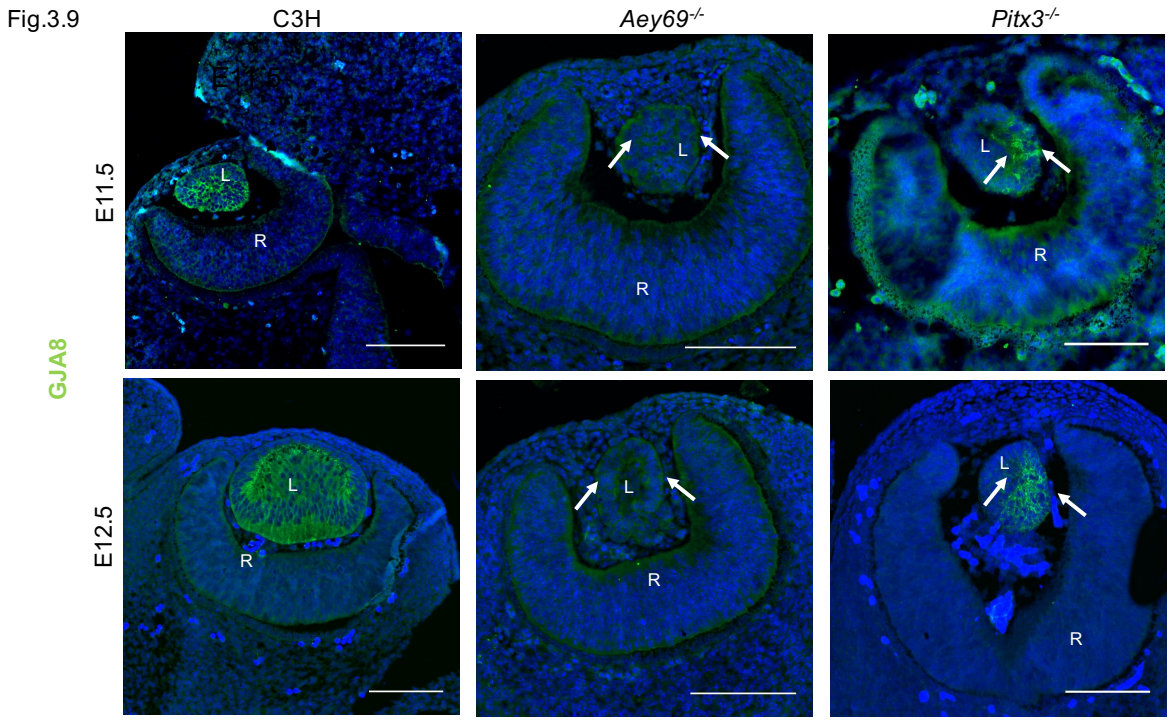

Fig.3.9: **GJA8 in early eye development**
Fig.3.9 shows the immunohistochemical distribution of **GJA8** at E11.5-E12.5 in wild type, *Aey69* mutant and similar microphthalmic mouse model *Pitx3*$^{-/-}$, *aphakia*. The shrinking lens region is marked in the mutant models by white arrows. There was no obvious immunohistochemical localization of **GJA8** in the mutant *Aey69* eyes at the stages of E11.5 - E12.5. The bars indicate 100 µm. n=3 for each embryonic stage. L, lens; R, retina.

3.5.2 *Hist2h3c1*

QPCR:

Hist2h3c1 is one of the eight genes encoding for the protein histone H3.2. To test for any tissue-specific dependence amongst the histone clusters expression pattern of these genes were analyzed in wild-type tissues – brain, liver, retina, lens (Fig. 3.10A). *Hist2h3c1* was found to be most highly expressed isoform in lens. In the brain, *Hist1h3d* was found to the highly expressed isoform, in liver, brain and retina. With regard to embryonic stages (Fig. 3.10B), there was a significant downregulation of the histone gene *Hist1h3b* in E10.5 and *Hist2h3c1* at E10.5-E12.5 ($p < 0.05$), but the overall expression levels of H3 genes was not dramatically changed (using universal H3 primer; Banday et al. 2014).

Immunohistochemistry:

For the localization of *Hist2h3c1* encoded protein no commercial antibodies are available that could effectively distinguish H3.2 from H3.1, H3.3 in chromatin, whereas antibodies against many different posttranslational modifications were readily available. Therefore, in the absence of specific H3.2 antibody histone PTM modification were tested across different embryonic stages. These involve markers of transcriptional regulation, H3K122me1 (Garcia et al. 2007) and mitosis, H3S10P (Hendzel et al. 1997), respectively. For H3K122me1, a strong localization was observed in the surface ectoderm in both the wild-type and mutant eyes at E11.5 - E12.5. However, no major differences were observed between wild-type and mutant at the analyzed stages (Fig.3.11). The absence of changes in the H3K122me1modification could be interpreted as: non-existence of H3K122me1 PTM bearing H3.2 does not carry at the particular stages or the mutation does not affect the modifications at a structural level.

Fig.3.10A

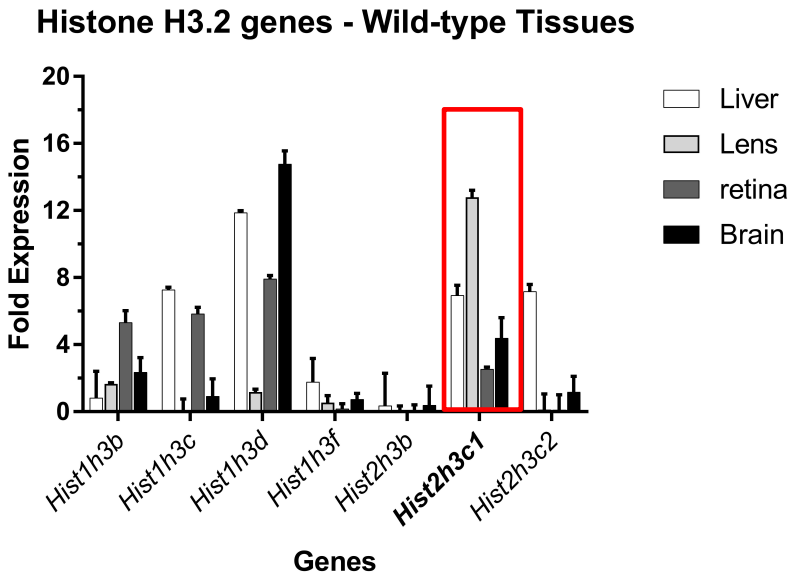

Fig.3.10B

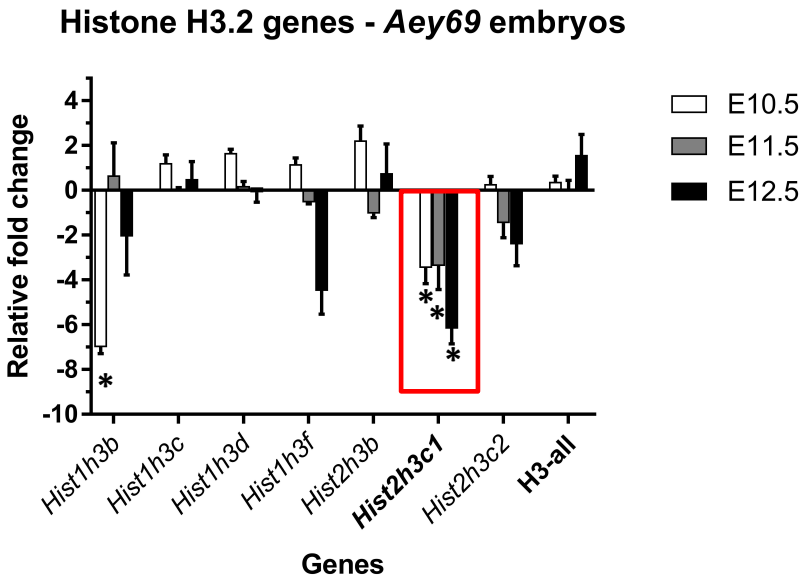

Fig.3.10: **QPCR analysis of Histone H3.2 coding genes**. **A)** Relative expression levels of histone genes in the wild-type tissues of brain, liver, lens and retina. *Rplp0* (ribosomal protein, large, P0) was taken as the housekeeping gene, and analysis was done using the relative expression method. Values are given as fold expression levels ± SEM; n=3 for each tissue type. The gene of interest, *Hist2h3c1*, is highlighted by a red box; *Hist2h3c1* was found to be the most highly expressed H3.2 encoding gene in the lens.**B)** Gene expression changes in the embryonic tissues of *Aey69* at the embryonic stages of E10.5-E12.5 using the -2**ΔΔ**ct method; the respective wild-type tissues were used as the control, and *Rplp0* was taken as the housekeeping gene. Values are given as fold expression levels ± SEM. n=3 for each embryonic stage. Statistically significant differences of the expression levels ($p < 0.005$) are marked by an asterisk. The mutated gene *Hist2h3c1* (red box) was found to be significantly downregulated through these stages.

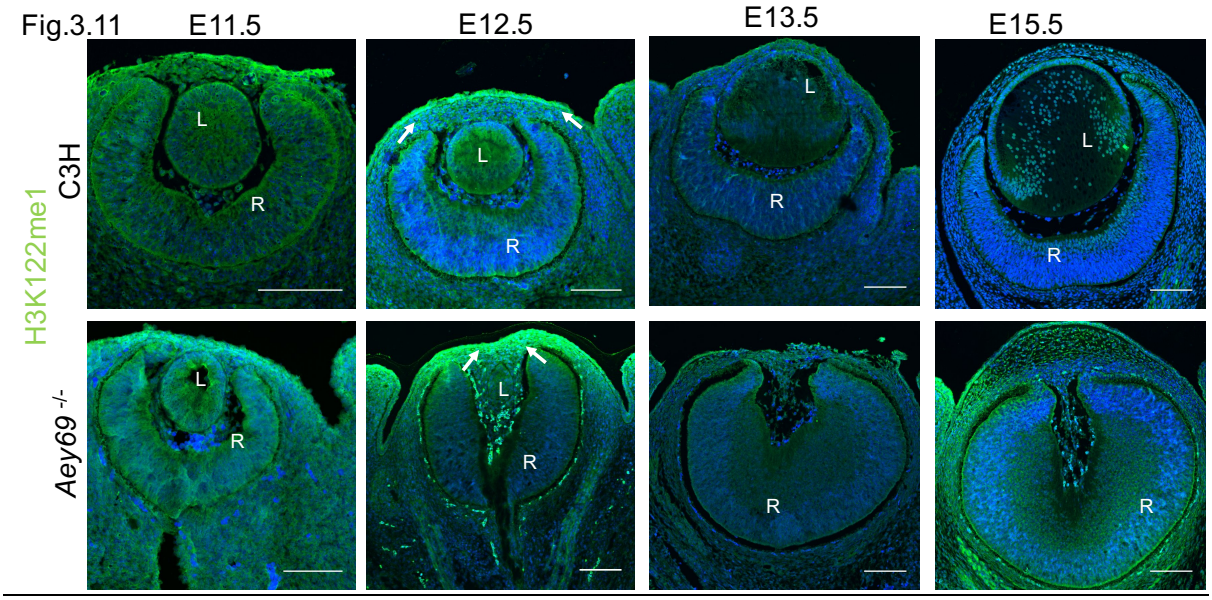

Fig.3.11: **Immunohistochemical analysis of H3K122me1.**
The distribution of the Histone H3 PTM - **H3K122me1** associated with transcriptional regulation is shown through the stages of E11.5-E15.5. A strong signal of the PTM is observed in the future cornea region in both the wildtype and mutant at E12.5 (indicated by white arrows). No major deviations in localization were found in the mutant in comparison to the wildtype. Bars indicate 100 µm. L,Lens; R, retina; ON, optic nerve.

The only change I found was in the distribution of mitotic marker H3S10P, which was mislocalized in the developing lens and retina. Phosphorylation of serine residue at position 10 at histone H3 is a highly dynamic process that initiates at pericentromeric heterochromatin regions, then spreads along the entire length of chromosomal arms to reach the maximal abundance during mitosis and then gradually decreases (Sawicka and Seiser 2012). Initially punctate H3S10P staining are observed in interphase cells (Crosio et al. 2003; Hendzel et al. 1997). At prophase, the cells have condensed chromosomes bearing H3S10P marker taking up most of the cellular area (Hans and Dimitrov 2001; Le et al. 2013). In metaphase, the condensed chromosomes bearing H3S10P marker are aligned at the metaphase plate and in anaphase/telophase, H3S10P is gradually lost from the diverging chromosomes (Ribas et al. 2012). A representative figure detailing the different spatial distributions of H3S10P in cell cycle is are represented in Fig.3.12.

Fig.3.12

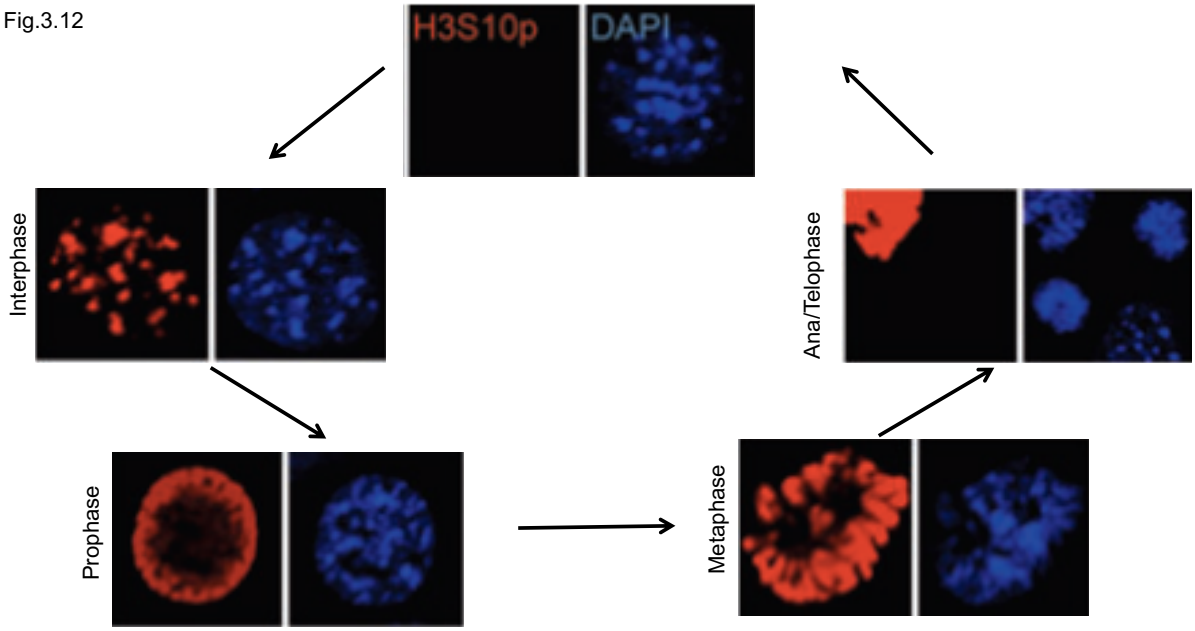

Fig.3.12: **H3S10P shows dynamic distribution during mitosis.**
Mouse embryonic fibroblasts were were doubly stained for **H3S10P** (red) and **DAPI** (blue). The first observance of H3S10P is at Interphase when H3S10P and DAPI label the chromosome spreads as punctate dots. At Prophase the staining is observed homogenously around the condensed mitotic chromosome. At Metaphase the staining is observed around the separating chromosomes. At Ana/Telophase the H3S10P is gradually decreasing and later no H3S10P is observed until the cell prepares for interphase. Adapted from Jeong et al.,2010 with permission form Molecular Biology Society of Japan/Blackwell Publishing Ltd

In the *Aey69* mutant, more H3S10P marked cells were found from E11.5, and the H3S10P stained cells showed an atypical, non-nuclear H3S10P staining in the mutant (Fig.3.13A). The next line of analysis was: what does this alteration mean for the spatial distribution of H3S10P at different cell phases. In the embryonic sections, the following spatial locations could be characterized – Prophase, Interphase and aberrant cells (Fig.3.13B). The aberrant cells represent cells that cannot be categorized as mitotic cell according to Fig.3.10. These three cell types, namely Prophase, Interphase and aberrant cells, were counted in wild-type and mutant sections (3 biological replicates) through the embryonic stages of E11.5-E13.5 (Fig.3.13(i-iii)).

As can be seen from Fig.3.13(i) there is a gradual increase in the number of prophase cells in both the wild type and mutant. On the other hand, the number of cells in interphase is slowly following a decreasing trend in both the wild type and mutant (Fig.3.13(ii)). This opposing trend in prophase and interphase could indicate that as development proceeds an increasing number of cells leave interphase and begin mitosis in both the wild type and mutant. These

cell counts were not found to be significantly different in the mutant, though there was a trend for more number of stained cells in mutant sections. There were very few/no aberrant cells were not found in any of the wild-type sections at E11.5, while at E12.5-E13.5 cells with irregular pattern were observed and taken as aberrant cells. These could represent either dying cells/highly proliferative cells in the wild-type as a part of normal differentiation process. However, in mutant there were significantly more dysregulated cells through the stages of E11.5-E13.5 (Fig.3.13(iii)). Cumulatively, the analyses hints at higher appearance of mislocalized H3S10P cells in the mutant.

Another interesting observation was the presence of larger stained structures at the stages of E12.5 in the lens (Fig.3.14A). Therefore, the second point of analysis was the size and fluorescence intensity of stained area of H3S10P signal at stages of E11.5-E13.5. The size and fluorescent intensity of the H3S10P stained cells were found to be significantly higher than the wild type (Fig.3.14(i-ii)). Taken together, it could be said that large H3S10P structures (which constitute as aberrant cells in cell count) dominate the mutant eyes at all stages. These structures could be hypothesized as cells not able to divide and pass through cell cycles. After the disappearance of the lens structure at E13.5 in the mutant, the trend for increased H3S10P stained cells continues through the stages of E15.5-P7 (Fig.3.15). After birth at P7, very less H3S10P stained cells restricted to the lens epithelium and at the retinal region near the iris ciliary body margin were found in the wild type. However, in the mutant retina mitotic events proceed with comparatively larger prophase cells in the retinal cells, filling up the empty 'lens-space'.

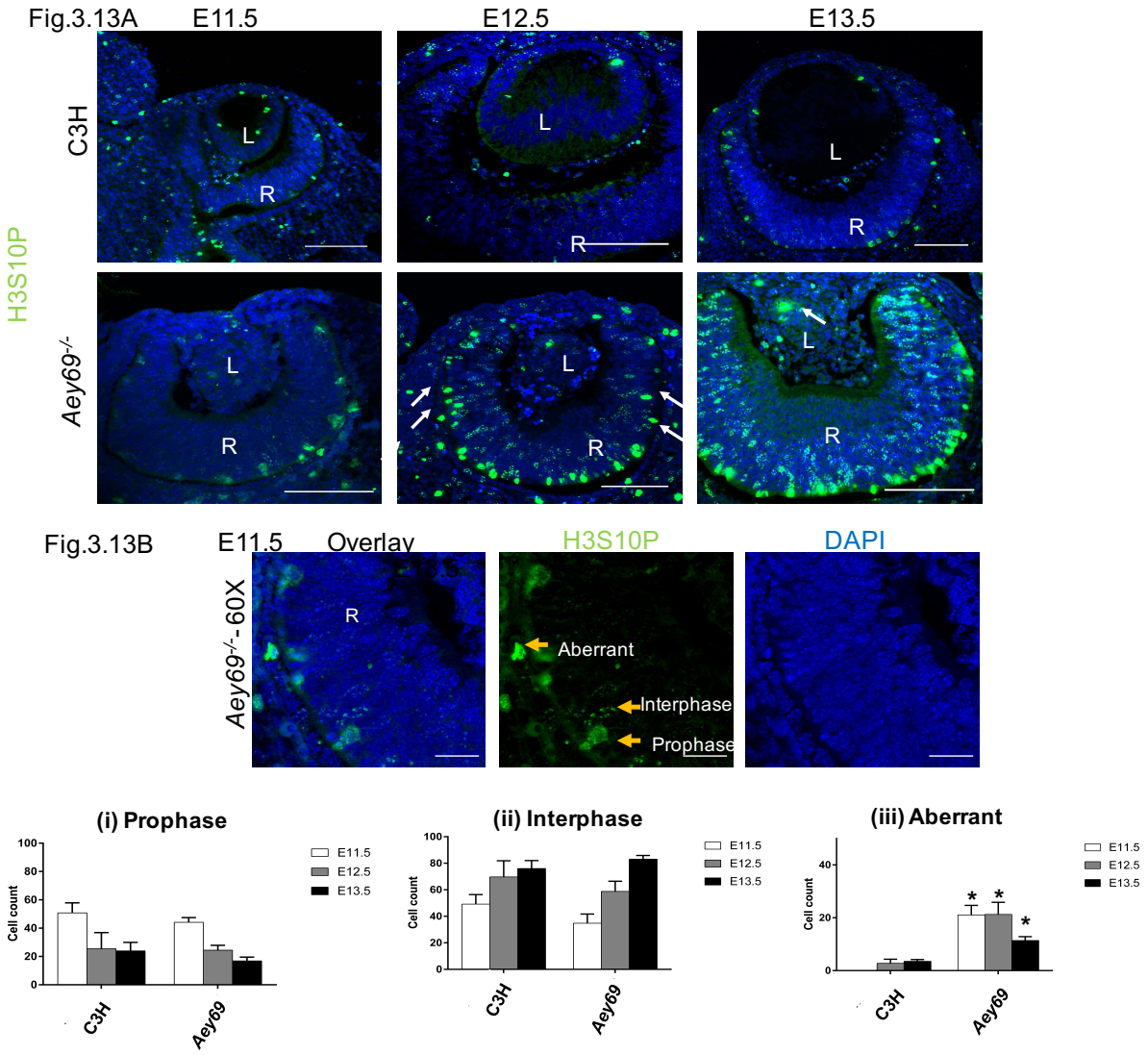

Fig.3.13: **Alteration of Histone H3 PTM H3S10P in *Aey69* (E11.5-E13.5). A)** The immunohistochemical distribution of **H3S10P** was characterized through the stages of E11.5-E12.5. White arrows in the mutant at E12.5 indicate the presence of numerous H3S10P positive cells in the mutant compared to the wild type. While at E13.5, differentially stained H3S10P positive structure was observed in the mutant lens(shown by white arrows) . L, lens; ON, optic nerve; R, retina. The bars indicate 100 µm. **B)** The different spatial distributions of H3S10P that can be identified in the embryonic sections are shown. Based on this the cells bearing different H3S10P spatial localization were counted using ImageJ (i-iii)). There was no difference in the distribution of prophase and interphase cells between the wildtype and mutant through the stages of E11.5-E13.5 (i-ii). The number of aberrant cells were found to be significantly higher in the mutant (iii). R, retina. n=3 for each embryonic stage. The bars indicate indicate 25 µm.

Fig.3.14A

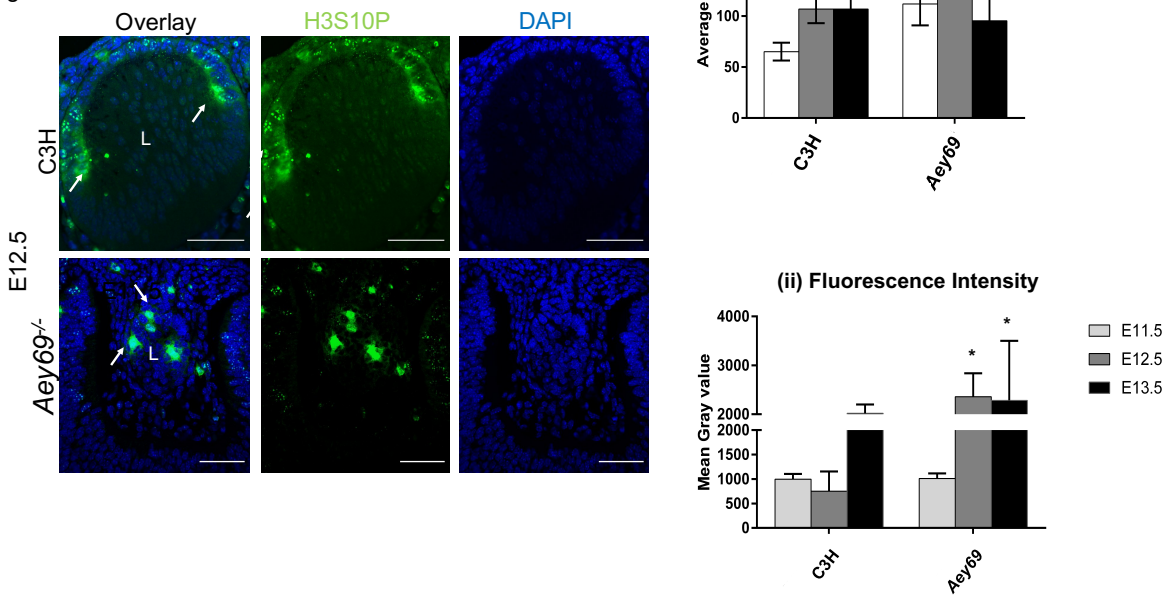

Fig.3.14: **Quantitative analyses of Histone H3 PTM H3S10P in *Aey69* (E11.5-E13.5)**
Quantitative analyses of H3S10P were based on size and fluorescence intensity. The area occupied by the H3S10P stained cells were found to be significantly higher in the mutant at E11.5-E12.5 (i-ii). And the fluorescence intensity of H3S10P was increasing consistently in the mutant(ii). n=3 for each embryonic stage. The bars indicate 50 μm. L, lens; R, retina.

Fig.3.15

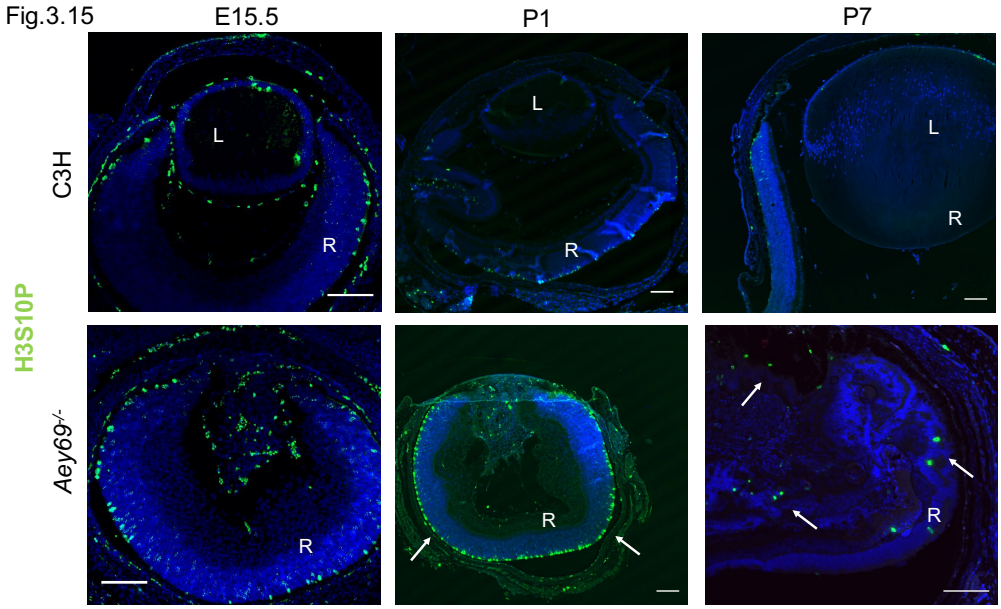

Fig.3.15: **Alteration of H3S10P in *Aey69* (E15.5-P7)**
The alteration associated with H3S10P was found to sustain through development. Higher number of irregularly stained H3S10P cells were identified in the mutant (shown by white arrows). The bars indicate 100 μm. n=3 for each embryonic stage. L, lens; R, retina.

Objective 3: Evaluation of the nature of mutation in *Hist2h3c1*.

Following the confirmation of mutant *Hist2h3c1* to play a pivotal role in *Aey69* pathology, the next point of analysis was: how the mutant changes the function of the gene? Two hypotheses were framed for this:

- The mutation creates/modifies binding sites for potential miRNA partners.
- The mutation changes the structural conformation of the protein.

3.6 Structural changes attributed to the mutation: miRNA vs protein.

3.6.1 miRNA:

Single nucleotide changes have been found to increase, decrease, or completely disrupt the binding efficacy of miRNAs (Bhaumik et al. 2014). Hence a possible hypothesis would be that this specific single nucleotide mutation would be the source of *Aey69* pathology through potential miRNA partners (Wang 2016). RegScan identified *mmu-miR-5627-5p* as the prime candidate having the seed region in the mutation sequence, while miRDB identified *mmu-miR-204-5p* as the prime candidate. These candidate miRNAs were then taken up for further analysis by stem loop qRT-PCR to quantify their co-expression with the mutated *Hist2h3c1*gene (Fig.3.16). miRNA analyzed were found to show downregulation at the specific stages indicating no influence of the gene on the histone mRNA.

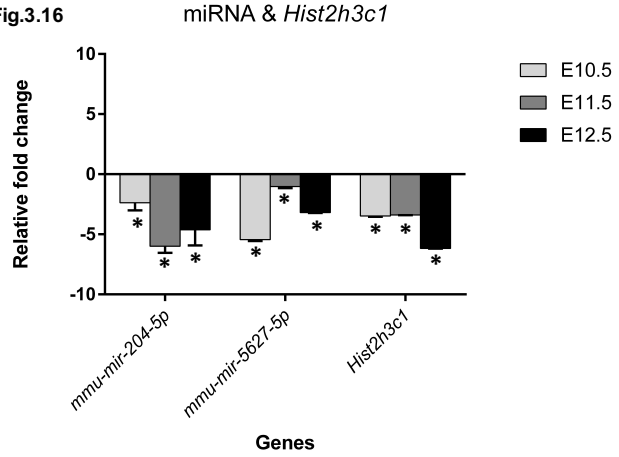

Fig. 3.16: **QPCR analysis of miRNA candidates**

The expression of *mmu-miR-204-5p* and *mmu-miR-5627-5p* were quantified in relation to the housekeeping gene of *Sno-202*. *Hist2h3c1* was quantified in relation to the housekeeping gene of *Rplp0*. Embryonic stages of E10.5 - E12.5 were chosen for analysis. Values are given as fold expression levels ± SEM; n=3 for each tissue type. Statistically significant expression levels ($p < 0.005$) are marked by an asterisk. The miRNAs as well as *Hist2h3c1* were found to be significantly downregulated in the mutant.

3.6.2 Protein:

A combination of QUARK-based *ab-initio* folding with template-based I-TASSER structure assembly has been reported to improve the quality and robustness of protein models (Zhang 2014). Therefore, a combination of both the approaches were used to generate respective wild-type and mutant protein structures, followed by RMSD calculation of the aligned structures using Pymol. I-Tasser predicted the wild-type and mutant proteins to be structurally distinct by a RMSD value of 1.352 Å. While, QUARK predicted the proteins to be structurally distinct by a RMSD value of 14.584 Å. In addition, the ligand binding hit structures – given by I-Tasser found structures similar to the mutant histone protein to exist in histone SIN mutant nucleosome crystal structures. SWI/SNF-independent (*SIN*) histone mutants were first identified in a genetic screen in yeast and are clustered in the L1L2 region of the $(H3–H4)_2$ tetramer that organizes the central two turns of nucleosomal DNA (Kurumizaka and Wolffe 1997; Muthurajan et al. 2004). The *SIN* mutations were found to alter transcription-dependent nucleosome occupancy at highly transcribed genes (Hainer and Martens 2011). These mutations were found to cause pleiotropic phenotypes in yeast including slow growth and temperature sensitivity (Fleming and Pennings 2001).

To further analyze, the similarity of H3.2Ile120Leu to reported *SIN* mutants, structural analyses of the protein in (H3–H4) complex and then in nucleosome were determined by *in-silico* approaches. Wild-type and mutant proteins were docked against H4 protein using two independent online docking software tools: GrammX and PatchDock. Alignment of the docked structures by Pymol found a divergence of 2.688 (GrammX) and 1.725 (PatchDock). Gaussian network model (GNM) analysis of the flexibility of the nucleosome containing the wild-type and mutant protein also indicated mobility of the histone residues around the nucleosome to be altered (Fig.3.17). Taken together, the *in-silico* predictions indicate the mutant protein to be structurally different to the wild-type and it could be speculated to create functional changes in the nucleosome similar to *SIN* mutants. To analyze, whether the mutation is causing any changes related to Swi-SNF complexes the expression pattern of the nucleosome assembly factors - *Smarca4*, *Smarcc5*, *Smarcd1*, *Smarcad1* & *Smarcc2* were analyzed in the stages of E10.5-E12.5. A fluctuating expression pattern was observed in the nucleosome assembly factors analyzed with significant upregulation at the pathological stage of E11.5. The QPCR results were validated by IHC for *Smarca4* (Fig.3.18 and Fig.3.19).

Fig.3.17

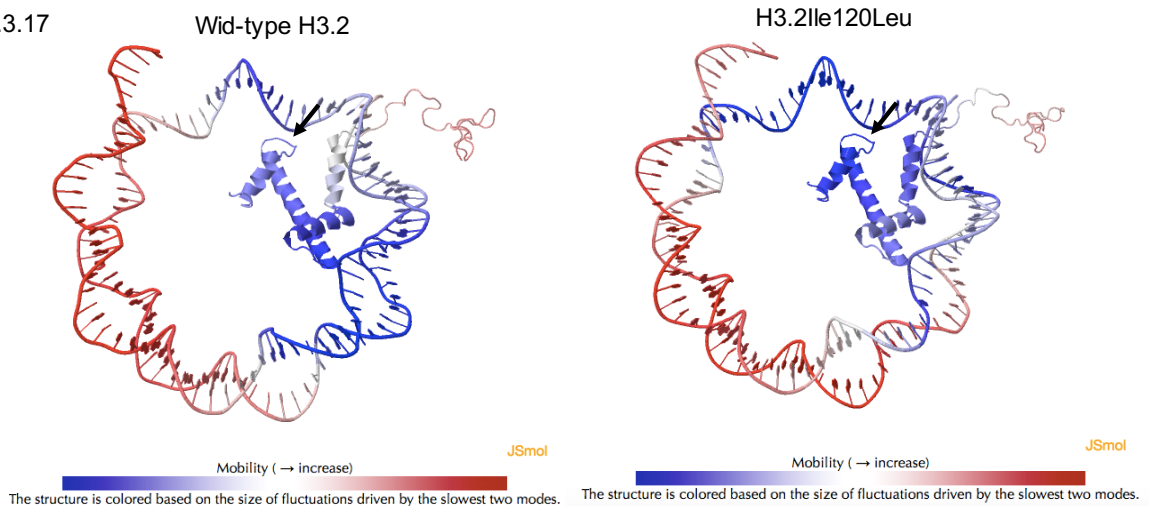

Fig.3.17: **Flexibility analysis of the nucleosomes**
Gaussian network model (GNM) was used to characterize the flexibility of the nucleosome containing the wildtype and mutant protein (H3.2Ile120Leu). The mutation site is highlighted by black arrows. The flexibility of the residues around the mutation site (specified by increased blue color) is found to be decreased in the mutant with respect to the wild-type.

Fig.3.18 SWI/SNF chromatin remodling factors

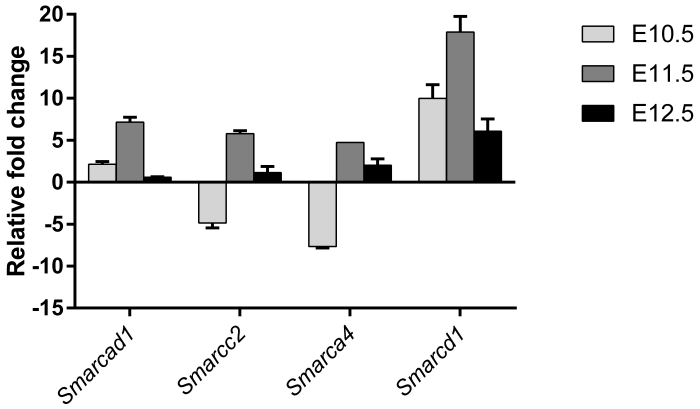

Fig.3.18**: QPCR analysis of SWI/SNF chromatin remodeling factors.**
The factors were analyzed at the histopathologically relevant stages of E10.5-E12.5. The analyzed factors were found to show significant upregulation at E11.5. Relative fold change was calculated by -2ΔΔct method by taking the respective wild-type tissue as the control. *B2m* was taken as the housekeeping gene. Statistically significant expression levels ($p < 0.005$) are marked by an asterisk. n=3 for each embryonic stage.

Fig.3.19

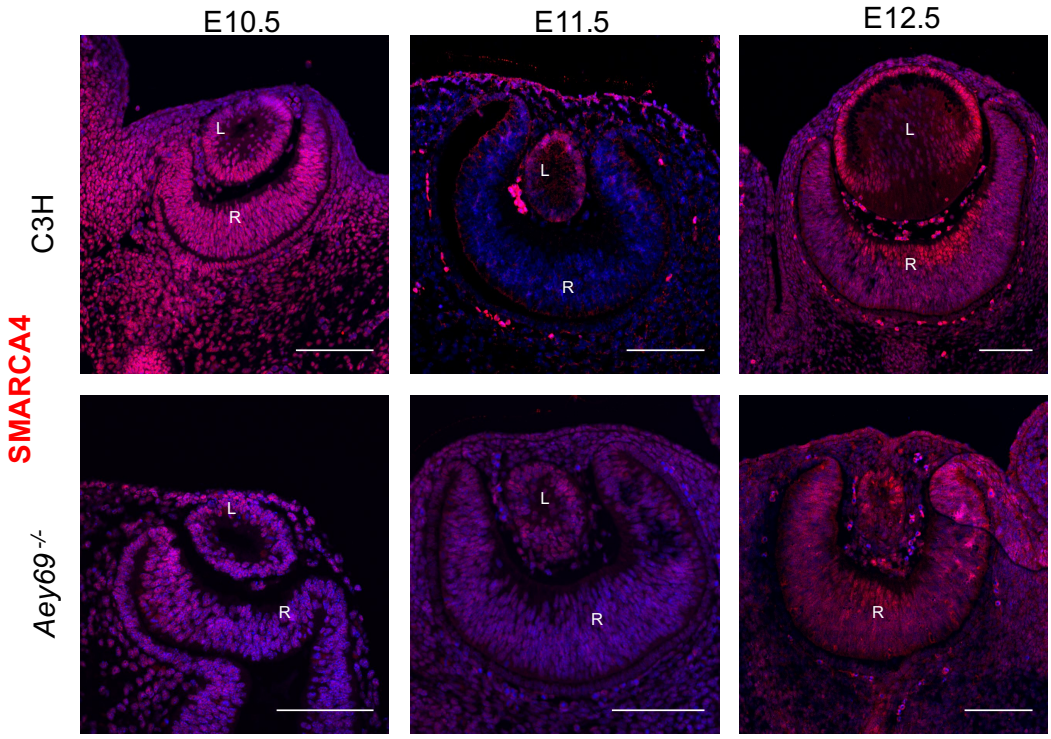

Fig.3.19: **SMARCA4 in *Aey69***
The distribution of chromatin remodeling factor **SMARC4** was characterized in the ocular sections the from the stages of E10.5-E12.5. At E10.5, no major change was observed in the distribution of the protein between the wild type and mutant , but the intensity was found to be qualitatively lesser,. At E11.5 in the wild type SMARCA4 was observed only in the lens (indicated by white arrows) , however in the mutant it is distributed in the lens and retina (indicated by white arrows). No major changes were found at E12.5. The bars indicate 100 µm; n=3 for each embryonic stage; L, lens; R, retina; ON, optic nerve.

I, then, tried to validate this hypothesis based on *in-silico* results by X-ray crystallography analysis of the nucleosome containing mutant histone protein sequences. The required histone proteins were made by the recombinant approach (Fig.3.20). For the formation of nucleosome, a step-by-step dialysis protocol was set up and optimized. The final product was then purified by the size exclusion chromatography using the column Superdex200 increase (Fig.3.21). And the final concentration of the nucleosome was analyzed by SDS-PAGE (Fig.3.22).

Fig.3.20

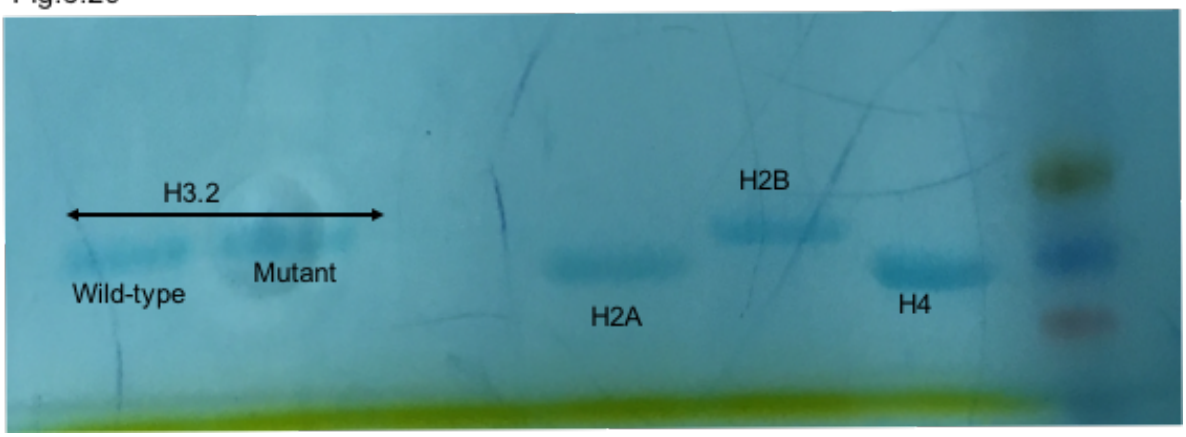

Fig.3.20: **SDS PAGE for the recombinant histones.**
The core histones H2A, H2B and H3.2 proteins (Wild-type and mutant) were produced by recombinant approach. The purified proteins were then resolved on 15% SDS PAGE. Bands were observed in the respective wells corresponding to their molecular weight. KD – KiloDalton.

Fig.3.21

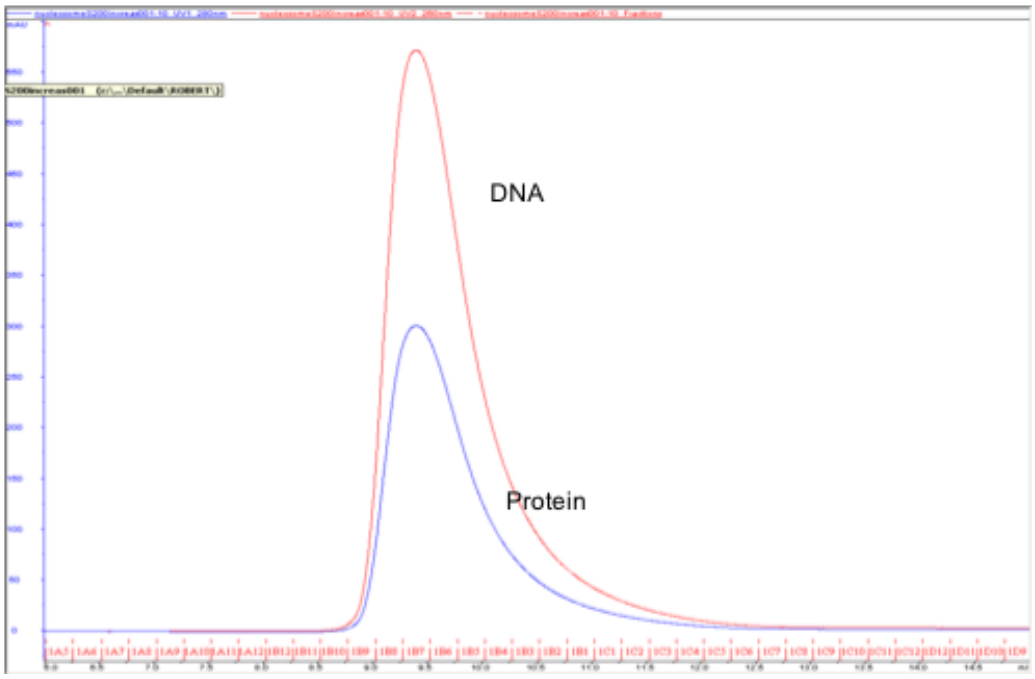

Fig.3.21: **Chromatogram profile of the assembled nucleosome.**
Nucleosome assembled by step by step salt gradient dialysis method was passes through size exclusion column SAU200. Nucleosome containing DNA and the core histone proteins eluted as a single complex as shown by the appearance of the single peak. The presence of DNA is shown by the red peak which corresponds to the biological molcules detected at 280 nm. The presence of protein is shown by the blue peak which corresponds to the biological molcules detected at 260 nm.

Fig.3.22

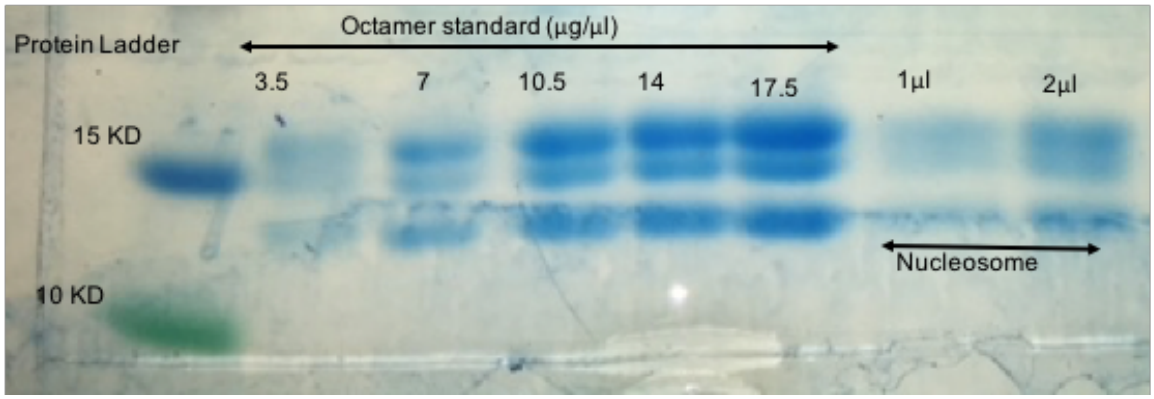

Fig.3.22: **SDS PAGE based estimation of the concentration of the assembled nucleosomes.**

Recombinant octamer containing H2A, H2B, H3.2 (mutant) and H4 histone proteins were prepared in different concentrations. The octamers were then resolved on 15% SDS PAGE along with different volumes of the assembled nucleosome. Concentration of the nuclesome was estimated in a semi-quantitative manner based on the intensity of the bands observed. KD - Kilo Dalton.

Crystallization conditions was optimized using different crystallization screens in 96 well plates. Various small crystals appeared in the following conditions (Fig.3.23). The conditions were further optimized by manual set up and the optimized condition involves 50 mM sodium cacodylate pH6.0, 0.5 mM Spermine, 20 mM magnesium acetate, 100 mM sodium chloride, 25% MPD (Fig.3.24). In brief, for the formation of mutant H3.2 nucleosome crystals the following protocol was optimized. Crystals of the purified H3.2 nucleosomes were obtained by the hanging drop vapor diffusion method. The drop included the H3.2 nucleosomes (1 µl) and a solution (1 µl) containing 20 mM potassium cacodylate (pH 6.0), 50 mM KCl, and 75–155 mM $MnCl_2$. The reservoir solution contained 20 mM potassium cacodylate (pH 6.0), 35–40 mM KCl, and 50–80 mM $MnCl_2$. Crystals typically appeared within 10 - 7 days, and grew to their full size over a period of 3 - 2 weeks. Crystals were transferred to 37 mM $MnCl_2$, 40 mM KCl, 20 mM cacodylate, pH 6.0, and 24% 2-methyl-2,4-pentanediol for stabilization and improvement of diffraction resolution. The crystals were small but big enough for the Micro ED (electron diffraction) which is dedicated for the small crystals. Diffraction patterns and conditions are presently being optimized by Dr. Robert Janowski (Structural Biology Unit, HMGU).

Fig.3.23

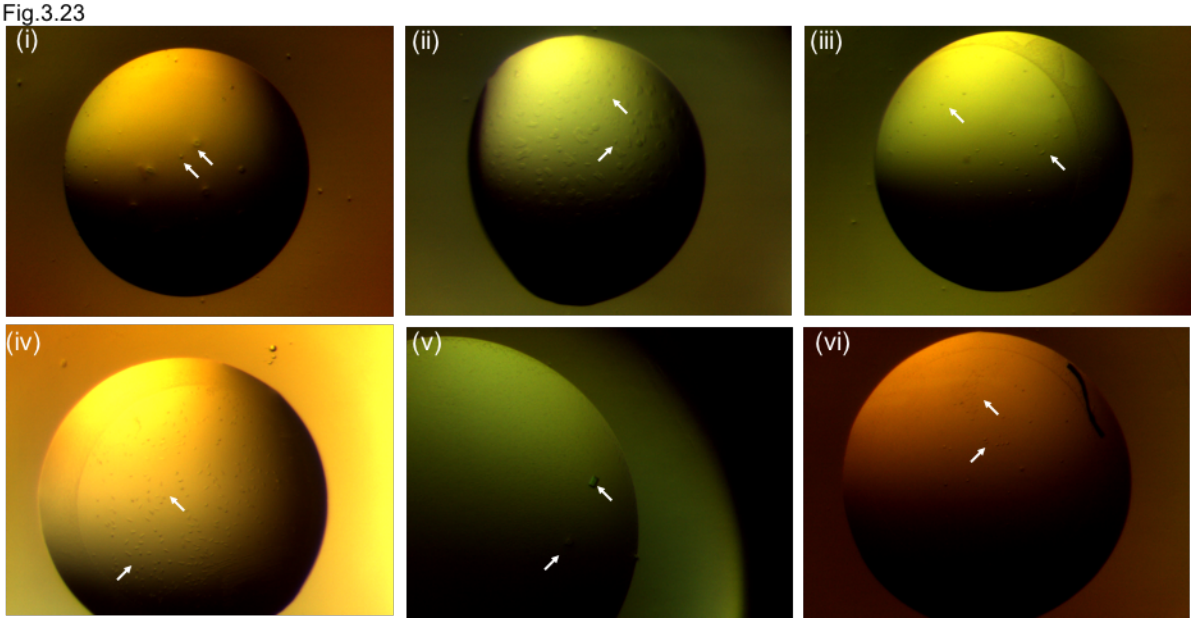

Fig.3.23: **Optimization of crysatllization conditions.**
Crystallization conditions was optimized using different crystallization screens in 96 well plates. The crystals appeared in the following conditions (highlighted by arrows): (i):0.05 M Na cacodylate pH 6.5, 0.08M Mg acetate, 15 % PEG 400 (ii):0.05 M HEPES pH 7.0, 0.1 M KCl, 0.01M $CaCl_2$, 10 % PEG 400. (iii) 0.05 M Na cacodylate pH 6.0, 2.5 mM Spermine, 20 mM $MgCl_2$, 5 % PEG 4000. (iv)0.1 M KCl, 0.01 M $MgCl_2$, 0.05 M MES pH 6.0, 10% PEG 400. (v)0.2 M AmAc, 0.01 M $CaCl_2$, 0.05 M Na cacodylate pH 6.5, 10% PEG 4000. (vi)0.2 M KCl, 0.01 M $MgCl_2$, 0.05 M Na cacodylate pH 6.5, 10% PEG 4000.

Fig.3.24

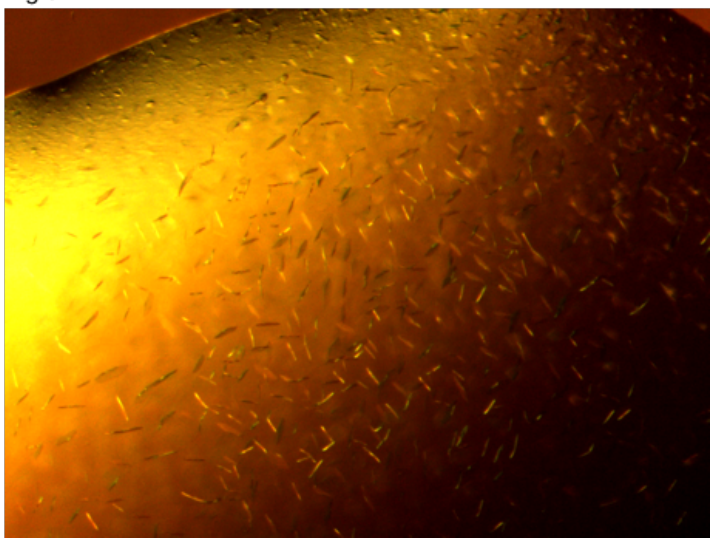

Fig.3.24: **Small crystals under optimized crystal conditions.**

Crystallization of nucleosome was optimized further by manual optimization. Various small crystals were formed. The diffraction obtained with the crystal was 20 Angstorm.

Objective 4: Assessment of the role of *Hist2h3c1* encoded H3.2 in embryonic development.

To identify the key developmental genes regulated by *Hist2h3c1* gene, a transgenic approach was employed. The mutant and the wild-type proteins were designed to be tagged to fluorescent proteins (GFP) to enable analysis of the H3.2 - specific DNA sequences and proteins. The results provided could help in identifying the unique functions of H3.2 in embryonic development.

3.7 Establishment of H3.2-GFP transgenic line

3.7.1 Rational designing of H3.2-GFP fusion protein.

The nucleotide sequence corresponding to the GFP variant - super folder GFP was chosen. The variant exhibits improved folding kinetics and minimal dimerization (Pédelacq et al. 2006). The sequence was codon optimized for mammalian expression (Patterson et al. 2005). 20 nucleotides of the *Hist2h3c1* gene fragment was added upstream of the GFP coding sequence for cloning purposes. Linker sequences comprising of varying lengths of glycine-serine residues represent an important component of GFP fusion proteins. The linker sequences improve protein stability and preserve the intrinsic biological activities of the fusion protein (Chen et al. 2013). Therefore, for efficient assembly of the Histone GFP fusion protein, nucleotide sequence encoding glycine-glycine-glycine-serine linker sequence of 7.6 nm length follows the *Hist2h3c1* coding sequence. Nucleotide sequence corresponding to the restriction enzyme *Age*I and *Afe*I were added upstream and downstream of the stop codon respectively for cloning purposes.

3.7.2 Selection of guides.

The gene of interest *Hist2h3c1*, is present in the histone gene cluster *Hist2* at the genomic sequence NC_000069.6 in chromosome 3. There are genes for 10 core histone proteins present in this 55-kb cluster, namely: three histone H3 genes, four histone H2a genes, one histone H4 gene and two histone H2b genes. There are no histone H1 genes present in this cluster. The three histone H3 genes are identical in their coding sequences and code for the histone H3.2 protein. In addition, the region containing the genes – *Hist2h3c1* and *Hist2h2aa1* appears to have been duplicated and is present as an inverted repeat separated by 5.2 kb (Wang et al. 1996, Fig.3.25). These two regions are highly homologous for a length of 1.8 kb and differ only by 4 nucleotides at the 5’ UTR of the histone H3 genes.

The available regions for positioning of uniques guides targeting *Hist2h3c1* is illustrated in the Fig.3.25. These regions were used for gRNA designing. To reduce off target effects, a dual

gRNA approach was used to cut out the entire *Hist2h3c1* coding region and facilitate knock in of the fusion gene *Hist2h3c1-GFP* by homology directed repair. The top ranked gRNA sequences were selected by the online gRNA Designer (http://www.broadinstitute.org/rnai/public/analysis-tools/sgrna-design) and are given in Table 1. The gRNAs are referred to as 5'gRNA (upstream of the *Hist2h3c1* gene start codon) and 3'gRNA (downstream of the *Hist2h3c1* gene stop codon).

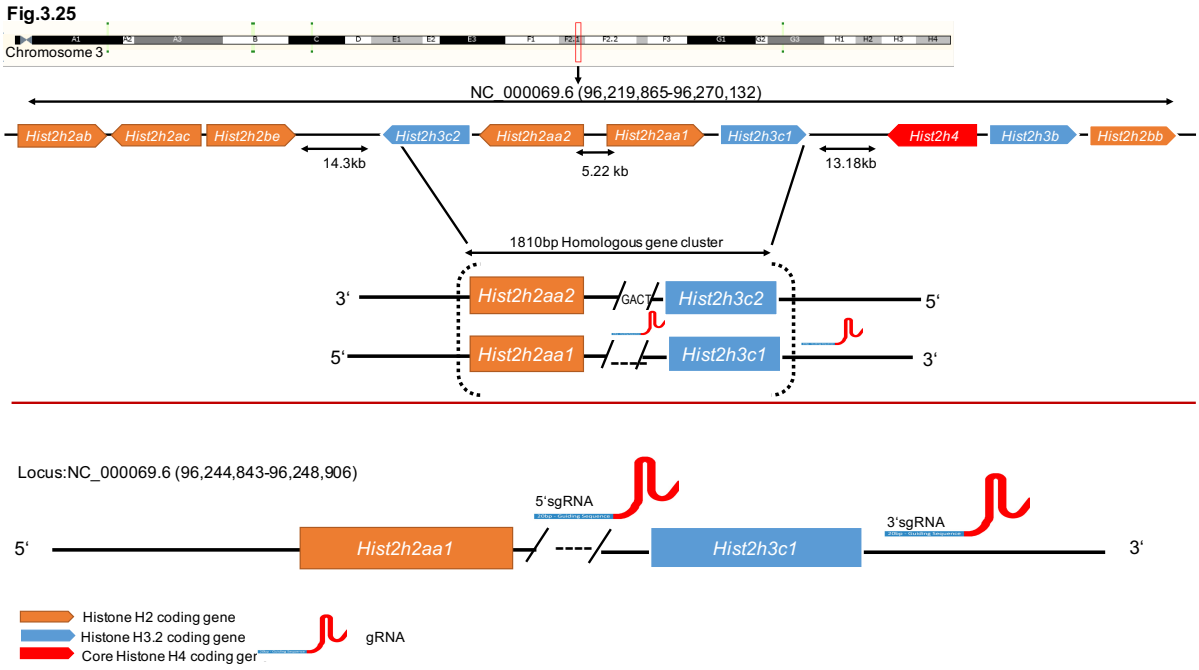

Fig.3.25: **Targeting strategy for *Hist2h3c1* by CRISPR/CAS9.**
The genomic co-ordinates of the *Hist2* cluster is given. The positions of the genes in the cluster are depicted. The genomic region containing *Hist2h3c1* and *Hist2h2aa1* is highly homologous with the region found 5.2kb downstream. The possible positions for the gRNA binding regions upstream and downstream of the gene are given.

3.7.3 *In-vitro* analysis of the target region.

To avoid the presence of any SNPs in the binding region of the guides primer sets were constructed to enable sequence analysis of the required regions. Primers were designed for the *Hist2h3c1* coding region and for regions 1.5 kb upstream as well as downstream of the gRNA sequences (Table 1). No SNPs were found in C57BL6/N genomic DNA at the regions NC_000069.6 (96,244,843-96,248,906). This particular sequence analyzed is henceforth referred to as target sequence. The efficient knock-in of the wild-type and mutant constructs fused in frame to GFP was mediated by the donor plasmid. Since the position of 5'gRNA is

near the coding region of *Hist2h2aa1* (90bps downstream of the coding region), the donor plasmid should encompass the entire *Hist2h2aa1* coding region, to ensure unwanted mutations in the *Hist2h2aa1* gene.

The features of the donor plasmid include

- 5' homology arm (5HA): 1352bp genomic region around the 5'gRNA PAM (also contains coding sequence of H2A)
- 1100 *Hist2h3c1* gene fragment (without the stop codon)
- 829bp *GFP* with stop codon for in-frame translation
- 3' homology arm (3HA): 1623 bp genomic region around the 3'gRNA PAM

The donor plasmids was also constructed to contain base changes in the PAM site to prevent re-cutting by CAS9 after editing (Paix et al. 2017). The NGG PAM sequence of guides was changed using specific primers (Table 3) to NCG, which has the relatively lowest level of CRISPR/Cas9 mediated DNA cleavage (Zhang et al. 2015). The sequence verified 5'gRNA and 3'gRNA plasmids along with the donor plasmids were tested for their *in-vitro* efficacy in N2A cell line. The insertion of the transgene was analyzed by the presence/absence of fluorescence in control and experimental cells. The results of the *in-vitro* analysis are shown in Fig.3.26.

Fig.3.26

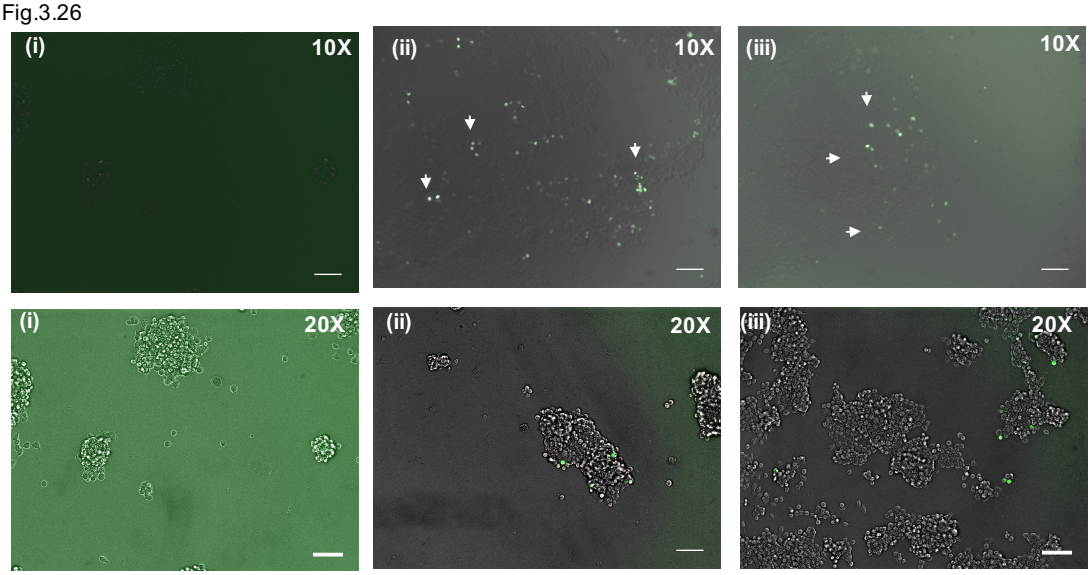

Fig.3.26: **Representative fluorescene microscopy images of the transfected cell lines.**
(i) Negative control: Empty vector
(ii) Vector with guideRNA sequences and wild-type donor plasmid
(iii) Vector with guideRNA sequences and donor plasmid
GFP postive cells were found only in (ii) and (iii) as shown by white arrows. Bars indicate 100 µm in 10X and 75 µm in 20X

3.7.4 Characterization of the transgenic line.

The tested guides and donor plasmids were used for the microinjections along with recombinant CAS9 protein (IDT, Coralville, USA). All the mice obtained from the injections showed normal development and appeared healthy. Genomic DNA was isolated from tail tips of mice and PCR amplification was done for the genotyping. By primers specific for *GFP* and *Hist2h3c1* positive mouse tails were identified. 54 positive founder mice were obtained from 4 separate injections. The selected founder mice were then mated with C57BL6/N mice. Fig.3.27 illustrates the establishment of the transgenic lines from the respective founders. No adverse pathological effect had been observed because of the wild-type and mutant transgene integration. In spite of repeated injections (n=4) only two founder mice were found to be positive for the Ile120Leu mutation and GFP insertion. In addition, the mutation was not consistently carried in the subsequent generations indicating episomal integration followed by loss of the plasmid in subsequent generations.

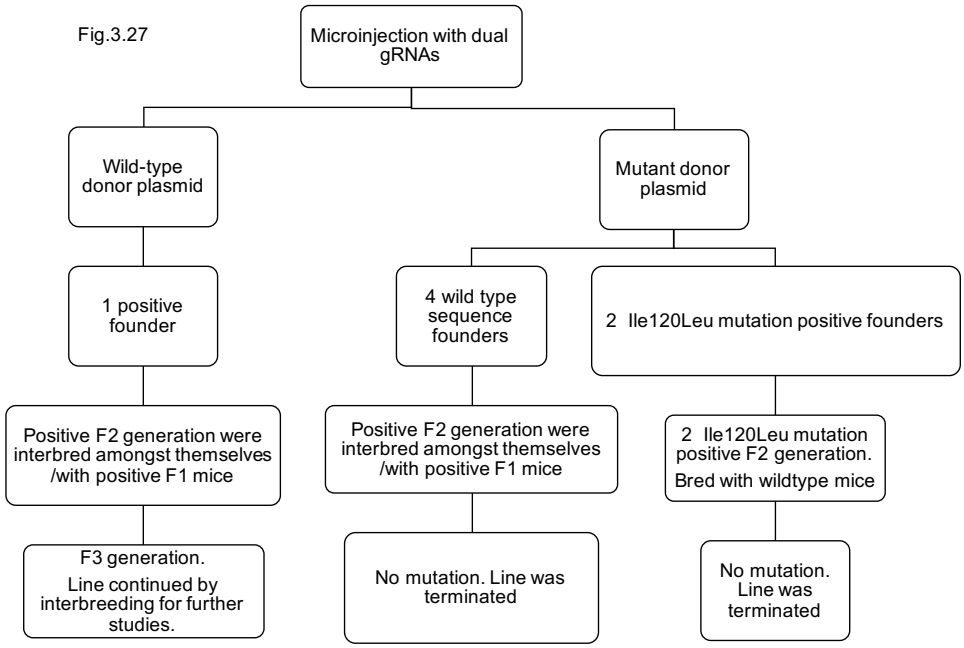

Fig.3.27: **Schematic overview of mice line generated from transgenic targeting of *Hist2h3c1* locus.**

Wild-type and mutant donor plasmid were used for microinjection with dual gRNAs. Positive founder mice were identified by PCR around the targeted region and interbred with wild-type C57BL/6N mice to give F1 generation mice. The positive F1 mice were interbred amongst themselves/with wildtype C57BL/6N mice to increase the breeding colony for subsequent line generation.

Unlike the mutant *Hist2h3c1* line, wild-type *Hist2h3c1* line was quite stable and the presence of *Hist2h3c1+GFP* sequence in genotyping PCR was consistently observed. However, the

genomic integration of the transgene in the correct locus was difficult to analyze using PCR. This could be either due to the complex nature of the histone-rich target locus or could be that the transgene is not integrated in the correct locus. An indirect approach was undertaken to assess whether the transgene has integrated into the correct locus (n=4 genomic DNA samples). The inserted transgene contains a mutated PAM (NGG>NCG) at the 5' and 3' end to prevent re-cutting by CAS9. Therefore, PCR around the mutated PAM site with primer sets inside the target region should give a sequence with the mutation. Primer sets with one of the primers binding outside of the target region and the other primer amplifying the PAM site would give wild-type/heterozygous sequence. The PCR reactions and the subsequent sequencing showed that the entire transgene had not been integrated in the correct locus (Fig.3.28).

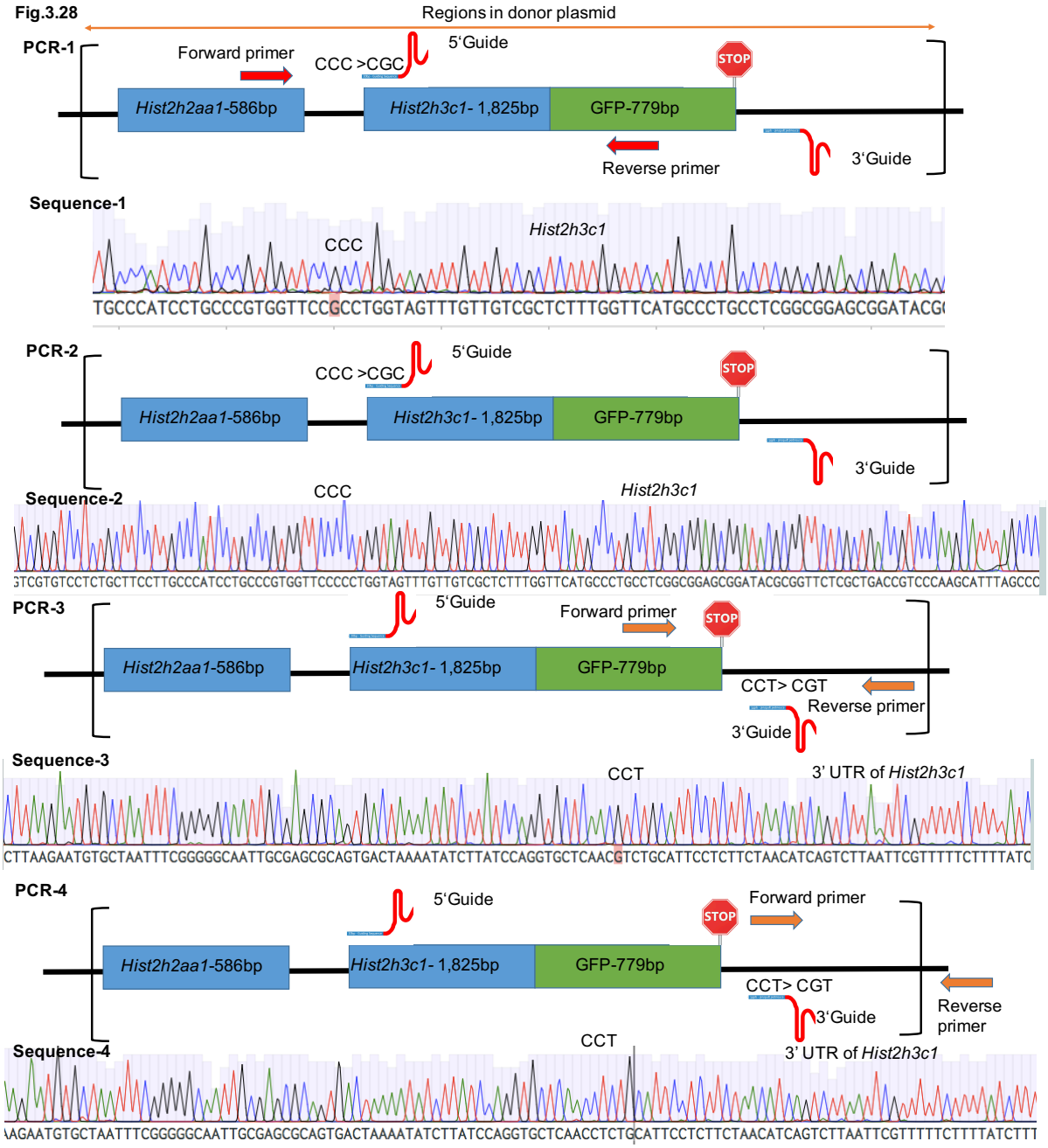

Fig.3.28: **Representative PCR schema and the sequences for PAM mutations**.

PCR-1: Primers span 5'PAM mutation site and GFP.
Sequence-1: Mutation in 5'PAM mutation site is detected.
PCR-2: Primers span 5'PAM mutation site and region upstream of donor plasmid.
Sequence-2: Wild type sequence was detected.
PCR-3: Primers span 3'PAM mutation site and GFP.
Sequence-3: Mutation in 3'PAM mutation site is detected.

3.8 Functional analysis of Histone H3.2WT-GFP fusion protein

To identify whether transgenic expression of *Hist2h3c1* is leading to transcriptional differences in H3.2 coding genes, QPCR analyses of the different H3.2 coding genes in *Hist2* cluster was done at E10.5 (Fig.3.29). No significant differences in the expression levels of the H3.2 genes were found between the transgenic lines and the wild-type line (C57BL6/N).

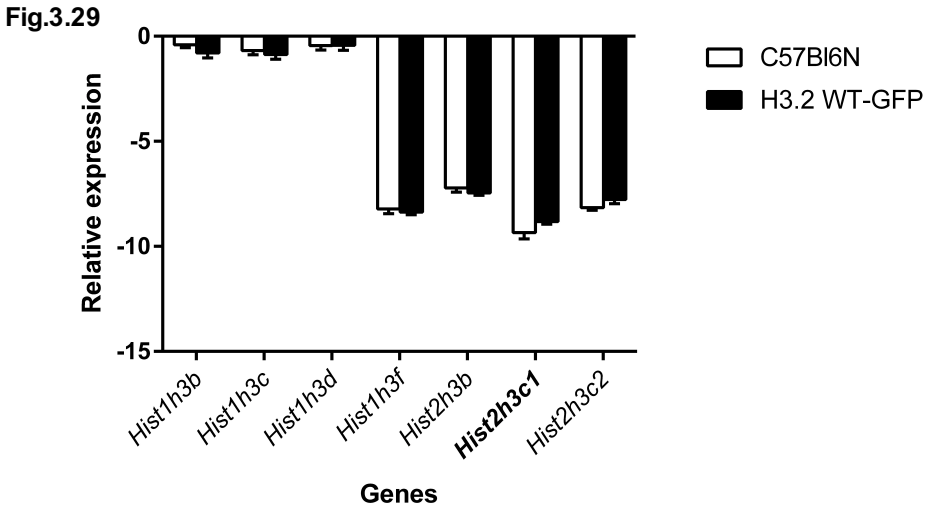

Fig. 3.29: **QPCR analysis of Hist2 cluster H3.2 coding genes**

Relative expression levels of histone genes in the embryonic heads of wildtype C57BL6/N mice and H3.2WT-GFP mice (E10.5). *Rplp0* was taken as the housekeeping gene, and analysis was done using the relative expression method. Values are given as relative expression levels ± SEM; n=4 for each tissue type. No alteration in the pattern of expression were found amongst the genes analyzed.

To look whether the fusion protein has been formed appropriately, western blotting and CoIP were done in the embryonic tissues using a GFP antibody. The blot from both the experiments indicate that the fusion protein (H3.2WT-GFP) is formed in the mouse line (Fig.3.30A&B). In addition, imaging of the embryonic fibroblasts culture indicate that the H3.2WT-GFP is functional and is found in the derived fibroblast cells of the embryo (Fig.3.31). Localization analysis was done in the embryonic tissue sections for GFP fluorescence. The GFP positive cells co-staining with DAPI-stained nuclei were found dispersed throughout the embryonic tissues, including developing optic vesicle (Fig.3.31).

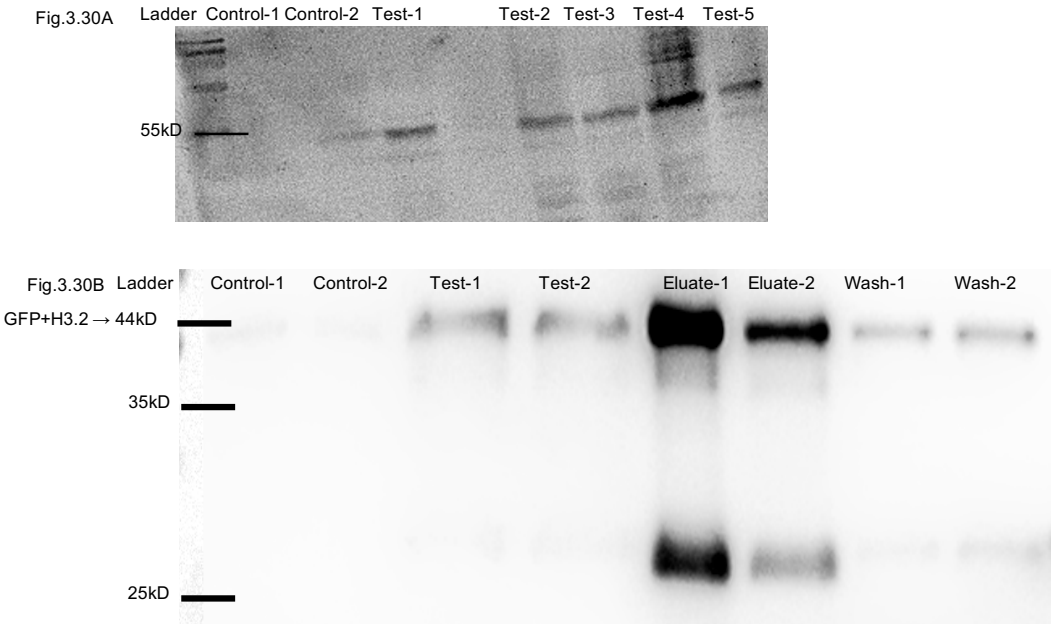

Fig.3.30: **Characterization of fusion protein H3.2WT-GFP. A)** Western blot was done in the protein extracted from the embryos of H3.2WT-GFP mouse line (Test) using GFP antibody. Wild type C57BL6/N embryos were used as control. H3.2-GFP fusion protein positive bands were found in the test (GFP → 27 KDa, H3 → 17 KDa, GFP+H3.2 → 44kD). **B)** Coimmunoprecipitation of embryonic head tissues from control & H3.2WT-GFP mouse line with GFP antibody. In case of test samples higher molecular weight H3.2 WT-GFP fusion protein band were detected in the eluates as well as the washes from co-immunoprecipitation.

Fig.3.31

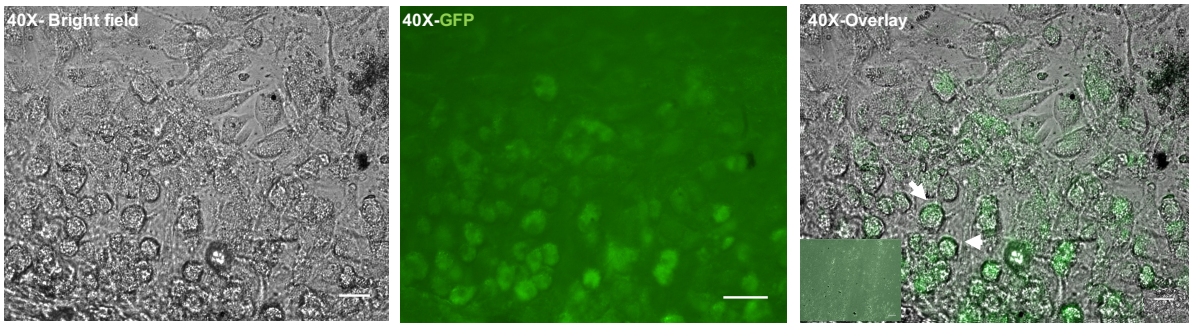

Fig.3.31: **Representative fluorescence microscopy images of embryonic fibroblasts.**

There is presence of GFP positive cells in cells derived from H3.2 WT-GFP embryos (E10.5), in comparison to the negative control of wild-type embryonic fibroblasts, shown in the inset. The overlay of GFP image with the corresponding bright field image indicates the presence of GFP in the rounded cells of the fibroblasts culture (highlighted by white arrows). Bars indicate 50 μm.

Fig.3.32

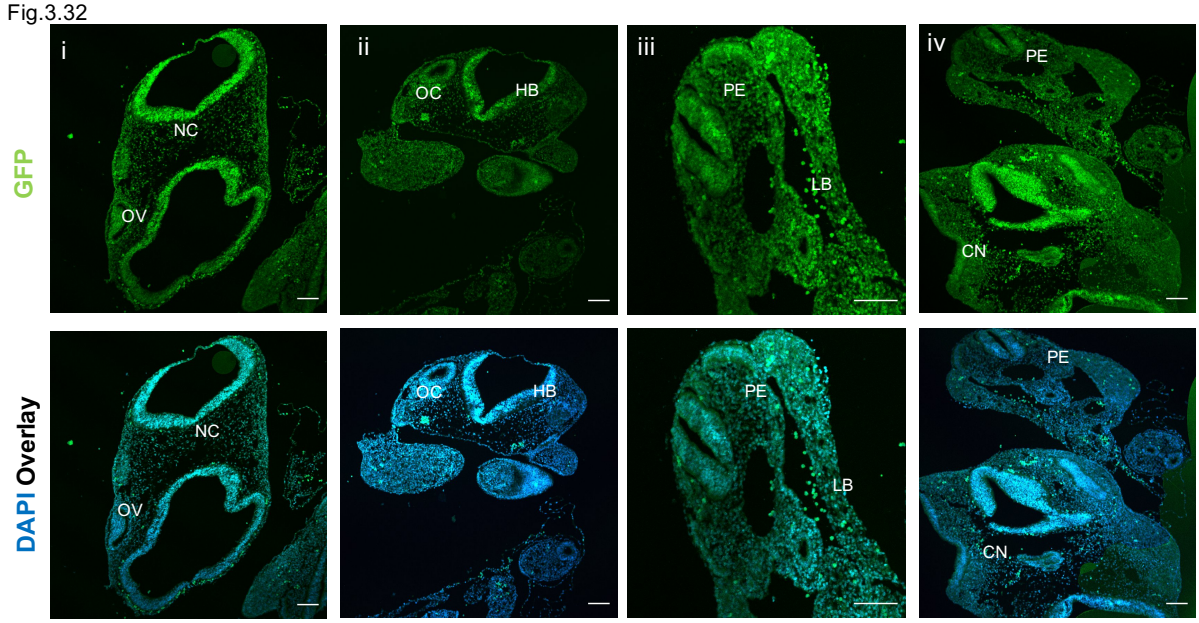

Fig.3.32: **Distribution of H3.2WT–GFP in sagittal sections of embryonic tissues.**

Diverse embryonic tissues were imaged at E10.5 for GFP fluorescence. Homogenous distribution of H3.2WT-GFP was found throughout the developing tissues (i-iv). Overlay with DAPI is also shown. The bars indicate 100 µm; NC, Neural Crest; OV, Optic Vescicle; HB, Hind Brain; OC, Otocyst PE, Pharyngeal Endoderm; LB; Limb Bud; CN; Caudal Neurophore.

3.9 Characterization of incorporation sites of *Hist2h3c1* encoded H3.2

ChIP-seq could help in identifying the H3.2 incorporation sites through specific enrichment using anti-GFP antibody in transgene positive embryonic tissues. 4 embryonic heads were pooled together and used for preparation of ChIP DNA and subsequent sequencing. More than 35 million reads were obtained for ChIP DNA and the associated input control. Peaks were called with a q value cut off of 5.00e-02 (adjusted p-values found using an optimised FDR approach; Wang et al. 2015). Highest distribution of H3.2-GFP peaks were found in chromosome 2, while lowest distribution were found in sex chromosomes X and Y. Also, the distribution of the H3.2-GFP peaks across various chromosomes is also given in Fig.3.33. Fold enrichment was calculated for the H3.2-GFP peaks by using the input control DNA for background subtraction. The top enriched were found in the intronic region of the genes: *F13a1, Shisa6, Epha3, Il15ra, Sdccag8, Dpp10*. The enriched gene co-ordinates along with their fold enrichment is given in Table 12.

Fig.3.33

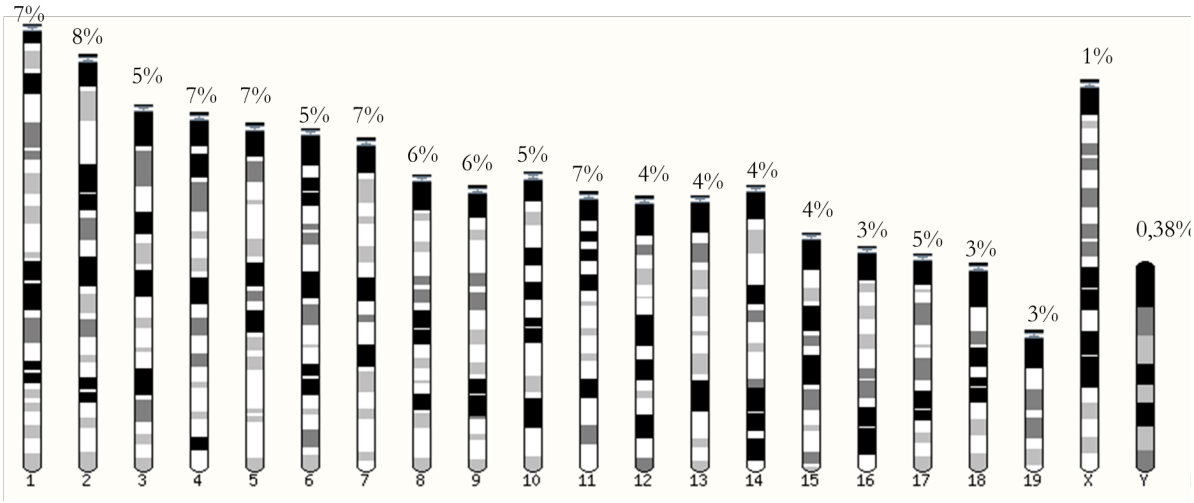

Fig.3.33: **Representation of H3.2WT-GFP binding sites across the different chromosomes.**

The graphic ideogram of different mouse chromosomes was taken from ENSEMBL (Zerbino et al.,2018). The chromosome specific binding sites were evaluated by calculating the proportion of peaks detected on each chromosome category by MACS software.

Table 12: **Top enriched genes bound by H3.2WT-GFP at E10.5.**

F13a1	blood coagulation, cytokine-mediated signaling pathway, platelet degranulation.	14.15773	Chr13: 36978295-36978985
Shisa6	neurotransmission, Wnt/β-Catenin signaling in development, regulation of short-term neuronal synaptic plasticity.	12.42411	Chr11: 66420882-66421325
Epha3	cellular response to retinoic acid, ephrin receptor signaling, regulation of epithelial to mesenchymal transition.	12.391	Chr16: 63833434-63833836
Car1	neuron projection development , natural killer cell differentiation, positive regulation of phagocytosis.	12.44904	Chr3: 14669654-14670023
Sdccag8	establishment of cell polarity, microtubule organizing center organization, neuron migration.	10.77189	Chr1: 176899515-176899933
Dpp10	positive regulation of protein localization to plasma membrane, regulation of potassium ion transmembrane transport.	10.23329	Chr1: 123820227-123820731
Bmp4	eye morphogenesis, neural tube closure, epithelial to mesenchymal cell proliferation	5.92454	Chr14: 46384122-46384627
Tsc1	neural tube closure, myelination, glucose import, hippocampus development.	5.92454	Chr2: 28675848-28676354

Further, to confirm that the transgenic insertion of H3.2-GFP does not affect the transcriptional expression of the bound genes, the expression levels of the top enriched genes were analyzed in H3.2-GFP and wild-type embryos. The relative expression levels of the genes given in Fig.3.34 indicate transcriptionally repressed levels of the bound gene. The relative expression levels were similar in both the lines. Interestingly, none of the major developmental factors like *Pax6*, *Sox2* and *Pitx3* were amongst the top enriched genes. Other ocular importance genes were found to be bound by H3.2-GFP across their promoters, intronic and exonic regions including *Cryaa* and *Bmp4* (Fig.3.35).

Fig.3.34

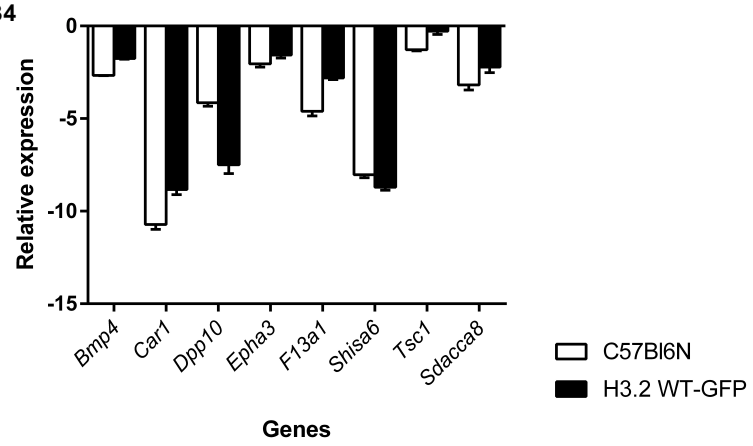

Fig. 3.34: **QPCR analysis of top enriched genes from H3.2WT-GFP**

Relative expression levels of the top ChIP Seq enriched genes in the embryonic heads of wildtype C57BL6/N mice and H3.2WT-GFP mice (E10.5). *B2m* was taken as the housekeeping gene, and analysis was done using the relative expression method. Values are given as relative expression levels ± SEM; n=4 for each tissue type. No significant alteration in the pattern of expression were found amongst the genes analyzed.

Fig.3.35

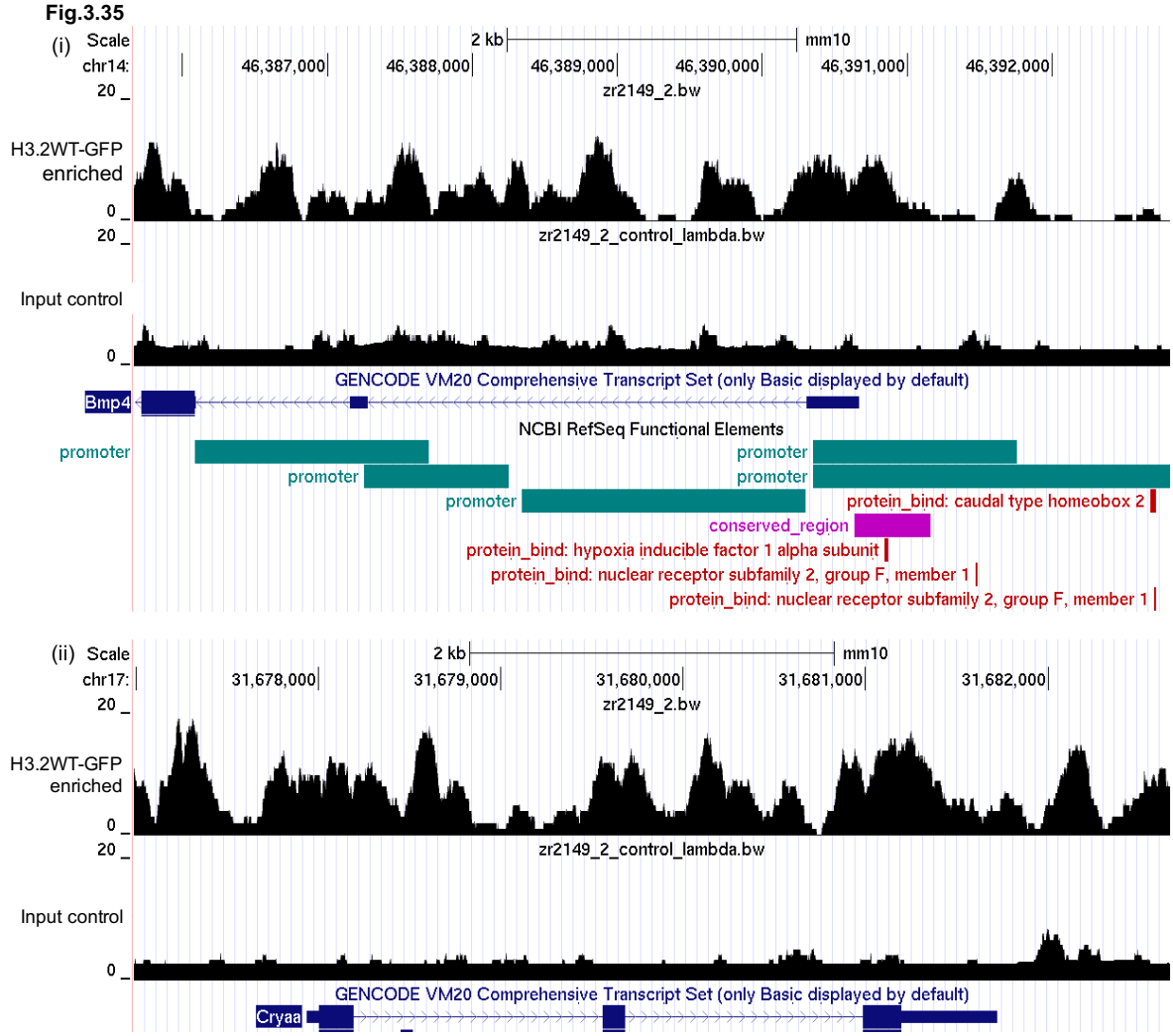

Fig.3.35: **Genomic distribution of H3.2-GFP binding peaks over *Bmp4* (i) and *Cryaa* (ii).**

The track files generated from sequencing of H3.2-GFP ChIP DNA and sequencing of input control (no antibody) were used. The peaks represent the binding sites of the fusion protein to be distributed throughout the *Bmp4* & *Cryaa* genomic region. Enriched peaks are also found in the promoter region of *Bmp4* responsible for tissue specific expression.

3.10 Characterization of H3.2 regulated genes in *Aey69*

Gene identifiers from H3.2WT-GFP ChIP-seq were matched to the gene identifiers from the microarray data in *Aey69* (E10.5). Almost 68 percentage of the genes were found to be shared between microarray and ChIP-seq. Amongst the 26517 genes analyzed by microarray, only 8573 genes were not found to be enriched by H3.2WT-GFP (32%). The incorporation of H3.2WT-GFP on the majority of the altered genes from *Aey69* microarray could indicate direct or indirect regulation of H3.2WT-GFP on the respectively bound genes. To analyze this, homozygous H3.2WT-GFP female mice were bred with homozygous *Aey69* male mice and

the resulting heterozygous embryos were also sent for ChIP-seq. For the ChIP-seq from Aey69 x H3.2WT-GFP line the signals were considerably less intense across the various genes.

Genome-wide peak calling by MACS indicated that only 348 peaks were detected in Aey69 x H3.2 WT-GFP embryos as opposed to 584724 peaks in H3.2 WT-GFP ChIP-seq. Heat maps for the average ChIP-Seq signals of H3.2WT-GFP in H3.2WT-GFP and Aey69 x H3.2WT-GFP were generated across the genomic regions of various genes. Comparison of th heat map indictes a dramatic loss of H3.2WT-GFP incorporation across the various regions (Fig.3.36). This could indicate a loss/reduction of wild-type H3.2 incorporation sites in *Aey69* mutant at E10.5. This loss could be speculated to be responsible for the transcriptomic alterations documented by *Aey69* microarray at E10.5.

The top enriched genes from the Aey69 x H3.2 WT-GFP Chip-Seq are given in Table 13. None of the top enriched genes from H3.2-GFP line were found in Aey69 x H3.2 WT-GFP ChIP-Seq. Interestingly, Ephrin ligand *Efna5* was one of the most enriched gene in the Aey69 x H3.2 WT-GFP Chip-seq. While, Ephrin receptors *Epha3* and *Ephb2* were some of the most enriched genes in H3.2 WT-GFP Chip-seq. The track files from the ChIP-seqs indicate the H3.2 incorporation pattern to be drastically altered in the mutant for the Ephrin ligand and its receptors (Fig.3.37).

Table 13**: Top enriched genes bound by H3.2WT-GFP at E10.5 in the embryos from Aey69xH3.2WT-GFP.**

Gene	Biological function	Fold Enrichment	Region
Dpp9	aminopeptidase activity, serine-type peptidase activity	35.20163	Chr17: 56200008-56200089
Myo7a	visual perception, inner ear development, lysosome organization, mechanoreceptor differentiation.	20.04537	Chr7: 98060025-98060094
Cntnap5c	development of peripheral and central nervous system, cell adhesion, intercellular communication.	17.74423	Chr17:57855968-57856020
Hdac9	negative regulation of striated muscle tissue development, histone H3 deacetylation, cholesterol homeostasis.	18.3249	Chr12: 34073758-34073812
Efna5	ephrin receptor signaling pathway, regulation of insulin secretion in cellular response to glucose stimulus, retinal ganglion cell axon guidance.	16.57919	Chr17: 62737574-62737625

Fig.3.36

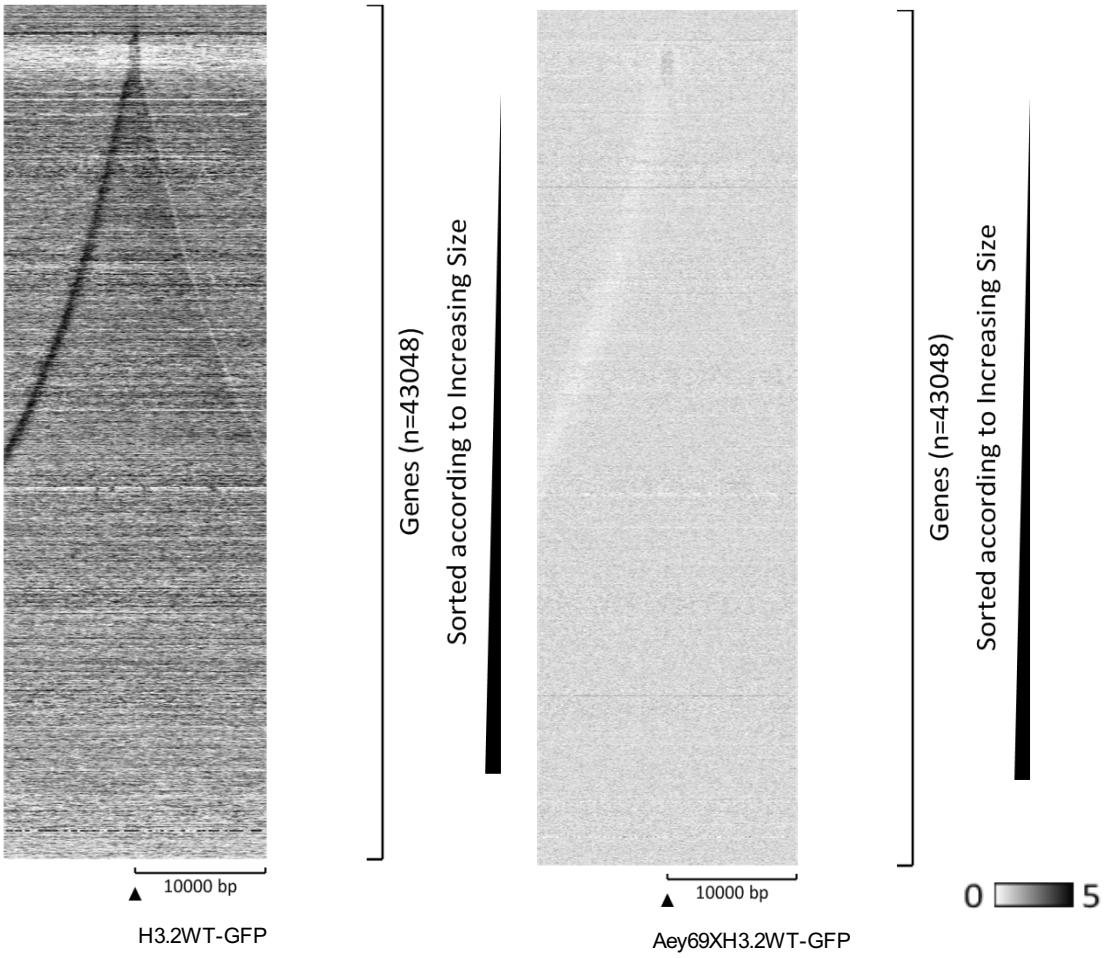

Fig.3.36: **Heat Map of H3.2-WTGFP ChIP-seq signals.**

Genomic regions corresponding to various annotated genes were extracted from the 'Mouse genomic DNA_mm10' dataset and was segmented into 200 bins. BedGraph files from the ChIP-Seq data were used. Average signal of the respective ChIP-seq read counts normalized to the corresponding total number of reads (counts per million reads) were plotted against the the genomic regions. The bar shows the relationship between coloring and signal intensity. Data were generated using EaSeq. Decrease in signal intensity of H3.2WT-GFP was found in the embryos from Aey69x H3.2 WT-GFP mouse line.

Fig.3.37

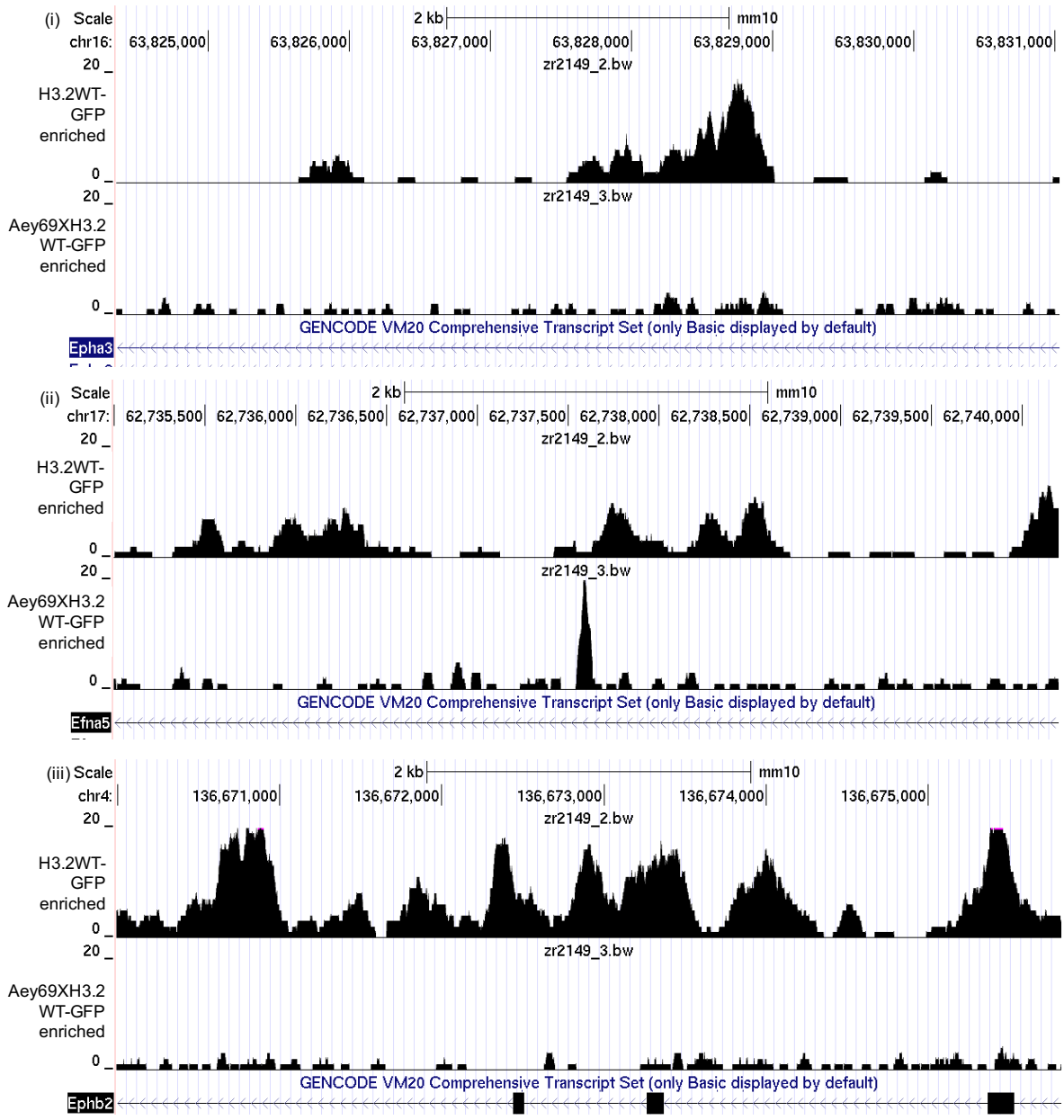

Fig.3.37: **Genomic distribution of H3.2-GFP binding peaks over *Epha3* (i), *Efna5* (ii) and *Ephb2* (iii).**

The track files were generated from the sequencing of embryos from H3.2WT-GFP and Aey69XH3.2 WT-GFP mice. The peaks indicate the binding sites of the fusion protein to be comparatively more enriched in the embryos from H3.2WT-GFP. Consequently, the binding is dramatically reduced in the embryos obtained from Aey69XH3.2 WT-GFP mice.

To validate the ChIP-Seq results, ChIP-qPCR was performed on two independent ChIP samples (n=8 embryos). The ChIP-qPCR values were in general agreement with the ChIP-Seq results. In brief, the top eight enriched regions from H3.2WT-GFP ChIP-Seq were chosen and analyzed by ChIP-QPCR (Fig.3.38). All the regions were found to show significant

enrichment respective to their enrichment in ChIP-Seq. Also no/less enrichment was found in Aey69 x H3.2 WT-GFP embryos. Interestingly, difference in the enrichment values were found in the head and body regions in both the H3.2 WT-GFP and Aey69 x H3.2 WT-GFP embryos. This could indicate an incorporation of H3.2 in specific genomic areas in a region specific manner (head vs body). In particular, for *Bmp4* broad enrichment of H3.2-GFP at tissue specific promoter regions shown by ChIP-Seq (Fig.3.35) and ChIP-QPCR further corroborates this hypothesis.

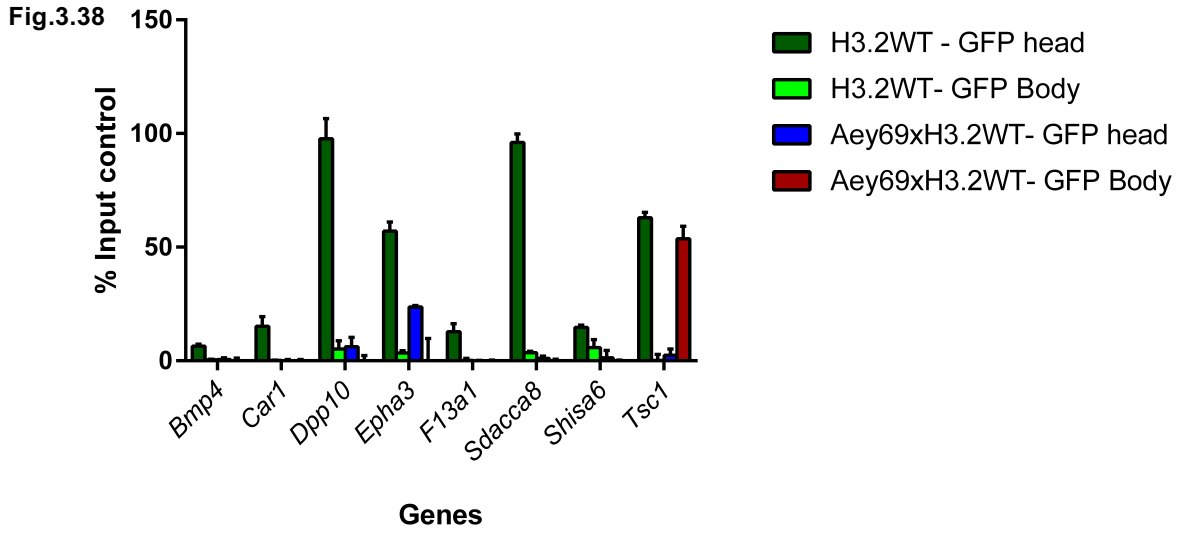

Fig.3.38: **ChIP-QPCR analysis of top enriched genes**.

The top enriched genes from H3.2WT-GFP ChIP Seq were analyzed in the embryonic tissues of the H3.2-WT GFP and Aey69xH3.2-WT GFP. E10.5 stage was chosen and 4 embryonic heads/bodies were pooled together. Values are represented as Mean±SD. The experiment was technically and biologically repeated. Enrichment was found in the head tissues of H3.2WT-GFP embryos. Enrichment of the genes were found to be reduced in the Aey69xH3.2-WT GFP embryos. Lesser enrichment was found in the body of the respective embryos. Enrichment was calculated by percentage input control method.

Amongst the enriched genes by H3.2-GFP in H3.2 WT-GFP and Aey69 x H3.2 WT-GFP embryos Ephrin family had genes of ocular developmental importance in both the ChIP-Seqs (Table 12 and Table 13). Therefore, Ephrin signaling mediated by EPHB2 and EFNA5 in early ocular differentiation (Noh et al.2016) were chosen for a closer look for any possible alteration in *Aey69*. For the same immunohistochemical distribution of Ephrin receptor EPHB2 and Ephrin ligand EFNA5 was done from E11.5 - E13.5 when the ocular pathology onsets and the results are given in Fig.3.39. The images show clearly altered Ephrin signaling in the mutant eyes from the pathological stage of E11.5.

EPHB2 was found to label across the membranes of the wild-type in lens and retina. Strong expression of its ligand EFNA5 is found with a very strong expression in the lens placode at E11.5. Compared to the wild-type, no strong expression of EFNA5 is found in the mutant lens and retina across the stages. There does seem to be an expression of EPHB2 across the membranes of the mutant lens and retina but its expression seems to be much weaker at E11.5 and is dramatically lost at the preceding stages. Cumulatively, it could be hypothesized that the loss of effective localization of the proteins has led to ineffective closure of the Ephrin signaling mediated optic fissure closure in *Aey69*. Of note, since the proteins represent one of the highly enriched genes in the ChIP-seqs, their effect could be speculated to be directly mediated by *Hist2h3c1* encoded H3.2.

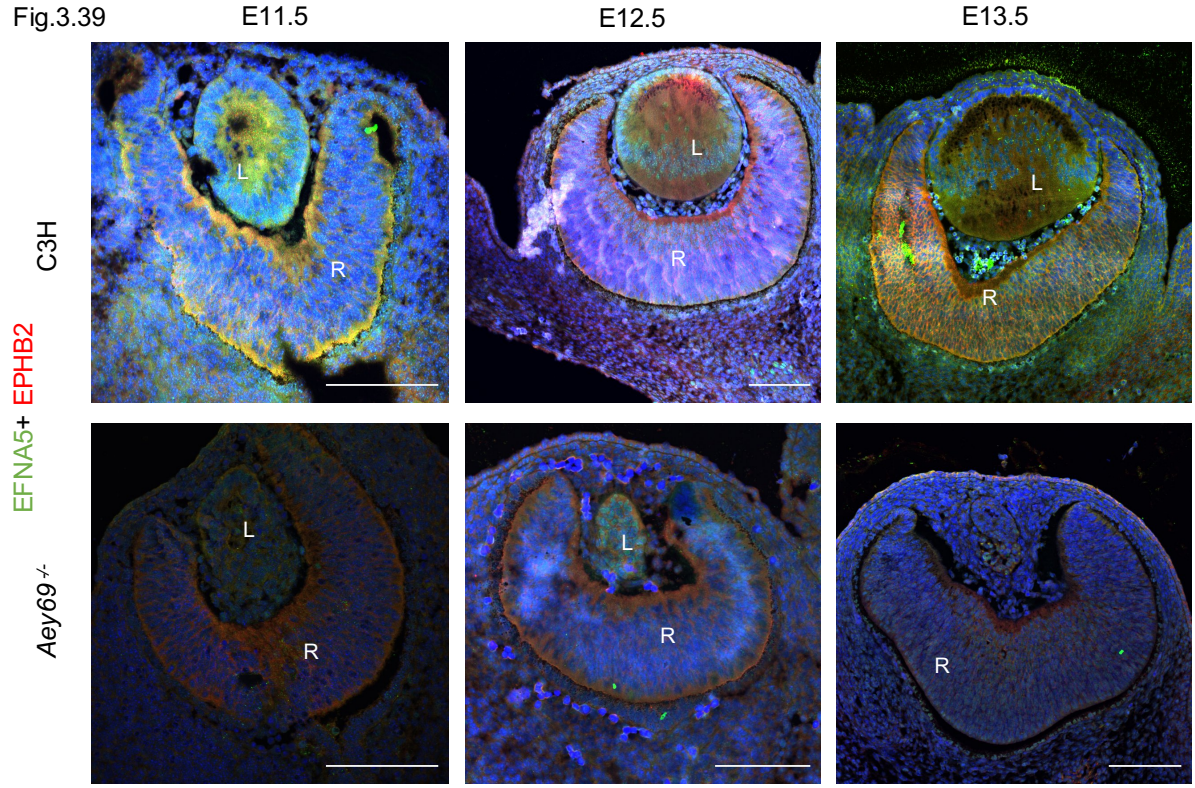

Fig.3.39: **Ephrin Signaling in *Aey69***

The EPHB2 receptor and its ligand EFNA5 to characterize the Ephrin signaling from the stages of E11.5-E13.5. From E11.5 reduced expression of EPHB2 was found in the mutant eyes. The bars indicate 100 µm; n=2 for each embryonic stage; L, lens; R, retina; ON, optic nerve.

4 Discussion

The doctoral thesis is focused on two diverse topics:

Pathophysiological changes in *Aey69*

The earliest hint for the ocular specification in the mouse happens at around E8.5 through the evagination of the diencephalon to form the optic vesicle. Subsequently, the lens vesicle is established at E11.5 following separation from the surface ectoderm (Smith et al. 2009). In *Aey69* this separation is altered leading to a 'no lens' pathology with overgrown retina at P7 (Fig. 1.2).

From the histological analyses, several questions arose:

- What is the nature of the lens vesicle in the *Aey69* mutants?
- Are there any changes in the development of the mutant retina and if so when do they start? Do all retinal cell types contribute to the retinal overgrowth?
- And how do the known ocular developmental factors contribute to the phenotype?

These questions are discussed in the first part of the discussion.

Role of *Hist2h3c1* in eye development through *Aey69* and H3.2WT-GFP

Aey69 represents a unique mouse model with two point mutations in two diverse genes: a gap junction mediating intercellular communication (*Gja8*) and a histone gene providing structural and regulatory components for epigenetic regulation (*Hist2h3c1*). The *Gja8* mutation in this mutant line (71T->C; Val24Ala) affects the first transmembrane domain. Point mutations in *Gja8* have been reported in sites preceding this amino acid position and domain, namely G22R in *Lop10* mouse (Runge et al. 1992) and R23T (human; Alapure et al. 2012). Both mutant forms are associated with a cataractous phenotype and smaller lenses (but not with no lens phenotype as in *Aey69*). In *Aey69*, the phenotype is much stronger and starts much earlier than the reported *Gja8* mutations. In addition, even in the similar phenotype, *aphakia*, GJA8 remains present in the mutant lens at E12.5, but it is localized differently in the *Aey69* mutants (Fig. 3.9). This led me to conclude that the primary role behind the *Aey69* phenotype is the *Hist2h3c1*. In addition, collaborative efforts in zebrafish by Dr.Natascia Tiso, Padova, Italy corroborated the primary role of *Hist2h3c1* in *Aey69* ocular pathology (Vetrivel et al. 2019). So, the second part of the discussion will focus on the nature of the *Hist2h3c1* mutation and the role of its encoded protein in eye development.

4.1 Lens apoptosis and retinal hyperproliferation leading to microphthalmia

Microphthalmic mouse models like *aphakia*, *Sey* (Yamada et al. 2003; Ahmad N et al. 2013) have been largely focussed on the defective lens development. However, herein I present the earliest evidence and time course of both lens and retinal alterations in the microphthalmic mouse model of *Aey69*.To get a brief overview of the disrupted events the mutant retina and lens development were characterized from the stage of pathological surface ectoderm connection at E11.5. For the mutant lenses, it is clear that cells expressing lens-specific factors namely, CRYAA, AP2α, PITX3 and FOXE3 (Fig.3.1 and Fig.3.2) were found until the stage of E14.5. However, there is a failure of lens fiber cell differentiation. Specifically, AP2α, PITX3, FOXE3 indicate the possible presence of lens epithelial cells that undergo proliferation. This speculation is corroborated by the presence of KI67-stained cells in the mutant lens (Fig.3.6A). However, this expression is not sufficient for successful lens differentiation. Rather we see a misshapen lens whose area of the lens specific factors is decreasing in the consequent stages through apoptosis (Fig.3.2).

On the other hand, the immunohistochemical characterization of the retina through E11.5-E15.5 suggested a different story. In the wild type, retinal ganglion cells (RGC) are generated first, followed by cone photoreceptors and horizontal cells. After birth, bipolar cells and Müller glia are specified and complete differentiation (Zagozewski et al. 2014). In *Aey69*, there is an early appearance and over expression of BRN3 - positive and OTX2 - positive RPC cell types in the mutant retina (Fig.3.3). This earlier expression of retinal cell types is accompanied by a strong retinal proliferation as seen by KI67 staining at E15.5 (Fig.3.6A). It might be speculated to have spearheaded the growth of an almost tumorigenic retina filling up the empty lens region (Fig. 1.2). Thus, we see that the failed surface ectoderm separation has a pathological effect on both, the lens and the retina, from E11.5.

One of the important aspects uncovered from the study involves the documentation of the earliest lens and retinal changes through CLEAVED CASPASE 3 + AP-2α and BRN3 immunostainings respectively following persistent surface ectoderm connection (E11.5). The study also provided evidence that all the important retinal cells are present in *Aey69* after birth (P7) despite the early retinal alterations. *Pitx3* mutant mouse lines which have been characterized extensively also show defective surface ectoderm (Ahmad N et al. 2013; Rosemann et al. 2010). Therefore, I analyzed these important aspects (BRN3 staining and retinal cells at P7) in *Pitx3* mouse line. In addition, since *Aey69* is a dominant mouse line, I investigated the aspects in Aey69$^{+/-}$ embryos also to provide evidence on the dominant nature of the *Hist2h3c1* mutant phenotype in heterozygous condition.

There is an earlier appearance of BRN3 - positive RPCs in both the *aphakia* and *Aey69*$^{+/-}$ embryos (Fig.3.4A). The loss of lens through apoptosis is illustrated through Cleaved caspase 3 and AP2α decreased expression in the mutant lenses of both *aphakia* mutant and *Aey69*$^{+/-}$ heterozygous embryos (Fig.3.4B). In addition, the persistence of AP2α positive cells in the mutant cornea indicate that the loss of a lens protein does not affect the expression of the protein in other ocular compartments. Also collapse of retinal architecture involving all the cells of the retina is also found in the mutant eyes analyzed (Fig.4.2C). The results clearly indicate the existence of early retinal alterations in the mutant mice with ocular pathology on setting from persistent surface ectoderm connection. Thus despite the absence of histological features of retinal alteration in embryonic changes, BRN3 staining clearly indicate that retinal development is altered when lens development is altered. This holds promising endeavors for the identification of shared molecular signatures orchestrating ocular changes in microphthalmic mice. For the same, BRN3 could be used as an indicator in diverse microphthalmic mouse models including *Pax6* small eye mutants (Hill et al. 1991) and *Foxe3* mutant mice *dyl* (dysgenetic lens; Blixt et al. 2000). Such a comparative analysis of coordinated lens and retinal development could help in the establishment of a pathophysiological timeline in the microphthalmic mouse models.

Fig.4.1

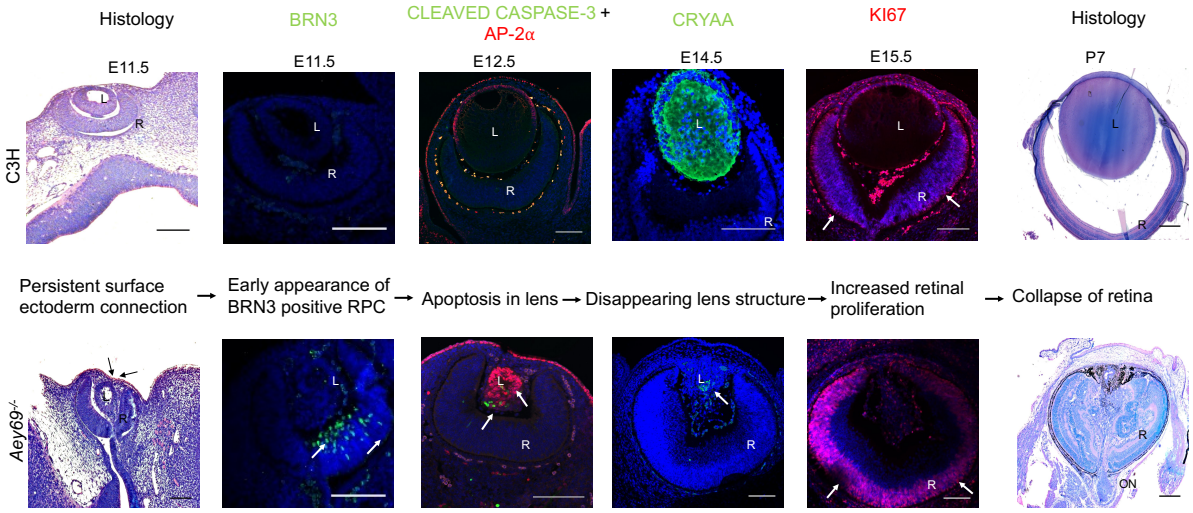

Fig.4.1: **Summary and representative timeline of micropthalmic pathology**

Earliest pathology of micropthalmia is evident from the histological observation of persistent surface ectoderm at E11.5. Concurrently, there is an early appearance of RPCs, followed by apoptotic events in lens leading to a dying lens structure. Increased proliferation events onset in retina, finally followed by filling up of the 'empty lens' region with retinal cells.

4.2 Altered molecules in *Aey69*

The pathology of microphthalmia in *Aey69* begins at embryonic stage of E11.5 similar to the *aphakia* mutant mice, when the mutant lens vesicle does not separate properly from the surface ectoderm (Fig.1.2). In *aphakia* mice, PITX3 deficiency has been found to cause this pathology (Rieger et al. 2001; Semina et al. 2000). However, in the early stages of *Aey69* development, the expression of PITX3 is maintained and therefore not responsible for the failed surface ectoderm separation (Fig.3.1). Interestingly, without any clear alteration of PITX3 at E11.5, decrease in expression was found for its downstream regulator factors namely FOXE3 and PROX1 (Blixt et al. 2000; Wigle and Oliver 1999). The effect of this alteration is more severe for FOXE3 which is found to be decreasing more in the mutant lens from E11.5 compared to CRYAA and PITX3 (Fig.3.1, Fig.3.2 and Fig.3.4). For the identification of alternative pathways regulating FOXE3 transcriptomic data from microarray could provide a vital clue.

An alternative pathway regulating FOXE3 could be *Bmpr1a*, one of the top altered genes at E9.5 from microarray. *Bmpr1a* along with its ligands *Bmp4* and *Bmp7* regulate multiple aspects of lens development via a Smad - dependent pathway for lens cells survival (Kahata et al. 2018). Lens formation and the expression of FOXE3 and CRYAA were found to be altered and reduced in *Bmpr1a* conditional knockout mice (Rajagopal et al. 2009). Additionally, disruptions of the dorsal–ventral gradient of BMP signaling in the optic cup results in failure to close the optic fissure (Huang et al. 2015). Therefore, the events of persistent surface ectoderm connection observed from E10.5 could be a consequence of these disrupted signaling. In particular, expression of the ligands, *Bmp4* and *Bmp7* needs to be negatively auto-regulated in the lens-forming ectoderm, decreasing when the tissue is exposed to exogenous BMPs, and increasing when BMP signaling is prevented. However, in the mutant mice this decrease is not found and the factors are found to show an inconsistent expression pattern with downregulation at E10.5, 12.5 and upregulation at E11.5 (Fig.3.8).

Other molecules showing similar expression trend were *Creb1* and its related molecules (Bleckmann et al. 2002). *Creb1* was predicted as the upstream regulator for the transcriptional changes at E9.5 by IPA analysis. CREB1- dependent transcriptional regulation of *Cryaa* promoter through chromatin remodeling enzymes (BRG1), PAX6 and high levels of histone H3 K9 acetylation has been well documented from E11.5 (Yang et al. 2006). Incidentally, CREB has been reported to act in concert with BMPR1A and BMP4 during hematopoietic stem cell differentiation in embryonic development (Kim et al. 2015). Thus, the microarray based expression analysis at E9.5 pointed to a dysregulated pathway involving *Creb1* and

Bmpr1a. The effect of this dysregulation is also seen by the prediction of upstream regulator at E10.5, *Vax2*. *Vax2* is a homeobox gene, responsible for establishment of a proper dorsoventral eye axis and has been reported to be regulated by BMP signaling.

Therefore, taken together the gene expression analyses could point to transcriptional differences in various interconnected key molecules of ocular development. In addition, though these molecules may be postulated to have important roles in ocular development at early embryonic stage of E9.5-E12.5, none of the mice models of these factors develop microphthalmia (Table 11). Instead, they develop specific alterations in lens and retina like misrouting of optic fibres, coloboma, defective lens fibre cells differentiation, attesting to their specific contribution to ocular differentiation at a specific time point. Moreover, alteration in these factors happen without any major changes in the immunohistochemical distributions of the primary ocular development factors, PAX6 and SOX2 (Richter-Kügler Master's thesis 2013, Cvekl and Ashery-Padan 2014).

The identification of the potential causative factors of microphthalmia in *Aey69* lead to the next line of investigation – how is *Hist2h3c1* primarily responsible for Aey69 ocular pathology? And, how does it act?

4.3 *Hist2h3c1* encoded H3.2 is responsible for the *Aey69* pathology

Hist2h3c1 encoded canonical variant H3.2 is synthesized in a replication-dependent manner and has been found to occupy heterochromatic sites in mouse embryos throughout the preimplantation stage, i.e. from the one-cell stage through the blastocyst stage. This expression is a prerequisite to achieve the epigenetic reprogramming required for development (Akiyama et al. 2011). Apart from this observation, no specific role is known about *Hist2h3c1* and its encoded protein during development and in different tissues. There is high nucleotide conservation amongst the genes encoding for H3.2. Therefore, highly specific primer sequences were used to analyze the expression of the histone cluster genes in different tissues and across different embryonic stages. *Hist2h3c1* was found to be the most highly expressed histone H3.2 genes in the lens as compared to the other analyzed tissues like retina, brain and liver (Fig.3.10A). In addition, the gene was found to be down-regulated in the embryonic stages of the homozygous *Aey69* mutants (Fig.3.10B). Therefore, it could be hypothesized that the *Hist2h3c1* has an indispensable role in ocular development because of its increased expression in the adult wild-type lenses and differential expression at the stages of E10.5-E12.5 in the mutant embryos when microphthalmia begins.

Initially, I hypothesized that the mutation could have created new miRNA binding sites in *Hist2h3c1* mRNA and the miRNA-mRNA combination could have led to the perturbations in *Aey69*. However, none of the miRNA analyzed were found to show the upregulation expression pattern in the analyzed embryonic stages (Fig.3.16). In addition, an analysis of miRNA dependent regulation of histone mRNA processing found polyadenylation of the histone mRNA to be one of the primary factors influencing the interactions (Sinkkonen 2008). In contrast, to other conventional mRNAs replication dependent histones include H3.2 encoding mRNA are produced with a stem-loop in the 3′-end of the RNA structure (Marzluff et al. 2002). Thus, the developmental disturbances in *Aey69* is more likely to be coordinated by histone protein than histone mRNA.

For *Hist2h3c1* encoded H3.2, there have been no characterized missense mutants so far. In addition, the Ile120 position has been conserved in all the histone variants in the mammalian species (Hake and Allis 2006). Therefore, I hypothesized a conserved role for this particular amino acid position. *in-silico* analyses of the wild-type and mutant proteins suggested structural divergence and altered nucleosome-DNA contacts (Fig.3.17). The altered DNA-Histone contacts in *Aey69* could have led to mutated subpopulation of H3.2 proteins that interferes with the normal functions of the wild-type H3.2 via a dominant-negative mechanism. A similar dominant-negative mode of action has been documented with H3.3D123N mutant in zebrafish model of altered craniofacial development (Cox et al. 2012). In the model, D123N mutation was shown to result in a dominant H3.3 mutants with defective H3.3 nucleosomes incorporation at certain genomic sites. Interestingly, indirect evidence of defective nucleosomes incorporation was observed in *Aey69* through upregulation of various nucleosome remodeling factors at E10.5-E12.5 (Fig.3.18) and in altered immune histochemical distribution of SMARCA4 in ocular sections at E10.5-E12.5 (Fig.3.19).

To test the hypothesis of dominant-negative action of mutant H3.2, I looked at the functional alterations of histone H3.2 in *Aey69*. There is no specific antibody available to detect only H3.2 protein, therefore, established Histone H3 PTMs were analyzed to indirectly assess any change in the H3.2 protein function in *Aey69* (Richter-Kügler Master's thesis 2013). Changes in the mitotic marker H3S10P was the predominant alteration observed (Fig.3.13). Phosphorylation of histone H3 fulfills multiple roles: chromosomes condensation and segregation during mitosis and gene expression modulation in a context-dependent manner (Sawicka and Seiser 2012). In *Aey69*, there is an increase in H3S10P stained cells, particularly a significant increase of H3S10P aberrant cells across the embryonic stages. Similar H3S10P aberrant cells were found to limit the mitotic progression in the RPCs of developing retina (Ribas et al. 2012). Moreover, mitotic defects characterized by KI67 and PROX1 (Fig.3.6)

were speculated to spearhead the retinal hyperproliferation in *Aey69* (Vetrivel et al.2019). In addition, the apoptosis of the mutant lens was speculated to arise from the cells stalled at G0 and thereby undergo apoptosis (Vetrivel et al.2019). Thus, it could be considered that the ocular pathological changes observed in *Aey69* are the result of altered H3S10P distribution. Concurrently, alteration in H3S10 phosphorylation have been observed in mutated version of H3.2 in nucleosomes of mouse zygote (Lan et al. 2017). Thus, it could be speculated that the mutant H3.2 interferes with the normal functions of the wild-type H3.2 particularly, those related to H3S10P, thereby being the primary motivating force behind the mitotic defects in *Aey69*. To elaborate on the dominant negative action of H3.2 mutants, I, then tried to identify the specific regions marked by the histone H3.2 and whether the region is differentially marked by the mutant histone in *Aey69*.

4.4 Primary characterization of Histone H3.2 during embryonic development.

To know more about the specific genomic regions marked by the histone H3.2 during embryonic development transgenic mice harboring wild-type and mutant H3.2 gene fused to GFP were planned. The Hist2 cluster bearing the target *Hist2h3c1* gene was found to be complex sequence wise (GC rich regions, AT hairpin loops). Particularly, the regions bearing *Hist2h3c1* and *Hist2h3c2* are almost 99% identical (Fig.3.25). This highly homologous nature made any kind of transgene approach difficult. This could be speculated to be the reason for the predominant episomal inheritance of the mutant histone H3.2 fused to GFP, however technical difficulties of CRISPR/CAS9 cannot be ruled out. Conventionally, single point mutations are known to be better introduced with the help of single guide RNA and an oligonucleotide donor (Prykhozhij et al.2018). However, due to the nature of the histone gene cluster, dual guide RNA approach with a donor plasmid was employed. Thus possible technical/biological difficulties associated with CRISPR gene editing in *Hist2h3c1* genomic locus prevented the generation of transgenic mouse line with mutant *Hist2h3c1* fused to GFP. The speculation of a complex genomic locus is further strengthened by previous transgenic experiments to obtain deletion/knockout *Hist2h3c1* mouse lines with similar developmental defects using CRISPR (Ortiz, Unpublished data) and TALENs (Kumar Panda Ph.D. thesis 2014).

Providentially, transgenic line bearing wild-type *Hist2h3c1* sequence fused to GFP could be generated. However, the targeting could not be accomplished at the right locus. The canonical variant H3.2 has been found to occupy heterochromatin sites in mouse embryos throughout the preimplantation stage, i.e., from the one-cell stage through the blastocyst stage (Akiyama et al. 2011). It is then presumed to be replaced by the replacement variant H3.3 during

development. Apart from this, no specific information is known about the function/incorporation sites of the protein during embryonic development to the best of my knowledge. Thus, despite the fact that the *Hist2h3c1-GFP* transgene is not integrated in the right locus, analysis of the intact fusion protein during development would give insights into the incorporation sites/functional properties of H3.2. Interestingly, no adverse transcriptional changes were found in the expression of other Histone H3.2 genes due to the random integration of an extra copy of *Hist2h3c1* gene (Fig.3.29). In addition, the expression of H3.2-GFP as a fusion protein was verified by western blot (Fig.3.30) and the functionality of the fusion protein was further characterized by GFP localization analyses in tissue sections and embryonic fibroblasts culture (Fig.3.31 and Fig.3.32). Interestingly a typical whole embryo distribution of the histone variant was found (Fig.3.32).

For identifying key players related to ocular development heads of E10.5 embryos were pooled and used for ChIP-seq. Chromosome 2 was found to have a higher percentage of H3.2 incorporation sites compared to other chromosomes (Fig.3.33). In an analysis of polygenic forms of obesity amongst inbred mouse strains (I129P3/J (129) and C57BL/6ByJ (B6)) Significant linkages were found for body weight and body length on Chr 2 (Reed et al. 2003). In the phenotypic screen from GMC *Aey69* mice were found to have increased body temperature, less body mass and reduced blood lipid values. The genetic nature behind this phenotype could be explained by altered incorporation of Histone H3.2 to possible key molecules in Chromosome 2. While the least preference for the sex chromosomes X and Y could be explained by the presence of specific histone variant H3t for these chromosomes (Boggs et al. 1996; Hoyer-Fender 2003)

4.5 Ocular development through Histone H3.2

Interestingly, higher fold enrichment was not found for well-studied microphthalmia-related genes, namely *Pax6*, *Sox2*, *Pitx3*, *Foxe3* (Table 12). This is in agreement with the observance of absence of gene expression of these genes in the *Aey69* microarray dataset. However, higher enrichment were found for other genes of ocular importance namely, *Shisa6* and *Epha3*. Amongst the genes broadly encompassed by H3.2, enrichment at promoters, intergenic and exonic region of *Cryaa*, lens specific marker was also found. CRYAA was characterized by IHC to be gradually lost in *Aey69* mutant eyes during embryonic development. Epigenetic regulation for enhanced activation of *Cryaa* promoter during lens differentiation by histone PTM and chromatin remodeling has been established earlier (Yang et al. 2006). Broad enrichment of H3.2 could add another regulation level to this epigenetic

process. Possible ineffective incorporation of H3.2 at *Cryaa* locus in *Aey69* could have led to disruption of the *Cryaa* activation and thereby stimulating its loss in the subsequent stages.

To test the hypothesis of ineffective incorporation of wild-type Histone H3.2 in Aey69, wtH3.2-GFP mice were crossed with dominant *Aey69* mice. ChIP-seq of the embryos from these cross bred mice revealed loss of enrichment of the bound regions in *Aey69* x wtH3.2-GFP corroborating our hypothesis (Fig.3.36). Similar reduction in ChIP-seq signals have been found in Histone H3 point mutations containing mouse ES cells (Fang et al. 2018; Voon et al. 2018). Though the antibodies used in the study do not discriminate between the various histone variants the effect on individual wild-type histone variant incorporation sites cannot be ruled out. Thus the observation of altered incorporation sites reiterates the findings from similar point mutant studies and also adds additional information regarding the effect of point mutant H3.2Ile120Leu effect on its wild-type counterpart. Concurrently altered histone subtype incorporation were found to have diverse transcriptional effects on the bound genes (Harada et al. 2018; Larson et al. 2019). Thus altered incorporation of wtH3.2-GFP in *Aey69* could also possibly explain the altered gene levels found in *Aey69* microarray analysis.

Validation of the ChIP-seq results by ChIP-QPCR again found loss of enrichment in *Aey69* x wtH3.2-GFP (Fig.3.38). Moreover, the incorporation of wtH3.2-GFP was found to be head region specific as no/less enrichment was found in the body regions of both the wild-type and mutant embryos. Thus despite its whole embryo distribution *Hist2h3c1* encoded H3.2 was found to have region specific function (Fig.3.38). In addition, comprehensive QPCR analysis of selected genes from microarray included top enriched genes found in ChIP-seq (*Epha3*, *Efna5*). Thus it could be speculated that insufficient incorporation of wtH3.2 could have directly lead to the expression changes in the observed genes. Incidentally, transcriptional changes have also been found in a H3.3 mutant with relation to skeletal muscle development (Harada et al. 2018). The non-uniformity in gene expression across development was characterized as a rate change of gene expression regulated by the histone variant through RNA-seq and ChIP-seq. The study further went on to show that the specific presence of a variant is required for transcriptional activation of genes in an organ specific manner.

To further elaborate the disrupted role of H3.2 in *Aey69* ocular development, candidate molecules were shortlisted based on microarray and ChIP-seq. Amongst the shortlisted molecules, Ephrin signaling based on the receptor *Efhb2* and the ligand *Efna5* from ChIP-seq were analyzed in depth by immunohistochemistry (Fig.3.39). Reduced expression of the ligand EFNA5 was found in the mutant ocular sections from E11.5-E13.5. The altered expression of the Ephrin molecules through ineffective wtH3.2 incorporations could potentially

be the primary factor behind the microphthalmic *Aey69* pathology. In embryonic ocular sections, binding of EphB2 to Ephrin A5 was found to induce a sustained activation of JNK (Jun N-terminal kinases). The prolonged JNK signal was found to be important for controlled cell proliferation and apoptosis (Noh et al. 2016). Thus, the altered proliferation and apoptotic events in *Aey69* could have resulted from the altered EFNA5 and EPHB2 distribution, triggered by ineffective wtH3.2 incorporation. The ineffective incorporation could also be speculated to manifest in the H3S10P aberrant distribution in Aey69 embryonic sections. Concurrently, altered H3S10P aberrant cells were identified in Ephrin-regulated cell cycle arrest, in the RPCs of developing retina (Ribas et al.2012). Taken together it could be postulated that the mutant histone H3.2 leads to widespread mitotic and gene transcriptional changes in *Aey69* and these changes have orchestrated the microphthalmic pathology primarily, through Ephrin signaling.

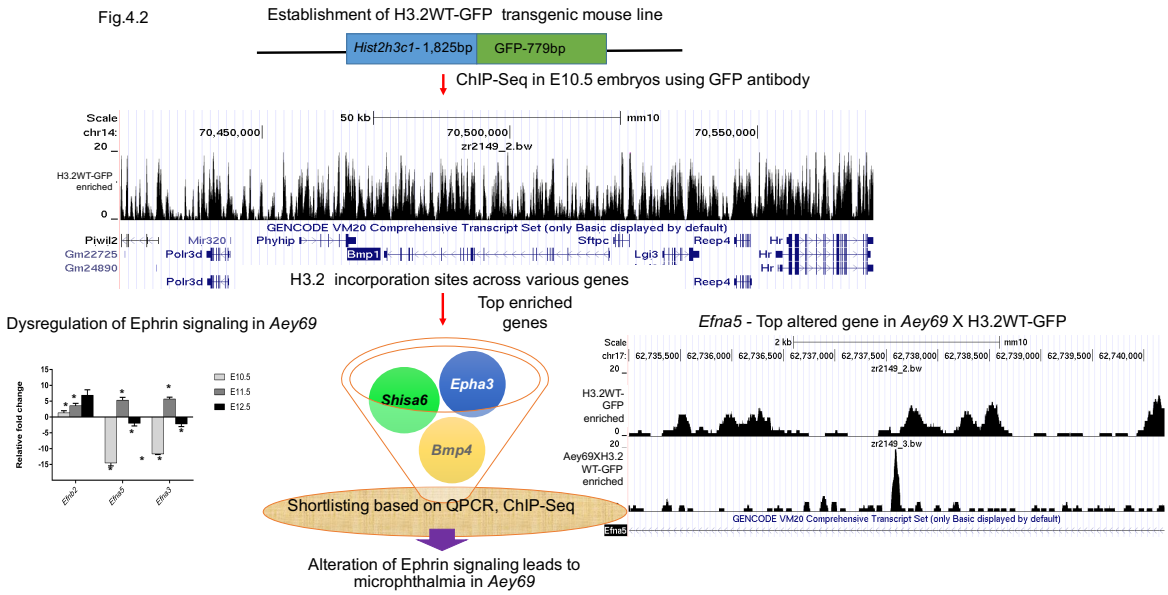

Fig.4.2: **Schematic overview for the identification of candidate molecules for *Aey69* microphthalmia through H3.2WT-GFP.**
The transgenic mouse line H3.2WT-GFP was established and characterized. Heads of the transgenic embryos (n=4) at E10.5 were used for ChIP-Seq. Track files obtained from the ChIP-Seq showed incorporation of H3.2WT-GFP across various genes. The top enriched genes included – *Ephb2* and *Epha3* of the Ephrin family. In addition, Ephrin family genes were found to be significantly altered by QPCR in *Aey69* during the pathological stages of E10-E12.5. Moreover, the transgenic line was crossed with the homozygous *Aey69* mutants and the resulting embryos were sent for ChIP-Seq to analyze their incorporation in the mutant. ChIP-Seq revealed drastic reduction in enrichment across various genes including *Efna5* of the Ephrin family. Based on these, *Efna5* (ligand) and *Ephb2* (receptor) were chosen and found to be altered in *Aey69.* Thus, the candidate molecules primarily responsible for the *Aey69* pathology were identified.

4.6 Conclusion

The association of H3.2 protein with transcriptionally inactive genes in mouse embryos (2-cell stage) has already been characterized (Akiyama et al. 2011). The presence of H3.2 at these genes had been originally interpreted as a pointer for heterochromatin until its replacement by H3.3. But herein, I observed the binding sites and regions of H3.2 have diverse effects – region specific function, direction of transcriptional regulation (down and up regulation) and disruption of downstream epigenetic processes. In conclusion, it could be said that Histone H3.2 binds and regulates various unique developmental factors. By affecting these multiple regulators, the mutant histone H3.2 in Aey69 seems to have created a restrictive environment for ocular differentiation in *Aey69*.

5 Future prospects.

5.1 Pleiotrophic effects in *Aey69*

Aey69 mice display additional impairments in other organs and systems including reduced fat content, hyperactivity and increased body temperature. Organ specific analyses related to these phenotypic changes have been limited till now to dopaminergic, noradrenergic and serotonergic neurons in the substantia nigra, innervating striatum and locus coeruleus of The adult *Aey69* brain. The quantitative analyses did not reveal any drastic changes and also the sample size was limited (Hladik Bachelor Thesis 2013). To competently rule out the involvement of the central nervous system in the *Aey69* hyperactivity increased sample size and analyses of the monoaminergic and cholinergic neurons needs to be done. Another alternative facet for the observed reduced fat content, hyperactivity and increased body temperature could be the metabolic functions of the liver. Therefore, in-depth molecular analyses of liver dependent changes is required. Interestingly, *Clpx* and *Pcsk2*, which were amongst the top enriched genes have diverse metabolic functions. Analyses of these genes in the liver system could be an ideal starting point. Finally, there was an observance of delayed vaginal plug in 40% of the *Aey69* mutant mice. For the same, quantitative documentation of any delayed circadian rhythm changes is required. This could help in defining biological basis for the pathology.

5.2 Single cell transcriptomics in eye development

The study presents a descriptive account of the role of H3.2 in eye patterning and promises an additional candidate for syndromic cases of ocular developmental changes. However, in depth analysis of its ocular specific effect requires single cell transcriptomic analysis of the H3.2WT-GFP and Aey69xH3.2WT-GFP. Single cell transcriptomic analysis could also help in defining the molecular basis for biphasic expression pattern observed in microarray data. In addition, a dorsal-ventral gradient has been found to be essential for the Efna5 mediated optic fissure closure at E11.5 (Noh et al. 2016). Consequently, *Efna5* has been shown to show dysregulated levels in terms of mRNA and immunohistochemistry in *Aey69*. Therefore, single cell transcriptomic analyses could provide more interesting cues behind the establishment of such a gradient. Such single cell transcriptomic analyses have been done for characterizing the abundance of extensive splicing alterations in lens development (Srivastava et al. 2017). Since intergenes represents a major genomic category bound by H3.2 the side-by-side analyses of ChIP-seq and single cell RNA-seq data could help in further delineating the

possible role of histone H3.2 in controlling lens development through controlling specific gene transcripts.

5.3 Post translational modifications of H3.2 and H3.2 interacting proteins

The reported mutation is at 120 amino acid position in the L2 loop of H3.2 The loop region forms one of the components in mediating DNA-histone interaction, nucleosomal mobility and stability (Tropberger and Schneider 2010). Also posttranslational modifications have been observed in the preceding amino acids, namely H3K115 and H3K122 acetylation, H3T118 phosphorylation, H3K122 succinylation *in-vivo*. These amino acids have been reported to have a functional role. Particularly acetylated H3K122 has been found to be enriched at active regulatory regions such as proximal promoters and enhancers, suggesting a role of this acetylation in regulating gene expression. The transcriptional stimulation by acetylated H3K122 happens through its ability to promote histone eviction and nucleosome disassembly (Kebede et al. 2014; Tropberger and Schneider 2010). Mass spectrometric quantification of H3.2-GFP associated PTMs in H3.2-WTGFP mice could provide clues to the existence/ non-existence of these PTMs in H3.2. Also comparative analysis of the identified H3.2 specific PTMs in H3.2-WTGFP and Aey69xH3.2WT-GFP Would help in the identification of novel PTMs in tissue specific epigenetics. Further, for tying together the observed H3S10P changes with the mutant Histone H3.2 quantitative mass spectrometric quantification of the Histone PTMs could be the ideal step.

Finally, chaperones have been shown to bind to the histones through residues located at the lateral surface of the nucleosome and particularly in the dyad region comprising H3K115, H3T118 and H3K122. For example ASF1 is a highly conserved histone H3/H4 chaperone that synergizes with two other histone chaperones-chromatin assembly factor 1 (CAF-1) and histone repression A factor (HIRA), in DNA synthesis-coupled and DNA synthesis-independent nucleosome assembly. Arginines at position 128,129, and 134 of H3 have been shown to participate in both electrostatic and hydrophobic interactions with ASF1 (Galvani et al. 2008). Such histone-chaperone interactions have been shown to modulate nucleosome assembly, disassembly or reassembly. Therefore, pull down assays using reported H3 interactions in H3.2-WTGFP mice could help in possible identification of H3.2 specific chaperones.

Thus, the characterized H3.2 transgenic mouse line would help in defining specific characteristics of H3.2 and contribute immensely to the growing field of histone variant specific epigenetic regulation.

6 References:

Acharya D, Nera B, Milstone ZJ, Bourke L, Yoon Y, Rivera-Pérez JA, Trivedi CM, Fazzio TG. TIP55, a splice isoform of the KAT5 acetyltransferase, is essential for developmental gene regulation and organogenesis. Sci Rep. 2018; 8(1):14908.

Adler R, Canto-Soler MV. Molecular mechanisms of optic vesicle development: complexities, ambiguities and controversies. Dev Biol. 2007;305(1):1-13.

Ahmad N, Aslam M, Muenster D, Horsch M, Khan MA, Carlsson P, Beckers J, Graw J. Pitx3 directly regulates Foxe3 during early lens development. Int J Dev Biol. 2013;57(9-10):741-51.

Akiyama T, Suzuki O, Matsuda J, Aoki F. Dynamic replacement of histone H3 variants reprograms epigenetic marks in early mouse embryos. PLoS Genet. 2011;7(10):e1002279.

Alapure BV, Stull JK, Firtina Z, Duncan MK. The unfolded protein response is activated in connexin 50 mutant mouse lenses. Exp Eye Res. 2012; 102:28-37.

Alkozi HA, Franco R, Pintor JJ. Epigenetics in the Eye: An Overview of the Most Relevant Ocular Diseases. Front Genet. 2017; 8:144.

Allfrey Vg, Faulkner R, Mirsky Ae. Acetylation and methylation of histones and their possible role in the regulation of RNA synthesis. Proc Natl Acad Sci U S A. 1964; 51:786-94.

Arnheiter H. The discovery of the microphthalmia locus and its gene, Mitf. Pigment Cell Melanoma Res. 2010;23(6):729-35.

Autiero I, Costantini S, Colonna G. Human sirt-1: molecular modeling and structure-function relationships of an unordered protein. PLoS One. 2008;4(10):e7350.

Baird PN, Guymer RH, Chiu D, Vincent AL, Alexander WS, Foote SJ, Hilton DJ. Generating mouse models of retinal disease using ENU mutagenesis. Vision Res. 2002;42(4):479-85.

Banday AR, Baumgartner M, Al Seesi S, Karunakaran DK, Venkatesh A, Congdon S, Lemoine C, Kilcollins AM, Mandoiu I, Punzo C, Kanadia RN. Replication-dependent histone genes are actively transcribed in differentiating and aging retinal neurons. Cell Cycle. 2014;13(16):2526-41.

Bannister AJ, Kouzarides T. Regulation of chromatin by histone modifications. Cell Res. 2011;21(3):381-95.

Bano D, Piazzesi A, Salomoni P, Nicotera P. The histone variant H3.3 claims its place in the crowded scene of epigenetics. Aging (Albany NY). 2017;9(3):602-614.

Bardakjian, Tanya, Avery Weiss, and Adele Schneider. Microphthalmia/Anophthalmia/Coloboma Spectrum. 2004. GeneReviews University of Washington, Seattle.

Barbieri AM, Broccoli V, Bovolenta P, Alfano G, Marchitiello A, Mocchetti C, Crippa L, Bulfone A, Marigo V, Ballabio A, Banfi S. Vax2 inactivation in mouse determines alteration of the eye dorsal-ventral axis, misrouting of the optic fibres and eye coloboma. Development. 2002;129(3):805-13.

Barton KM, Levine EM. Expression patterns and cell cycle profiles of PCNA, MCM6, cyclin D1, cyclin A2, cyclin B1, and phosphorylated histone H3 in the developing mouse retina. Dev Dyn. 2008;237(3):672-82.

Becker PB, Workman JL. Nucleosome remodeling and epigenetics. Cold Spring Harb Perspect Biol. 2013;5(9).

Berthoud VM, Minogue PJ, Yu H, Schroeder R, Snabb JI, Beyer EC. Connexin50D47A decreases levels of fiber cell connexins and impairs lens fiber cell differentiation. Invest Ophthalmol Vis Sci. 2013;54(12):7614-22.

Berthoud VM, Minogue PJ, Osmolak P, Snabb JI, Beyer EC. Roles and regulation of lens epithelial cell connexins. FEBS Lett. 2014;588(8):1297-303.

Berthoud VM, Ngezahayo A. Focus on lens connexins. BMC Cell Biol. 2017;18(Suppl 1):6.

Bharti K, Gasper M, Ou J, Brucato M, Clore-Gronenborn K, Pickel J, Arnheiter H. A regulatory loop involving PAX6, MITF, and WNT signaling controls retinal pigment epithelium development. PLoS Genet. 2012;8(7):e1002757.

Bhaumik P, Gopalakrishnan C, Kamaraj B, Purohit R. Single nucleotide polymorphisms in microRNA binding sites: implications in colorectal cancer. Scientific World Journal. 2014; 2014:547154.

Biterge B, Schneider R. Histone variants: key players of chromatin. Cell Tissue Res. 2014;356(3):457-66.

Blixt A, Mahlapuu M, Aitola M, Pelto-Huikko M, Enerbäck S, Carlsson P. A forkhead gene, FoxE3, is essential for lens epithelial proliferation and closure of the lens vesicle. Genes Dev. 2000;14(2):245-54.

Boggs BA, Connors B, Sobel RE, Chinault AC, Allis CD. Reduced levels of histone H3 acetylation on the inactive X chromosome in human females. Chromosoma. 1996;105(5):303-9.

Brzezinski JA 4th, Lamba DA, Reh TA. Blimp1 controls photoreceptor versus bipolar cell fate choice during retinal development. Development. 2010 ;137(4):619-29.

Cantone I, Fisher AG. Epigenetic programming and reprogramming during development. Nat Struct Mol Biol. 2013;20(3):282-9.

Cavalheiro GR, Matos-Rodrigues GE, Gomes AL, Rodrigues PM, Martins RA. c-Myc regulates cell proliferation during lens development. PLoS One. 2014;9(2):e87182.

Chambers TM, Agopian AJ, Lewis RA, Langlois PH, Danysh HE, Weber KA, Shaw GM, Mitchell LE, Lupo PJ. Epidemiology of anophthalmia and microphthalmia: Prevalence and patterns in Texas, 1999-2009. Am J Med Genet A. 2018;176(9):1810-1818.

Chang P, Giddings TH Jr, Winey M, Stearns T. Epsilon-tubulin is required for centriole duplication and microtubule organization. Nat Cell Biol. 2003;5(1):71-6.

Chen C, Ridzon DA, Broomer AJ, Zhou Z, Lee DH, Nguyen JT, Barbisin M, Xu NL, Mahuvakar VR, Andersen MR, Lao KQ, Livak KJ, Guegler KJ. Real-time quantification of microRNAs by stem-loop RT-PCR. Nucleic Acids Res. 2005;33(20):e179.

Chen X, Taube JR, Simirskii VI, Patel TP, Duncan MK. Dual roles for Prox1 in the regulation of the chicken betaB1-crystallin promoter. Invest Ophthalmol Vis Sci. 2008;49(4):1542-52.

Chen X, Zaro JL, Shen WC. Fusion protein linkers: property, design and functionality. Adv Drug Deliv Rev. 2013;65(10):1357-69.

Chrysanthou S, Senner CE, Woods L, Fineberg E, Okkenhaug H, Burge S, Perez-Garcia V, Hemberger M. A Critical role of TET1/2 proteins in cell-cycle progression of trophoblast stem cells. Stem Cell Reports. 2018;10(4):1355-1368.

Churchill A, Graw J. Clinical and experimental advances in congenital and pediatric cataracts. Philos Trans R Soc Lond B Biol Sci. 2011 ;366(1568):1234-49.

Clayton AL, Rose S, Barratt MJ, Mahadevan LC. Phosphoacetylation of histone H3 on c-fos- and c-jun-associated nucleosomes upon gene activation. EMBO J. 2000 ;19(14):3714-26.

Cobb RE, Wang Y, Zhao H. High-efficiency multiplex genome editing of Streptomyces species using an engineered CRISPR/Cas system. ACS Synth Biol. 2015 ;4(6):723-8.

Cox SG, Kim H, Garnett AT, Medeiros DM, An W, Crump JG. An essential role of variant histone H3.3 for ectomesenchyme potential of the cranial neural crest. PLoS Genet. 2012;8(9): e1002938.

Crosio C, Heitz E, Allis CD, Borrelli E, Sassone-Corsi P. Chromatin remodeling and neuronal response: multiple signaling pathways induce specific histone H3 modifications and early gene expression in hippocampal neurons. J Cell Sci. 2003;116(Pt 24):4905-14.

Crosio C, Cermakian N, Allis CD, Sassone-Corsi P. Light induces chromatin modification in cells of the mammalian circadian clock. Nat Neurosci. 2000;3(12):1241-7.

Cvekl A, Mitton KP. Epigenetic regulatory mechanisms in vertebrate eye development and disease. Heredity (Edinb). 2010;105(1):135-51.

Cvekl A, Ashery-Padan R. The cellular and molecular mechanisms of vertebrate lens development. Development. 2014;141(23):4432-47.

Cvekl A, Duncan MK. Genetic and epigenetic mechanisms of gene regulation during lens development. Prog Retin Eye Res. 2007;26(6):555-97.

Dalke C, Graw J. Mouse mutants as models for congenital retinal disorders. Exp Eye Res. 2005;81(5):503-12.

De Rop V, Padeganeh A, Maddox PS. CENP-A: the key player behind centromere identity, propagation, and kinetochore assembly. Chromosoma. 2012;121(6):527-38.

Dorgau B, Herrling R, Schultz K, Greb H, Segelken J, Ströh S, Bolte P, Weiler R, Dedek K, Janssen-Bienhold U. Connexin50 couples axon terminals of mouse horizontal cells by homotypic gap junctions. J Comp Neurol. 2015;523(14):2062-81.

Duhovny D, Nussinov R, Wolfson HJ. Efficient Unbound Docking of Rigid Molecules. In Gusfield et al. Ed. Proceedings of the 2'nd Workshop on Algorithms in Bioinformatics(WABI) Rome, Italy, Lecture Notes in Computer Science 2452, pp. 185-200, Springer Verlag, 2002

Dyer MA, Livesey FJ, Cepko CL, Oliver G. Prox1 function controls progenitor cell proliferation and horizontal cell genesis in the mammalian retina. Nat Genet. 2003;34(1):53-8.

Evans WH, De Vuyst E, Leybaert L. The gap junction cellular internet: connexion hemichannels enter the signaling limelight. Biochem J. 2006;397(1):1-14. Review.

Fang D, Gan H, Cheng L, Lee JH, Zhou H, Sarkaria JN, Daniels DJ, Zhang Z. H3.3K27M mutant proteins reprogram epigenome by sequestering the PRC2 complex to poised enhancers. Elife. 2018 22;7.

Feng J, Liu T, Qin B, Zhang Y, Liu XS. Identifying ChIP-seq enrichment using MACS. Nat Protoc. 2012;7(9):1728-40.

Fleming AB, Pennings S. Antagonistic remodeling by Swi-Snf and Tup1-Ssn6 of an extensive chromatin region forms the background for FLO1 gene regulation. EMBO J. 2001;20(18):5219-31.

Freund C, Horsford DJ, McInnes RR. Transcription factor genes and the developing eye: a genetic perspective. Hum Mol Genet. 1996;5 Spec No:1471-88. Review.

Fritsch L, Robin P, Mathieu JR, Souidi M, Hinaux H, Rougeulle C, Harel-Bellan A, Ameyar-Zazoua M, Ait-Si-Ali S. A subset of the histone H3 lysine 9 methyltransferases Suv39h1, G9a, GLP, and SETDB1 participate in a multimeric complex. Mol Cell. 2010;37(1):46-56.

Fuhrmann S. Eye morphogenesis and patterning of the optic vesicle. Curr Top Dev Biol. 2010; 93:61-84.

Galvani A, Courbeyrette R, Agez M, Ochsenbein F, Mann C, Thuret JY. In-vivo study of the nucleosome assembly functions of ASF1 histone chaperones in human cells. Mol Cell Biol. 2008;28(11):3672-85.

Garcia BA, Hake SB, Diaz RL, Kauer M, Morris SA, Recht J, Shabanowitz J, Mishra N, Strahl BD, Allis CD, Hunt DF. Organismal differences in post-translational modifications in histones H3 and H4. J Biol Chem. 2007;282(10):7641-55.

Glaser T, Jepeal L, Edwards JG, Young SR, Favor J, Maas RL. PAX6 gene dosage effect in a family with congenital cataracts, aniridia, anophthalmia and central nervous system defects. Nat Genet 1994;8(2):203.

Graw J, Löster J, Puk O, Münster D, Haubst N, Soewarto D, Fuchs H, Meyer B, Nürnberg P, Pretsch W, Selby P, Favor J, Wolf E, Hrabé de Angelis M. Three novel *Pax6* alleles in the mouse leading to the same small-eye phenotype caused by different consequences at target promoters. Invest Ophthalmol Vis Sci. 2005;46(12):4671-83.

Graw J. Mouse models of cataract. J Genet. 2009;88(4):469-86.

Graw J. Eye development. Curr Top Dev Biol. 2010;90:343-86.

Graw J. Mouse models for microphthalmia, anophthalmia and cataracts. Hum Genet. 2019. doi: 10.1007/s00439-019-01995-w.

Hainer SJ, Martens JA. Identification of histone mutants that are defective for transcription-coupled nucleosome occupancy. Mol Cell Biol. 2011;31(17):3557-68.

Hake SB, Allis CD. Histone H3 variants and their potential role in indexing mammalian genomes: the "H3 barcode hypothesis". Proc Natl Acad Sci U S A. 2006 ;103(17):6428-35.

Hake SB, Garcia BA, Duncan EM, Kauer M, Dellaire G, Shabanowitz J, Bazett-Jones DP, Allis CD, Hunt DF. Expression patterns and post-translational modifications associated with mammalian histone H3 variants. J Biol Chem. 2006 ;281(1):559-68.

Hanauer A, Young ID. Coffin-Lowry syndrome: clinical and molecular features. J Med Genet. 2002;39(10):705-13.

Handa K, Yamakawa M, Takeda H, Kimura S, Takahashi T. Expression of cell cycle markers in colorectal carcinoma: superiority of cyclin A as an indicator of poor prognosis. Int J Cancer. 1999;84(3):225-33.

Hans F, Dimitrov S. Histone H3 phosphorylation and cell division. Oncogene. 2001;20(24):3021-7.

Harada A, Maehara K, Ono Y, Taguchi H, Yoshioka K, Kitajima Y, Xie Y, Sato Y, Iwasaki T, Nogami J, Okada S, Komatsu T, Semba Y, Takemoto T, Kimura H, Kurumizaka H, Ohkawa Y. Histone H3.3 sub-variant H3mm7 is required for normal skeletal muscle regeneration. Nat Commun. 2018;9(1):1400.

Hari L, Miescher I, Shakhova O, Suter U, Chin L, Taketo M, Richardson WD, Kessaris N, Sommer L. Temporal control of neural crest lineage generation by Wnt/β-catenin signaling. Development. 2012;139(12):2107-17.

Heavner WE, Andoniadou CL, Pevny LH. Establishment of the neurogenic boundary of the mouse retina requires cooperation of SOX2 and WNT signaling. Neural Dev. 2014 9;9:27.

Heavner W, Pevny L. Eye development and retinogenesis. Cold Spring Harb Perspect Biol. 2012 1;4(12).

Hendzel MJ, Wei Y, Mancini MA, Van Hooser A, Ranalli T, Brinkley BR, Bazett-Jones DP, Allis CD. Mitosis-specific phosphorylation of histone H3 initiates primarily within pericentromeric heterochromatin during G2 and spreads in an ordered fashion coincident with mitotic chromosome condensation. Chromosoma. 1997;106(6):348-60.

Henikoff S, Smith MM. Histone variants and epigenetics. Cold Spring Harb Perspect Biol. 2015;7(1):a019364.

Hertwig P. Neue Mutationen und Kopplungsgruppen bei der Hausmaus. Z. Indukt. Abstammungs- u. Vererbungsl. 1942; 80:220–246.

Hever AM, Williamson KA, van Heyningen V. Developmental malformations of the eye: the role of PAX6, SOX2 and OTX2. Clin Genet. 2006;69(6):459-70.

Hill RE, Favor J, Hogan BL, Ton CC, Saunders GF, Hanson IM, Prosser J, Jordan T, Hastie ND, van Heyningen V. Mouse small eye results from mutations in a paired-like homeobox-containing gene. Nature. 1991;354(6354):522-5.

Hou L, Pavan WJ. Transcriptional and signaling regulation in neural crest stem cell-derived melanocyte development: do all roads lead to Mitf? Cell Res. 2008 ;18(12):1163-76.

Howman EV, Fowler KJ, Newson AJ, Redward S, MacDonald AC, Kalitsis P, Choo KH. Early disruption of centromeric chromatin organization in centromere protein A (Cenpa) null mice. Proc Natl Acad Sci U S A. 2000;97(3):1148-53.

Hoyer-Fender S. Molecular aspects of XY body formation. Cytogenet Genome Res. 2003;103(3-4):245-55.

Huang J, Liu Y, Filas B, Gunhaga L, Beebe DC. Negative and positive auto-regulation of BMP expression in early eye development. Dev Biol. 2015 ;407(2):256-64.

Huang T, Garcia R, Qi J, Lulla R, Horbinski C, Behdad A, Wadhwani N, Shilatifard A, James C, Saratsis AM. Detection of histone H3 K27M mutation and post-translational modifications in pediatric diffuse midline glioma via tissue immunohistochemistry informs diagnosis and clinical outcomes. Oncotarget. 2018 ;9(98):37112-37124.

Takeshi I, Tomarev S. Animal Models for Eye Diseases and Therapeutics. In Sourcebook of Models for Biomedical Research 2008.Totowa, NJ: Humana Press, 279–87.

Jang CW, Shibata Y, Starmer J, Yee D, Magnuson T. Histone H3.3 maintains genome integrity during mammalian development. Genes Dev. 2015;29(13):1377-92.

Jerath R, Cearley SM, Barnes VA, Nixon-Shapiro E. How lateral inhibition and fast retinogeniculo-cortical oscillations create vision: A new hypothesis. Med Hypotheses. 2016;96:20-29.

Kahata K, Dadras MS, Moustakas A. TGF-β Family Signaling in Epithelial Differentiation and Epithelial-Mesenchymal Transition. Cold Spring Harb Perspect Biol. 2018 2;10(1).

Kalloniatis M, Nivison-Smith L, Chua J, Acosta ML, Fletcher EL. Using the rd1 mouse to understand functional and anatomical retinal remodeling and treatment implications in retinitis pigmentosa: A review. Exp Eye Res. 2016;150:106-21.

Kar R, Batra N, Riquelme MA, Jiang JX. Biological role of connexion intercellular channels and hemichannels. Arch Biochem Biophys. 2012;524(1):2-15.

Kawabata Y, Kamio A, Jincho Y, Sakashita A, Takashima T, Kobayashi H, Matsui Y, Kono T. Sex-specific histone modifications in mouse fetal and neonatal germ cells. Epigenomics. 2019;11(5):543-561.

Kawauchi S, Takahashi S, Nakajima O, Ogino H, Morita M, Nishizawa M, Yasuda K, Yamamoto M. Regulation of lens fibre cell differentiation by transcription factor c-Maf. J Biol Chem. 1999;274(27):19254-60.

Kebede AF, Schneider R, Daujat S. Novel types and sites of histone modifications emerge as players in the transcriptional regulation contest. FEBS J. 2015;282(9):1658-74.

Kebede AF, Nieborak A, Shahidian LZ, Le Gras S, Richter F, Gómez DA, Baltissen MP, Meszaros G, Magliarelli HF, Taudt A, Margueron R, Colomé-Tatché M, Ricci R, Daujat S, Vermeulen M, Mittler G, Schneider R. Histone propionylation is a mark of active chromatin. Nat Struct Mol Biol. 2017;24(12):1048-1056.

Kidder GM, Cyr DG. Roles of connexins in testis development and spermatogenesis. Semin Cell Dev Biol. 2016; 50:22-30.

Kim PG, Nakano H, Das PP, Chen MJ, Rowe RG, Chou SS, Ross SJ, Sakamoto KM, Zon Li, Schlaeger TM, Orkin SH, Nakano A, Daley GQ. Flow-induced protein kinase A-CREB pathway acts via BMP signaling to promote HSC emergence. J Exp Med. 2015;212(5):633-48.

Kramer MF. Stem-loop RT-qPCR for miRNAs. Curr Protoc Mol Biol. 2011; Chapter 15: Unit 15.10.

Kranz K, Paquet-Durand F, Weiler R, Janssen-Bienhold U, Dedek K. Testing for a gap junction-mediated bystander effect in retinitis pigmentosa: secondary cone death is not altered by deletion of connexin36 from cones. PLoS One. 2013;8(2):e57163.

Krebs MP, Collin GB, Hicks WL, Yu M, Charette JR, Shi LY, Wang J, Naggert JK, Peachey NS, Nishina PM. Mouse models of human ocular disease for translational research. PLoS One. 2017;12(8):e0183837.

Kubicek S, Schotta G, Lachner M, Sengupta R, Kohlmaier A, Perez-Burgos L, Linderson Y, Martens JH, O'Sullivan RJ, Fodor BD, Yonezawa M, Peters AH, Jenuwein T. The role of histone modifications in epigenetic transitions during normal and perturbed development. Ernst Schering Res Found Workshop. 2006;(57):1-27.

Kuhn DE, Martin MM, Feldman DS, Terry AV Jr, Nuovo GJ, Elton TS. Experimental validation of miRNA targets. Methods. 2008;44(1):47-54.

Kumar M, Agarwal T, Kaur P, Kumar M, Khokhar S, Dada R. Molecular and structural analysis of genetic variations in congenital cataract. Mol Vis. 2013;19: 2436-50.

Kurumizaka H, Wolffe AP. Sin mutations of histone H3: influence on nucleosome core structure and function. Mol Cell Biol. 1997;17(12):6953-69.

Panda SK. Establishment of mouse disease models by using sequence specific nucleases. 2014. Doctoral Thesis, Technische Universität München. https://mediatum.ub.tum.de/doc/1205835/1205835.pdf.

Lan J, Lepikhov K, Giehr P, Walter J. Histone and DNA methylation control by H3 serine 10/threonine 11 phosphorylation in the mouse zygote. Epigenetics Chromatin. 2017 14;10:5.

Larson JD, Kasper LH, Paugh BS, Jin H, Wu G, Kwon CH, Fan Y, Shaw TI, Silveira AB, Qu C, Xu R, Zhu X, Zhang J, Russell HR, Peters JL, Finkelstein D, Xu B, Lin T, Tinkle CL, Patay Z, Onar-Thomas A, Pounds SB, McKinnon PJ, Ellison DW, Zhang J, Baker SJ. Histone H3.3 K27M accelerates spontaneous brainstem glioma and drives restricted changes in bivalent gene expression. Cancer Cell. 2019;35(1):140-155.e7.

Le LT, Vu HL, Nguyen CH, Molla A. Basal aurora kinase B activity is sufficient for histone H3 phosphorylation in prophase. Biol Open. 2013;2(4):379-86.

Lerdrup M, Johansen JV, Agrawal-Singh S, Hansen K. An interactive environment for agile analysis and visualization of ChIP-sequencing data. Nat Struct Mol Biol. 2016;23(4):349-57.

Li H, Chang YY, Yang LW, Bahar I. iGNM 2.0: the Gaussian network model database for biomolecular structural dynamics. Nucleic Acids Res. 2016 ;44(D1):D415-22.

Li J, Dani JA, Le W. The role of transcription factor Pitx3 in dopamine neuron development and Parkinson's disease. Curr Top Med Chem. 2009;9(10):855-9.

Li Y, Seto E. HDACs and HDAC Inhibitors in Cancer Development and Therapy. Cold Spring Harb Perspect Med. 2016 3;6(10).

Liang X, Potter J, Kumar S, Zou Y, Quintanilla R, Sridharan M, Carte J, Chen W, Roark N, Ranganathan S, Ravinder N, Chesnut JD. Rapid and highly efficient mammalian cell engineering via Cas9 protein transfection. J Biotechnol. 2015; 208:44-53.

Liu J, Xu J, Gu S, Nicholson BJ, Jiang JX. Aquaporin 0 enhances gap junction coupling via its cell adhesion function and interaction with connexin 50. J Cell Sci. 2011;124(Pt 2):198-206.

Liu MM, Chan CC, Tuo J. Epigenetics in ocular diseases. Curr Genomics. 2013;14(3):166-72.

Livak KJ, Schmittgen TD. Analysis of relative gene expression data using real-time quantitative PCR and the 2(-Delta Delta C(T)) Method. Methods. 2001;25(4):402-8.

Livesey FJ, Cepko CL. Vertebrate neural cell-fate determination: lessons from the retina. Nat Rev Neurosci. 2001;2(2):109-18.

Love J, Axton R, Churchill A, van Heyningen V, Hanson I. A new set of primers for mutation analysis of the human PAX6 gene. Hum Mutat. 1998;12(2):128-34.

Loyola A, Bonaldi T, Roche D, Imhof A, Almouzni G. PTMs on H3 variants before chromatin assembly potentiate their final epigenetic state. Mol Cell. 2006 ;24(2):309-16.

Maehara K, Harada A, Sato Y, Matsumoto M, Nakayama KI, Kimura H, Ohkawa Y. Tissue-specific expression of histone H3 variants diversified after species separation. Epigenetics Chromatin. 2015 17;8:35.

Maes M, Crespo Yanguas S, Willebrords J, Cogliati B, Vinken M. Connexin and pannexin signaling in gastrointestinal and liver disease. Transl Res. 2015;166(4):332-43.

Manuel M, Pratt T, Liu M, Jeffery G, Price DJ. Overexpression of Pax6 results in microphthalmia, retinal dysplasia and defective retinal ganglion cell axon guidance. BMC Dev Biol. 2008 28;8:59.

Marino-Ramírez L, Kann MG, Shoemaker BA, Landsman D. Histone structure and nucleosome stability. Expert Rev Proteomics. 2005;2(5):719-29.

Marzluff WF, Gongidi P, Woods KR, Jin J, Maltais LJ. The human and mouse replication-dependent histone genes. Genomics. 2002;80(5):487-98.

Marzluff WF, Koreski KP. Birth and Death of Histone mRNAs. Trends Genet. 2017 ;33(10):745-759.

Mathers PH, Grinberg A, Mahon KA, Jamrich M. The Rx homeobox gene is essential for vertebrate eye development. Nature. 1997;387(6633):603-7.

Mathias RT, White TW, Gong X. Lens gap junctions in growth, differentiation, and homeostasis. Physiol Rev. 2010;90(1):179-206.

Matsushima D, Heavner W, Pevny LH. Combinatorial regulation of optic cup progenitor cell fate by SOX2 and PAX6. Development. 2011;138(3):443-54.

Mersfelder EL, Parthun MR. The tale beyond the tail: histone core domain modifications and the regulation of chromatin structure. Nucleic Acids Res. 2006;34(9):2653-62.

Muranishi Y, Terada K, Furukawa T. An essential role for Rax in retina and neuroendocrine system development. Dev Growth Differ. 2012;54(3):341-8.

Muthurajan UM, Bao Y, Forsberg LJ, Edayathumangalam RS, Dyer PN, White CL, Luger K. Crystal structures of histone Sin mutant nucleosomes reveal altered protein-DNA interactions. EMBO J. 2004;23(2):260-71.

Nielsen MS, Axelsen LN, Sorgen PL, Verma V, Delmar M, Holstein-Rathlou NH. Gap junctions. Compr Physiol. 2012;2(3):1981-2035.

Noh H, Lee H, Park E, Park S. Proper closure of the optic fissure requires ephrin A5-EphB2-JNK signaling. Development. 2016;143(3):461-72.

Ohuchi H, Sato K, Habuta M, Fujita H, Bando T. Congenital eye anomalies: More mosaic than thought? Congenit Anom (Kyoto). 2019;59(3):56-73.

Oliver SS, Denu JM. Dynamic interplay between histone H3 modifications and protein interpreters: emerging evidence for a "histone language". Chembiochem. 2011;12(2):299-307.

Osumi N, Shinohara H, Numayama-Tsuruta K, Maekawa M. Concise review: Pax6 transcription factor contributes to both embryonic and adult neurogenesis as a multifunctional regulator. Stem Cells. 2008;26(7):1663-72.

Owczarzy R, Tataurov AV, Wu Y, Manthey JA, McQuisten KA, Almabrazi HG, Pedersen KF, Lin Y, Garretson J, McEntaggart NO, Sailor CA, Dawson RB, Peek AS. IDT SciTools: a suite for analysis and design of nucleic acid oligomers. Nucleic Acids Res. 2008;36(Web Server issue):W163-9.

Paix A, Folkmann A, Seydoux G. Precision genome editing using CRISPR-Cas9 and linear repair templates in C. elegans. Methods. 2017;121-122:86-93.

Palmer DK, O'Day K, Trong HL, Charbonneau H, Margolis RL. Purification of the centromere-specific protein CENP-A and demonstration that it is a distinctive histone. Proc Natl Acad Sci U S A. 1991;88(9):3734-8.

Pan L, Yang Z, Feng L, Gan L. Functional equivalence of Brn3 POU-domain transcription factors in mouse retinal neurogenesis. Development. 2005;132(4):703-12.

Patterson SS, Dionisi HM, Gupta RK, Sayler GS. Codon optimization of bacterial luciferase (lux) for expression in mammalian cells. J Ind Microbiol Biotechnol. 2005;32(3):115-23.

Pédelacq JD, Cabantous S, Tran T, Terwilliger TC, Waldo GS. Engineering and characterization of a superfolder green fluorescent protein. Nat Biotechnol. 2006;24(1):79-88.

Pelletier RM, Akpovi CD, Chen L, Kumar NM, Vitale ML. Complementary expression and phosphorylation of Cx46 and Cx50 during development and following gene deletion in mouse and in normal and orchitic mink testes. Am J Physiol Regul Integr Comp Physiol. 2015;309(3):R255-76.

Pennington KL, DeAngelis MM. Epigenetic Mechanisms of the Aging Human Retina. J Exp Neurosci. 2016;9(Suppl 2):51-79.

Peterson SM, Thompson JA, Ufkin ML, Sathyanarayana P, Liaw L, Congdon CB. Common features of microRNA target prediction tools. Front Genet. 2014 18;5:23.

Pfaffl MW, Horgan GW, Dempfle L. Relative expression software tool (REST) for group-wise comparison and statistical analysis of relative expression results in real-time PCR. Nucleic Acids Res. 2002;30(9):e36.

Pfenniger A, Wohlwend A, Kwak BR. Mutations in connexin genes and disease. Eur J Clin Invest. 2011;41(1):103-16.

Pirity MK, Wang WL, Wolf LV, Tamm ER, Schreiber-Agus N, Cvekl A. Rybp, a polycomb complex-associated protein, is required for mouse eye development. BMC Dev Biol. 2007 30;7:39.

Plaisancie J, Calvas P, Chassaing N. Genetic Advances in Microphthalmia. J Pediatr Genet. 2016;5(4):184-188.

Polo SE, Roche D, Almouzni G. New histone incorporation marks sites of UV repair in human cells. Cell. 2006;127(3):481-93.

Popova EY, Xu X, DeWan AT, Salzberg AC, Berg A, Hoh J, Zhang SS, Barnstable CJ. Stage and gene specific signatures defined by histones H3K4me2 and H3K27me3 accompany mammalian retina maturation in-vivo. PLoS One. 2012;7(10):e46867.

Rajagopal R, Huang J, Dattilo LK, Kaartinen V, Mishina Y, Deng CX, Umans L, Zwijsen A, Roberts AB, Beebe DC. The type I BMP receptors, Bmpr1a and Acvr1, activate multiple signaling pathways to regulate lens formation. Dev Biol. 2009;335(2):305-16.

Ramaswamy A, Ioshikhes I. Dynamics of modeled oligonucleosomes and the role of histone variant proteins in nucleosome organization. Adv Protein Chem Struct Biol. 2013;90:119-49.

Raney BJ, Dreszer TR, Barber GP, Clawson H, Fujita PA, Wang T, Nguyen N, Paten B, Zweig AS, Karolchik D, Kent WJ. Track Data Hubs enable visualization of user-defined genome-wide annotations on the UCSC Genome Browser. Bioinformatics. 2014 1;30(7):1003-5.

Rao RC, Tchedre KT, Malik MT, Coleman N, Fang Y, Marquez VE, Chen DF. Dynamic patterns of histone lysine methylation in the developing retina. Invest Ophthalmol Vis Sci. 2010;51(12):6784-92.

Reed DR, Li X, McDaniel AH, Lu K, Li S, Tordoff MG, Price RA, Bachmanov AA. Loci on chromosomes 2, 4, 9, and 16 for body weight, body length, and adiposity identified in a genome scan of an F2 intercross between the 129P3/J and C57BL/6ByJ mouse strains. Mamm Genome. 2003;14(5):302-13.

Reis LM, Semina EV. Conserved genetic pathways associated with microphthalmia, anophthalmia, and coloboma. Birth Defects Res C Embryo Today. 2015;105(2):96-113.

Ribas VT, Gonçalves BS, Linden R, Chiarini LB. Activation of c-Jun N-terminal kinase (JNK) during mitosis in retinal progenitor cells. PLoS One.2012;7(4):e34483.

Richter-Kügler A. Gene Expression Analysis of the Aey69 Mouse Mutant Related to Eye Phenotype. 2013. Master Thesis, Technische Universität München.

Rieger DK, Reichenberger E, McLean W, Sidow A, Olsen BR. A double-deletion mutation in the Pitx3 gene causes arrested lens development in aphakia mice. Genomics. 2001;72(1):61-72.

Rosano GL, Ceccarelli EA. Recombinant protein expression in Escherichia coli: advances and challenges. Front Microbiol. 2014 17;5:172.

Rosemann M, Ivashkevich A, Favor J, Dalke C, Hölter SM, Becker L, Rácz I, Bolle I, Klempt M, Rathkolb B, Kalaydjiev S, Adler T, Aguilar A, Hans W, Horsch M, Rozman J, Calzada-Wack J, Kunder S, Naton B, Gailus-Durner V, Fuchs H, Schulz H, Beckers J, Busch DH, Burbach JP, Smidt MP, Quintanilla-Martinez L, Esposito I, Klopstock T, Klingenspor M, Ollert M, Wolf E, Wurst W, Zimmer A, de Angelis MH, Atkinson M, Heinzmann U, Graw J. Microphthalmia, parkinsonism, and enhanced nociception in Pitx3 (416insG) mice. Mamm Genome. 2010;21(1-2):13-27.

Rothbart SB, Dickson BM, Raab JR, Grzybowski AT, Krajewski K, Guo AH, Shanle EK, Josefowicz SZ, Fuchs SM, Allis CD, Magnuson TR, Ruthenburg AJ, Strahl BD. an interactive database for the assessment of histone antibody specificity. Mol Cell. 2015;59(3):502-11.

Runge PE, Hawes NL, Heckenlively JR, Langley SH, Roderick TH. Autosomal dominant mouse cataract (Lop-10). Consistent differences of expression in heterozygotes. Invest Ophthalmol Vis Sci. 1992;33(11):3202-8.

Sadakierska-Chudy A, Kostrzewa RM, Filip M. A comprehensive view of the epigenetic landscape part I: DNA methylation, passive and active DNA demethylation pathways and histone variants. Neurotox Res. 2015;27(1):84-97.

Saili KS, Tilton SC, Waters KM, Tanguay RL. Global gene expression analysis reveals pathway differences between teratogenic and non-teratogenic exposure concentrations of bisphenol A and 17β-estradiol in embryonic zebrafish. Reprod Toxicol. 2013;38:89-101.

Sawicka A, Seiser C. Histone H3 phosphorylation - a versatile chromatin modification for different occasions. Biochimie. 2012;94(11):2193-201.

Schenk R, Jenke A, Zilbauer M, Wirth S, Postberg J. H3.5 is a novel hominid-specific histone H3 variant that is specifically expressed in the seminiferous tubules of human testes. Chromosoma. 2011;120(3):275-85.

Schneider A, Bardakjian T, Reis LM, Tyler RC, Semina EV. Novel SOX2 mutations and genotype-phenotype correlation in anophthalmia and microphthalmia. Am J Med Genet A. 2009;149A(12):2706-15.

Schneider TD, Arteaga-Salas JM, Mentele E, David R, Nicetto D, Imhof A, Rupp RA. Stage-specific histone modification profiles reveal global transitions in the Xenopus embryonic epigenome. PLoS One. 2011;6(7):e22548.

Schneidman-Duhovny D, Inbar Y, Nussinov R, Wolfson HJ. PatchDock and SymmDock: servers for rigid and symmetric docking. Nucl. Acids. Res. 33: W363-367, 2005

Schwämmle V, Sidoli S, Ruminowicz C, Wu X, Lee CF, Helin K, Jensen ON. systems level analysis of histone H3 post-translational modifications (PTMS) reveals features of PTM crosstalk in chromatin regulation. Mol Cell Proteomics. 2016;15(8):2715-29.

Schwartzentruber J, Korshunov A, Liu XY, Jones DT, Pfaff E, Jacob K, Sturm D, Fontebasso AM, Quang DA, Tönjes M, Hovestadt V, Albrecht S, Kool M, Nantel A, Konermann C, Lindroth A, Jäger N, Rausch T, Ryzhova M, Korbel JO, Hielscher T, Hauser P, Garami M, Klekner A,

Bognar L, Ebinger M, Schuhmann MU, Scheurlen W, Pekrun A, Frühwald MC, Roggendorf W, Kramm C, Dürken M, Atkinson J, Lepage P, Montpetit A, Zakrzewska M, Zakrzewski K, Liberski PP, Dong Z, Siegel P, Kulozik AE, Zapatka M, Guha A, Malkin D, Felsberg J, Reifenberger G, von Deimling A, Ichimura K, Collins VP, Witt H, Milde T, Witt O, Zhang C, Castelo-Branco P, Lichter P, Faury D, Tabori U, Plass C, Majewski J, Pfister SM, Jabado N. Driver mutations in histone H3.3 and chromatin remodeling genes in pediatric glioblastoma. Nature. 2012;482(7384):226-31.

Semina EV, Ferrell RE, Mintz-Hittner HA, Bitoun P, Alward WL, Reiter RS, Funkhauser C, Daack-Hirsch S, Murray JC. A novel homeobox gene PITX3 is mutated in families with autosomal-dominant cataracts and ASMD. Nat Genet.1998;19:167–170.

Semina EV, Murray JC, Reiter R, Hrstka RF, Graw J. Deletion in the promoter region and altered expression of Pitx3 homeobox gene in aphakia mice. Hum Mol Genet. 2000;9(11):1575-85.

Shah SP, Taylor AE, Sowden JC, Ragge NK, Russell-Eggitt I, Rahi JS, Gilbert CE; Surveillance of Eye Anomalies (SEA-UK) Special Interest Group. Anophthalmos, microphthalmos, and typical coloboma in the United Kingdom: a prospective study of incidence and risk. Invest Ophthalmol Vis Sci. 2011;52(1):558-64.

Shi Q, Gu S, Yu XS, White TW, Banks EA, Jiang JX. Connexin controls cell-cycle exit and cell differentiation by directly promoting cytosolic localization and degradation of E3 Ligase Skp2. Dev Cell. 2015;35(4):483-96.

Shiraishi K, Shindo A, Harada A, Kurumizaka H, Kimura H, Ohkawa Y, Matsuyama H. Roles of histone H3.5 in human spermatogenesis and spermatogenic disorders. Andrology. 2018;6(1):158-165.

Sinkkonen, L. MicroRNAs Regulate de Novo DNA Methylation and Histone MRNA 3' End Formation in Mammalian Cells. 2008. Doctoral Thesis, University of Basel https://edoc.unibas.ch/848/1/DissB_8426.pdf.

Skene PJ, Henikoff S. Histone variants in pluripotency and disease. Development. 2013;140(12):2513-24.

Slavotinek AM. Eye development genes and known syndromes. Mol Genet Metab. 2011;104(4):448-56.

Smith AN, Miller LA, Radice G, Ashery-Padan R, Lang RA. Stage-dependent modes of Pax6-Sox2 epistasis regulate lens development and eye morphogenesis. Development. 2009;136(17):2977-85.

Solovei I, Kreysing M, Lanctôt C, Kösem S, Peichl L, Cremer T, Guck J, Joffe B. Nuclear architecture of rod photoreceptor cells adapts to vision in mammalian evolution. Cell. 2009;137(2):356-68.

Srivastava R, Budak G, Dash S, Lachke SA, Janga SC. Transcriptome analysis of developing lens reveals abundance of novel transcripts and extensive splicing alterations. Sci Rep. 2017;7(1):11572.

Steingrímsson E, Arnheiter H, Hallsson JH, Lamoreux ML, Copeland NG, Jenkins NA. Interallelic complementation at the mouse Mitf locus. Genetics. 2003;163(1):267-76.

Stillman B. Histone Modifications: Insights into their influence on gene expression. Cell. 2018;175(1):6-9.

Stottmann R, Beier D. ENU Mutagenesis in the Mouse. Curr Protoc Hum Genet. 2014;82:15.4.1-10.

Strahl BD, Allis CD. The language of covalent histone modifications. Nature. 2000;403(6765):41-5.

Su X, Ren C, Freitas MA. Mass spectrometry-based strategies for characterization of histones and their post-translational modifications. Expert Rev Proteomics. 2007;4(2):211-25.

Sundin OH. The mouse's eye and Mfrp: not quite human. Ophthalmic Genet. 2005 ;26(4):1535.

Swindell EC, Liu C, Shah R, Smith AN, Lang RA, Jamrich M. Eye formation in the absence of retina. Dev Biol. 2008;322(1):56-64.

Szenker E, Ray-Gallet D, Almouzni G. The double face of the histone variant H3.3. Cell Res. 2011;21(3):421-34.

Szewczyk E, Nayak T, Oakley CE, Edgerton H, Xiong Y, Taheri-Talesh N, Osmani SA, Oakley BR. Fusion PCR and gene targeting in Aspergillus nidulans. Nat Protoc. 2006;1(6):3111-20.

Tachiwana H, Osakabe A, Kimura H, Kurumizaka H. Nucleosome formation with the testis-specific histone H3 variant, H3t, by human nucleosome assembly proteins in vitro. Nucleic Acids Res. 2008;36(7):2208-18.

Takahashi JS, Pinto LH, Vitaterna MH. Forward and reverse genetic approaches to behavior in the mouse. Science. 1994;264(5166):1724-33.

Taranova OV, Magness ST, Fagan BM, Wu Y, Surzenko N, Hutton SR, Pevny LH. SOX2 is a dose-dependent regulator of retinal neural progenitor competence. Genes Dev. 2006;20(9):1187-202.

Taverna SD, Li H, Ruthenburg AJ, Allis CD, Patel DJ. How chromatin-binding modules interpret histone modifications: lessons from professional pocket pickers. Nat Struct Mol Biol. 2007;14(11):1025-1040.

Thaung C, West K, Clark BJ, McKie L, Morgan JE, Arnold K, Nolan PM, Peters J, Hunter AJ, Brown SD, Jackson IJ, Cross SH. Novel ENU-induced eye mutations in the mouse: models for human eye disease. Hum Mol Genet. 2002;11(7):755-67.

Tomarev SI, Sundin O, Banerjee-Basu S, Duncan MK, Yang JM, Piatigorsky J. Chicken homeobox gene Prox 1 related to Drosophila prospero is expressed in the developing lens and retina. Dev Dyn. 1996;206(4):354-67.

Tovchigrechko A, Vakser IA. GRAMM-X public web server for protein-protein docking. Nucleic Acids Res. 2006; 34:W310-4.

Tropberger P, Schneider R. Going global: novel histone modifications in the globular domain of H3. Epigenetics. 2010;5(2):112-7.

Tvardovskiy A, Schwämmle V, Kempf SJ, Rogowska-Wrzesinska A, Jensen ON. Accumulation of histone variant H3.3 with age is associated with profound changes in the histone methylation landscape. Nucleic Acids Res. 2017;45(16):9272-9289.

Ueda J, Harada A, Urahama T, Machida S, Maehara K, Hada M, Makino Y, Nogami J, Horikoshi N, Osakabe A, Taguchi H, Tanaka H, Tachiwana H, Yao T, Yamada M, Iwamoto T, Isotani A, Ikawa M, Tachibana T, Okada Y, Kimura H, Ohkawa Y, Kurumizaka H, Yamagata K. Testis-Specific Histone Variant H3t Gene is essential for entry into spermatogenesis. Cell Rep. 2017;18(3):593-600.

Urahama T, Harada A, Maehara K, Horikoshi N, Sato K, Sato Y, Shiraishi K, Sugino N, Osakabe A, Tachiwana H, Kagawa W, Kimura H, Ohkawa Y, Kurumizaka H. Histone H3.5 forms an unstable nucleosome and accumulates around transcription start sites in human testis. Epigenetics Chromatin. 2016 15;9:2.

Usui A, Mochizuki Y, Iida A, Miyauchi E, Satoh S, Sock E, Nakauchi H, Aburatani H, Murakami A, Wegner M, Watanabe S. The early retinal progenitor-expressed gene Sox11 regulates the timing of the differentiation of retinal cells. Development. 2013;140(4):740-50.

Vardabasso C, Hasson D, Ratnakumar K, Chung CY, Duarte LF, Bernstein E. Histone variants: emerging players in cancer biology. Cell Mol Life Sci. 2014;71(3):379-404.

Vastenhouw NL, Schier AF. Bivalent histone modifications in early embryogenesis. Curr Opin Cell Biol. 2012;24(3):374-86.

Veazey KJ, Golding MC. Selection of stable reference genes for quantitative RT-PCR comparisons of mouse embryonic and extra-embryonic stem cells. PLoS One. 2011;6(11):e27592.

Verma AS, Fitzpatrick DR. Anophthalmia and microphthalmia. Orphanet J Rare Dis. 2007 26;2:47.

Vetrivel S, Tiso N, Kügler A, Irmler M, Horsch M, Beckers J, Hladik D, Giesert F, Gailus-Durner V, Fuchs H, Sabrautzki S; German Mouse Clinic, Helmholtz Zentrum München, German Research Center for Environmental Health GmbH, Neuherberg, Germany, Hrabě de Angelis M, Graw J. Mutation in the mouse histone gene Hist2h3c1 leads to degeneration of the lens vesicle and severe microphthalmia. Exp Eye Res. 2019. pii: S0014-4835(18)30702-4.

Vitale ML, Garcia CJ, Akpovi CD, Pelletier RM. Distinctive actions of connexion 46 and connexin 50 in anterior pituitary folliculostellate cells. PLoS One. 2017;12(7):e0182495.

Voon HPJ, Udugama M, Lin W, Hii L, Law RHP, Steer DL, Das PP, Mann JR, Wong LH. Inhibition of a K9/K36 demethylase by an H3.3 point mutation found in pediatric glioblastoma. Nat Commun. 2018;9(1):3142.

Wada K, Matsushima Y, Tada T, Hasegawa S, Obara Y, Yoshizawa Y, Takahashi G, Hiai H, Shimanuki M, Suzuki S, Saitou J, Yamamoto N, Ichikawa M, Watanabe K, Kikkawa Y. Expression of truncated PITX3 in the developing lens leads to microphthalmia and aphakia in mice. PLoS One. 2014 27;9(10):e111432.

Wang Q, Huang J, Sun H, Liu J, Wang J, Wang Q, Qin Q, Mei S, Zhao C, Yang X, Liu XS, Zhang Y. CR Cistrome: a ChIP-Seq database for chromatin regulators and histone modification linkages in human and mouse. Nucleic Acids Res. 2014;42(Database issue):D450-8.

Wang H, Wu X, Lezmi S, Li Q, Helferich WG, Xu Y, Chen H. Extract of Ginkgo biloba exacerbates liver metastasis in a mouse colon cancer Xenograft model. BMC Complement Altern Med. 2017;17(1):516.

Wang X. Improving microRNA target prediction by modeling with unambiguously identified microRNA-target pairs from CLIP-ligation studies. Bioinformatics. 2016;32(9):1316-22.

Wang ZF, Tisovec R, Debry RW, Frey MR, Matera AG, Marzluff WF. Characterization of the 55-kb mouse histone gene cluster on chromosome 3. Genome Res. 1996;6(8):702-14.

Welby JP, Kaptzan T, Wohl A, Peterson TE, Raghunathan A, Brown DA, Gupta SK, Zhang L, Daniels DJ. Current Murine Models and New Developments in H3K27M Diffuse Midline Gliomas. Front Oncol. 2019 27;9:92.

White TW, Bruzzone R. Intercellular communication in the eye: clarifying the need for connexin diversity. Brain Res Brain Res Rev. 2000;32(1):130-7.

Wigle JT, Oliver G. Prox1 function is required for the development of the murine lymphatic system. Cell. 1999;98(6):769-78.

Williamson KA, FitzPatrick DR. The genetic architecture of microphthalmia, anophthalmia and coloboma. Eur J Med Genet. 2014;57(8):369-80.

Willoughby CE, Ponzin D, Ferrari S, Lobo A, Landau K, Omidi Y. Anatomy and physiology of the human eye: effects of mucopolysaccharidoses disease on structure and function–a review. Clinical & Experimental Ophthalmology. 2010;38:2–11.

Wride MA. Lens fibre cell differentiation and organelle loss: many paths lead to clarity. Philos Trans R Soc Lond B Biol Sci. 2011;366(1568):1219-33.

Xu HE, Rould MA, Xu W, Epstein JA, Maas RL, Pabo CO. Crystal structure of the human Pax6 paired domain-DNA complex reveals specific roles for the linker region and carboxy-terminal subdomain in DNA binding. Genes Dev. 1999;13(10):1263-75.

Yan B, Yao J, Tao ZF, Jiang Q. Epigenetics and ocular diseases: from basic biology to clinical study. J Cell Physiol. 2014;229(7):825-33.

Yang J, Yan R, Roy A, Xu D, Poisson J, Zhang Y. The I-TASSER Suite: protein structure and function prediction. Nat Methods. 2015;12(1):7-8.

Yang Y, Stopka T, Golestaneh N, Wang Y, Wu K, Li A, Chauhan BK, Gao CY, Cveklová K, Duncan MK, Pestell RG, Chepelinsky AB, Skoultchi AI, Cvekl A. Regulation of alphaA-crystallin via Pax6, c-Maf, CREB and a broad domain of lens-specific chromatin. EMBO J. 2006;25(10):2107-18.

Yasue A, Kono H, Habuta M, Bando T, Sato K, Inoue J, Oyadomari S, Noji S, Tanaka E, Ohuchi H. Relationship between somatic mosaicism of Pax6 mutation and variable developmental eye abnormalities-an analysis of CRISPR genome-edited mouse embryos. Sci Rep. 2017;7(1):53.

Ye J, Coulouris G, Zaretskaya I, Cutcutache I, Rozen S, Madden TL. Primer-BLAST: a tool to design target-specific primers for polymerase chain reaction. BMC Bioinformatics. 2012 18;13:134.

Yeager M, Harris AL. Gap junction channel structure in the early 21st century: facts and fantasies. Curr Opin Cell Biol. 2007;19(5):521-8.

You L, Yan K, Zou J, Zhao H, Bertos NR, Park M, Wang E, Yang XJ. The chromatin regulator Brpf1 regulates embryo development and cell proliferation. J Biol Chem. 2015;290(18):11349-64.

Young RW. Cell differentiation in the retina of the mouse. Anat Rec. 1985;212(2):199-205.

Yu W, Wu Z. In-vivo Applications of CRISPR-Based Genome Editing in the Retina. Front Cell Dev Biol. 2018 14;6:53.

Yu W, Yu Z, Wu D, Zhang J, Zhu Y, Zhang Y, Ning H, Wang M, Zhang J, Zhao J. Lens-specific conditional knockout of Msx2 in mice leads to ocular anterior segment dysgenesis via activation of a calcium signaling pathway. Lab Invest. 2019.doi: 10.1038/s41374-018-0180-y.

Yu Y, Wu M, Chen X, Zhu Y, Gong X, Yao K. Identification and functional analysis of two novel connexin 50 mutations associated with autosome dominant congenital cataracts. Sci Rep. 2016 24;6:26551.

Zagozewski JL, Zhang Q, Eisenstat DD. Genetic regulation of vertebrate eye development. Clin Genet. 2014;86(5):453-60.

Zerbino DR, Achuthan P, Akanni W, et al. Ensembl 2018. Nucleic Acids Res. 2018;46(D1):D754-D761.

Zhang L, Mathers PH, Jamrich M. Function of Rx, but not Pax6, is essential for the formation of retinal progenitor cells in mice. Genesis. 2000;28(3-4):135-42.

Zhang Y, Ku WL, Liu S, Cui K, Jin W, Tang Q, Lu W, Ni B, Zhao K. Genome-wide identification of histone H2A and histone variant H2A.Z-interacting proteins by bPPI-seq. Cell Res. 2017;27(10):1258-1274.

Zhang Y, Ge X, Yang F, Zhang L, Zheng J, Tan X, Jin ZB, Qu J, Gu F. Comparison of non-canonical PAMs for CRISPR/Cas9-mediated DNA cleavage in human cells. Sci Rep. 2014 23;4:5405.